

Design, Synthesis, and Characterization of
Magnetite Clusters using a Multi Inlet Vortex Mixer

by

Raquel Mejia-Ariza

Thesis submitted to the Faculty of the
Virginia Polytechnic Institute and State University
in partial fulfillment of the requirements for the degree of

Master of Science

In

Macromolecular Science and Engineering Program

Richey M. Davis, Committee Chair

Judy S. Riffle, Committee Co-chair

Kevin J. Edgar, Committee Member

October 18, 2010

Blacksburg, Virginia

Keywords: Rapid nanoprecipitation, Multi Inlet Vortex Mixer, magnetite clusters, poly (ethylene oxide), poly (propylene oxide), steric stabilization, contrast agent

Copyright 2010

Design, Synthesis, and Characterization of Magnetite Clusters using a Multi Inlet Vortex Mixer

Raquel Mejia-Ariza

ABSTRACT

Superparamagnetic nanoparticles have potential applications in targeted drug delivery and as magnetic resonance imaging contrast agents. Magnetite clusters are of particular interest for these applications because they provide higher magnetic flux (under a magnetic field) than individual magnetite nanoparticles, are biocompatible, and their size and compositions can be controlled. This thesis involves the controlled synthesis and characterization of clusters composed of magnetite nanoparticles stabilized with an amphiphilic block copolymer. It outlines a method to design and form well-defined and colloiddally stable magnetite clusters. A Multi Inlet Vortex mixer (MIVM) was used because it is a continuous process that yields particles with relatively narrow and controlled size distributions. In the MIVM, four liquid streams collide under turbulent conditions in the mixing chamber where clusters form within milliseconds. The formation of magnetite clusters was studied in the presence of amphiphilic block copolymers containing poly (ethylene oxide) to provide steric stabilization and control of size distributions using flash nanoprecipitation.

First, the mixer was tested using β -carotene as a model compound to form nanoparticles stabilized with an amphiphilic triblock copolymer poly(propylene oxide)-b-poly(ethylene oxide) (F127) at different Reynolds numbers and supersaturation values. Size analysis was done using dynamic light scattering and nanoparticle tracking analysis techniques. The cluster structure was studied using electron microscopy and magnetite compositions were measured using thermogravimetric analysis. Finally, the stability of magnetite clusters was studied over time and the effect of an applied magnetite field on the colloidal stability was investigated.

Dedication

This work is dedicated to my three very special men in my life:

Federico A. Mejia Pardo, Juan M. Mejia-Ariza, and Thomas Weinhart; thank you for your advice and support, and always believing in my scientific skills.

“Sorprendernos por algo es el primer paso de la mente hacia el descubrimiento”, Louis Pasteur

“In the field of observation, chance favors only the prepared minds”, Louis Pasteur

Acknowledgments

I would like to thank my advisor, Dr. Richey Davis, for his support and knowledge, for giving me the strength to keep working every day, for believing in my skills and capacities and always giving me advice and support to improve my communication and scientific skills; he was a true inspiration. I want to thank my co-advisor Dr. Judy S. Riffle; I admire her professional life and I learned many valuable skills from her. She always believes in me and teaches and guides me in the right direction. Finally, I would like to thank the member of my committee, Dr. Kevin Edgar, thank you for your advice, support, and always listening to me. I really admire your patience and knowledge.

I want to thank the members of my group, Dr. William C. Miles, Dr. Akhilesh Garg, Sharavanan Balasubramaniam, and Adam Larkin. I want to thank Dr. William C. Miles and Dr. Akhilesh Garg for incorporating me into the research group and for teaching and introducing me to many laboratory and experimental techniques. I want to thank Sharavanan Balasubramaniam for guiding, revising, and being part of my master research work. Finally, I want to thank Adam Larkin to help me in many duties in the laboratory.

I want to thank my colleagues in Dr. Riffle's group. Without them and their skills to synthesize new materials, none of this work could have been possible. They include Oguzhan Celebi, Dr. Philip P. Huffstetler, and John Boyd.

I would like to thank Riley Chan for his ability to design any possible idea and fix any problem, and Angie Flynn, Diane Cannaday, Tina Kirk, Michael Vaught, Nora Bentley, and Mary Jane for all their assistance and time.

I am also thankful for my financial support from: NSF/ARC Materials World Network for the Study of Macromolecular Ferrofluids (DMR-0602932), Omnova Solutions, NSF IGERT Grant #DGE-0114346, NSF MILES-IGERT program, Institute for Critical Technology and Applied Science at VT. Also, I want to thank Professor Robert K. Prud'homme for advice and help in constructing the mixer.

I want to thank all my colleagues and friends for all their unconditional support. I want to thank my colleagues and friends Sharavanan Balasubramaniam, Nikorn Pothayee, Nipon Pothayee, Dr. Michael Vadala, Tim Vadala, Oguzhan Celebi and Lindsay Johnson. I also thank

my friends Dr. Fernando Navarro, Soco Navarro, Hans-Werner Van Wyk, and Gregorio Velez, thank you for all your favors and supports.

I am grateful to my family: my parents, Federico A. Mejia Pardo and Rosalba Ariza-Pinzon, my brother, Juan Manuel Mejia-Ariza, he is another truly inspiration in my life. My cousin Eliana Lopez-Mejia, she is like my sister and thank you for her truly love and friendship. Finally, I want to thank my fiancé Thomas Weinhart, he helped me to understand many scientific concepts. I love you all and thank you for supporting me in the bad and good moments during my life.

Attribution

Mr. Oguzhan Celebi at Virginia tech synthesized the magnetite coated with oleic acid and oleylamine discussed in the third section.

Mr. Sharavanan Balasubramaniam at Virginia Tech synthesized magnetite coated with oleic acid discussed in the fourth section.

Dr. Philip P. Huffstetler at Virginia Tech synthesized magnetite coated with oleic acid discussed in the fourth section.

Dr. Judy S. Riffle at Virginia Tech served as a collaborator and co-adviser and was directly involved in the project design and review of publications directly from this work.

Dr. Richey Davis at Virginia Tech was my principal advisor throughout my graduate career. He supervised the overall work, including the review of this document.

Nomenclature

A_{is}	Area of the inlet stream (m^2)
A_{mixer}	Area of the mixer (m^2)
B	Magnetic moment ($m^2 \cdot A$)
B_0	External magnetic moment ($m^2 \cdot A$)
$c(R)$	Solubility of a particle with radius R (g/mL)
c^*	Solubility at equilibrium (g/mL)
C_f	Final concentration of organic material (g/mL)
C_i	Initial concentration of organic material (g/mL)
C_M	Curie constant
C_{cwc}	Critical water concentration (mg/mL)
C_∞	Bulk solubility (g/mL)
C_{cmc}	Critical Micelle Concentration (mg/mL)
d_{is}	Diameter of the inlet streams (m)
D	Diffusion coefficient (m^2/s)
D_I	Intensity diameter (nm)
D_V	Volume diameter (nm)
D_N	Number diameter (nm)
DI-water	Deionized water
DLS	Dynamic Light Scattering
D_{mixer}	Diameter of the mixer (m)
D_{os}	Diameter of the outlet stream (m)
F127	Pluronic™ F127
F	Flow rate (m^3/min)
$G(\tau)$	Autocorrelation function
ΔG	Free energy change (J)
h_{mixer}	height of the mixer (m)
I	Scattering intensity
J	Nucleation rate (number of nuclei / $m^3 \cdot s$)
K_B	Boltzmann constant ($m^2 \text{ kg s}^{-2} \text{ K}^{-1}$)

K_{eff}	Isotropy constant
K_n	Equilibrium constant
l	Dilution factor (v/v)
LSW	Lifshitz, Slyozov, and Wagner
m_i	Mass rate of inlet stream (g/s)
m_{mag}	Mass of magnetite measured by TGA (mg)
m_{oa}	Mass of oleic acid measured by TGA (mg)
m_p	Mass of polymer measured by TGA (mg)
m_T	Total mass in clusters measured by TGA (mg)
M	Molecular weight (g/mol)
MIVM	Multi-Inlet Vortex Mixer
M_o	Initial magnetic moment ($\text{m}^2 \cdot \text{A}$)
MPIO	Micrometer-sized Paramagnetic Iron Oxide
M_{xy}	Transverse magnetization ($\text{m}^2 \cdot \text{A}$)
M_z	Longitudinal magnetization ($\text{m}^2 \cdot \text{A}$)
NMV	Net Magnetization Vector
N_A	Avogadro's number (mol^{-1})
n_i	Molecule
p	Vapor pressure (N / m^2)
p_0	Bulk saturation pressure (N / m^2)
P	Energy (J/s)
PDI	Polydispersity Index
Q_i	Flow rate of the inlet streams (m^3/s)
R	Radius (nm)
r_i	Relaxivity ($\text{mmol}^{-1} \cdot \text{sec}^{-1}$)
R_c	Critical nucleus radius (nm)
R_i	Relaxation rates (1/s)
R_g	Gas constant ($\text{J K}^{-1} \text{mol}^{-1}$)
Re	Reynolds number (dimensionless)
RF	Radiofrequency (Hz)
R_H	Hydrodynamic radius (nm)
S	Supersaturation values (dimensionless)

SPIO	Superparamagnetic Iron Oxides
t	Duration of injection of inlet streams (min)
t_D	Characteristic diffusion time (min)
T	Temperature of the system ($^{\circ}\text{C}$)
T_1	Spin-lattice interaction relaxation (s)
T_{1w}	T_1 -weighted images (s)
T_2	Spin-spin interaction relaxation (s)
T_{2w}	T_2 -weighted images (s)
T_2^*	Total relaxation time (s)
T_B	Blocking temperature ($^{\circ}\text{C}$)
T_c	Curie temperature ($^{\circ}\text{C}$)
TE	Echo time (min)
TEM	Transmission Electron Microscopy
TGA	Thermogravimetric Analysis
THF	Tetrahydrofuran
TR	Repetition time (min)
USPIO	Ultrasmall Superparamagnetic Iron Oxides
u_i	Velocity of the inlet streams (m/s)
V	Particle volume (m^3)
V_{is}	Volume of the inlet streams (m^3)
V_{mixer}	Volume of the mixer (m^3)
V_M	Molecular volume (m^3/mol)
V_s	Solute volume (m^3)
w_{fi}	weight fraction of material in solution (w/w))
x_i	Mass fraction (w/w)

Greek Notation:

β	Size parameter (dimensionless)
ζ	friction factor (kg/sec)
ξ	The number of polymer chains per nm^2
ϵ	Energy dissipation rate ($\text{J/s}\cdot\text{kg}$)
ϵ_0	Polarizability in vacuum ($\text{A}^2\cdot\text{s}^4\cdot\text{kg}^{-1}$)
α	Mass ratio between magnetite and oleic acid-oleylamine (dimensionless)

α_l	The capillary length (m)
λ_o	Wavelength in vacuum (nm)
λ	Wavelength of light in the medium (nm)
λ_K	Kolmogorov length scale (m)
η_l	Viscosity of the inlet streams (mPa·s)
ν_i	Kinematic viscosity of the inlet streams (m ² /s)
ρ_i	Density of the inlet streams (kg/m ³)
$\tau_{\text{diffusion}}$	Diffusion time (ms)
τ_{cf}	Cluster formation time (ms)
τ_{mix}	Mixing time (ms)
τ_{ng}	Nucleation and growth time (ms)
τ_{sa}	Self assembly time (ms)
τ_{res}	Residence time (min)
ϕ_i	Volume fraction of inlet stream (v/v)
μ_p^θ	Chemical potential of the particle (J)
μ_l^θ	Chemical potential of the liquid (J)
γ	Surface free energy (J/m ²)
γ_{sl}	Solid-liquid interfacial tension of the solute (N/m)
χ_{abs}	Absorbance efficiency factor (dimensionless)
χ_{sec}	Scattering efficiency factor (dimensionless)
χ_M	magnetic susceptibility (dimensionless)
γ_{ps}	Particle-solution surface free energy (N/m)
ω_0	Larmor frequency (MHz)
γ_0	Gyromagnetic ratio (MHz/T)
γB_s	susceptibility effect (s ⁻¹)
ρ	Density (g/mL)

Table of Contents

Dedication.....	iii
Acknowledgments.....	iv
Attribution.....	vi
Nomenclature.....	vii
Table of Contents.....	xi
List of Figures.....	xiii
List of Tables.....	xv
1 Introduction and overview of the research.....	1
1.1 Objective 1: Design and Characterization of the Multi-Inlet Vortex Mixer to form uniform nanoparticles.....	2
1.2 Objective 2: Formation of Colloidally Stable Magnetite Nanoparticle Clusters by Rapid Precipitation.....	3
2 Literature Review.....	5
2.1 Biological Materials.....	7
2.2 Medical imaging.....	9
2.3 Nucleation and Growth.....	24
2.4 Continuous mixer techniques.....	28
2.5 Flash Nanoprecipitation of organics.....	32
2.6 Dynamic Light Scattering (DLS).....	32
3 Design and Characterization of the Multi Inlet Vortex Mixer to form uniform nanoparticles.....	37
3.1 Abstract.....	37
3.2 Introduction.....	38
3.3 Materials and Methods.....	42
3.4 Discussion of Results.....	50
3.5 Conclusions.....	67
3.6 Acknowledgements.....	67
4 Formation of Colloidally Stable Magnetite Nanoparticle Clusters by Rapid Precipitation.....	68
4.1 Abstract.....	68
4.2 Introduction.....	68
4.3 Experimental Section.....	70
4.4 Results and Discussion.....	76
4.5 Conclusions.....	87
4.6 Acknowledgements.....	88

5	Conclusions and Future Work	89
5.1	Conclusions.....	89
5.2	Future work.....	90
	Appendix A: Geometry and dimensions of the MIVM	92
	Appendix B: Appendix C - Physical Properties of Solvents Used	93
	Appendix C: Calculations for the MIVM in Excel	94
	References	96

List of Figures

Figure 1.1- Flash nanoprecipitation of oleic acid-coated magnetite clusters.....	4
Figure 2.1. Types of magnetic behavior	10
Figure 2.2. Longitudinal relaxation. Decay of M_{xy} and regrowth of magnetization along the z-axis	15
Figure 2.3. Longitudinal relaxation	15
Figure 2.4. Transverse relaxation.....	16
Figure 2.5. Relationship between TR and T_1 contrast.	17
Figure 2.6. Relationship between TE and T_2 contrast.	18
Figure 2.7. Free energy of water droplet in vapor versus nucleus radius	25
Figure 2.8. Schematic for the Multi-Inlet Vortex Mixer	31
Figure 2.9. Flash NanoPrecipitation for Beta-Carotene.....	32
Figure 2.10. Electric field coordinates relative to the oscillating charge.....	35
Figure 3.1. Schematic for the Multi-Inlet Vortex Mixer	38
Figure 3.2. Flash NanoPrecipitation for Beta-Carotene.....	42
Figure 3.3. Schematic for the Multi-Inlet Vortex Mixer	45
Figure 3.4. Flash Nanoprecipitation of clusters	46
Figure 3.5. Intensity diameter for Beta-carotene nanoparticles at different Reynolds numbers ..	54
Figure 3.6. TEM image of individual magnetite nanoparticles for Batch 1	55
Figure 3.7. TEM image of individual magnetite nanoparticles for Batch 2	55
Figure 3.8. Critical micelle concentration of F127 and critical water concentration of oleic acid and oleylamine for forming clusters of magnetite at 25 °C	57
Figure 3.9. Intensity diameters of magnetite clusters.	58
Figure 3.10. TEM image of magnetite clusters prepared with $Re=21,500$ and 75 wt% of water in the mixing chamber.....	60
Figure 3.11- Images of magnetite clusters at different supersaturation values in the mixer	63
Figure 3.12. The stability of magnetite clusters at Reynolds numbers of 21,500.....	65
Figure 3.13. The stability of magnetite clusters at Reynolds numbers of 15,500.....	65
Figure 3.14. Magnetite clusters at Reynolds number of 5,000 under the influence of a magnetic field	66
Figure 4.1. Critical micelle concentration of F127 and critical water concentration of oleic acid and oleylamine coated magnetite for forming clusters of magnetite at 25 °C.....	72
Figure 4.2. Schematic illustration of the formation of copolymer stabilized-magnetite nanoparticle clusters via rapid precipitation using a Multi-Inlet Vortex Mixer	74
Figure 4.3. TEM image of oleic acid-coated magnetite nanoparticles.	77
Figure 4.4. (a) Representative particle size distributions (b) Variation of DI as a function of Reynolds number (F127:magnetite = 1:1, 75 vol % water in the mixer)	78
Figure 4.5. (a) Visualization of nanoparticles using NTA (b) Representative particle size distributions (c) Number and volume diameters using NTA (F127:magnetite = 1:1 wt/wt, 75 vol % water in the mixer).....	79
Figure 4.6. Images of magnetite clusters at Reynolds number of 2000 (F127:magnetite = 1:1, 75 vol % water in the mixer).....	83
Figure 4.7. Images of magnetite clusters formed with the injection condition F127:magnetite (0.1:1) ($Re = 15,500$, 75 vol % water in the mixer).....	84
Figure 4.8. Colloidal stability of magnetite nanoparticle clusters	86

Figure 4.9. Magnetite clusters at Reynolds number of 2000 under the influence of a magnetic field	87
Figure 5.1. Encapsulation of hydrophobic drug via Flash Nanoprecipitation	91
Figure 6.1. Schematics and dimensions of the Multi-Inlet Vortex Mixer	92

List of Tables

Table 2-2- Magnetite (Fe ₃ O ₄) properties	12
Table 2-3. Image contrasts as a function of TR and TE	18
Table 2-4. Signal intensities of different tissues on T ₁ - and T ₂ - weighted images	19
Table 2-5. Properties of T ₂ contrast agents	21
Table 2-6. Properties of T ₁ contrast agents based on inorganic nanoparticles	23
Table 2-7. Studies on r ₁ relaxivities of T ₁ contrast agents based in inorganic nanoparticles	23
Table 2-8. Different diameters for the Multi-Inlet Vortex Mixer	31
Table 2-9. Constant values for A1-A4	36
Table 3-1. Specifications for the Multi-Inlet Vortex Mixer	39
Table 3-2- Flow rates for organic and water solution in the mixer	47
Table 3-3. Intensity Diameter, Volume diameter, and PDI for Beta-carotene nanoparticle	52
Table 3-4- Summary diameter results for individual magnetite nanoparticles	56
Table 3-5. Organic and magnetite composition in clusters using magnetite from batch #1	59
Table 3-6. Estimated PEO chain density on the surface of magnetite clusters	59
Table 3-7. Intensity, Volume, and number diameters of magnetite clusters	60
Table 3-8. Intensity, Volume, and number diameters using DLS	62
Table 3-9. Volume and number diameters using Nanosight	62
Table 3-10. Organic and magnetite composition in clusters	63
Table 3-11. Experimental number of chains per 1 nm ² on the surface area of magnetite clusters	64
Table 3-12. Magnetite clusters made at Re = 5,000 aggregate after applying a magnetic field (Before dialysis procedure)	66
Table 4-1- Intensity diameters using DLS and Nanosight for clusters	80
Table 4-2. Organic and magnetite weight fraction in clusters at different Reynolds numbers	81
Table 4-3. Intensity diameters using DLS and Nanosight for clusters	82
Table 4-4. Intensity diameters using DLS and Nanosight at different supersaturation values in the MIVM. F127:magnetite 1:1 w/w, Re = 15,500.	85
Table 6-1. Different diameters for the Multi-Inlet Vortex Mixer	92
Table 7.1. Viscosities and Densities of THF and Water at 35 °C	93
Table 7.2. Viscosities and Densities of THF and Water at 25 °C	93

1 Introduction and overview of the research

In biomedicine, nanoparticles (NPs) have attracted interest for their applications in drug delivery,¹ tissue engineering,² tumor destruction via heating (hyperthermia),³ separation and purification of biological molecules and cells,⁴ Magnetic Resonance Imaging (MRI) contrast enhancement,⁵ and fluorescent biological labels.⁶ Colloidal drug carriers such as liposomes and nanoparticles, with a diameter range of 50-400 nm, are used in drug delivery and anticancer therapeutics.^{7, 8} Recently, inorganic nanoparticles such as gold nanospheres,⁹ quantum dots,¹⁰ nanoshells,¹¹ and superparamagnetic metals¹² have been used in biomedical applications such as targeting delivery, medical imaging, and separation.⁸ This is because the chemical and physical properties of nanoparticles originate from their small dimension, exhibiting different properties such as morphology, surface chemistry, reactivity, optical and magnetic properties, and circulation in the blood stream.¹³

For biomedical applications, general design requirements for nanoparticles for diagnostics and drug delivery include control of particle size, colloidal stability, biocompatibility of compounds by surface functionalization, binding of particles to proteins and to cell membranes, and biodistribution (clearance by liver & kidney; entry to tumors (Enhanced Permeability and Retention, (EPR)) and cell uptake (phagocytosis; endocytosis, pinocytosis).¹⁴⁻¹⁶

Different methods have been used to form nanoparticles such as mixing with a conventional high speed homogenizer¹⁷, Confined Impinging Jet (CIJ) mixer¹⁸, Multi-Inlet Vortex Mixer (MIVM)¹⁹, controlled dialysis²⁰, and emulsification followed by stripping²¹. The last two methods are thermodynamically controlled processes which can be slow and can result in drug/matrix separation and low drug loading.²² Using flash nanoprecipitation with the MIVM, high drug loading and formation of the complexes are kinetically controlled.^{8, 23} The CIJ mixer and MIVM have been used to create narrow particle size distributions, to control the particle size, enhance drug loading capacity, and manipulate the encapsulated component composition.^{8, 24} These methods were chosen for their ability to mix fluids in a time less than the characteristic precipitation times of organic/inorganic materials.²⁵ Two important steps are required: first, produce a region of high turbulent energy dissipation. High energy dissipation occurs for impinging jets because the kinetic energy of each jet stream is converted into a turbulent-like motion through a collision and redirection of the flow in a very small volume. Second, ensure

that the process streams for mixing pass through the high intensity region without bypassing. The first step ensures the proper scale for mixing and the second ensures that the desired molar flow ratios are preserved during the rapid mixing process.¹⁸

Functional nanoparticles that have well-defined size distributions and are colloidally stable in aqueous media are important for biomedical applications. Clusters of superparamagnetic particles are particularly interesting as magnetic resonance imaging (MRI) contrast agents. Steric stabilization of nanoparticles is important because it increases the colloidal stability, prevents aggregation between particles, and makes it possible to control particle size during the formation of nanoparticles. Thus, development of a method to control the size of sterically stabilized nanoparticles is needed.

With this brief introduction, the following sections describe the two main objectives of this thesis:

1.1 Objective 1: Design and Characterization of the Multi Inlet Vortex Mixer to form uniform nanoparticles

1.1.1 Hypothesis

We can control particle sizes of nanoparticles comprised of organic and inorganic components by controlling the Reynolds number and supersaturation values in the mixer.

1.1.2 Approach:

The importance of the MIVM is that a turbulent region can be created to provide a mixing environment necessary to create and precipitate homogeneous nanoparticles. The turbulent region is created by the momentum of the inlet streams through the mixer, where organic material and polymer stabilizer are mixed with an organic solvent (e.g. tetrahydrofuran, THF). An antisolvent (deionized water, DI-water)) is required to precipitate the hydrophobic part of the amphiphilic polymer and the organic active material. The key is that the micellization of the amphiphilic polymer and nucleation and growth of the organic active material occur almost simultaneously to create stable particles in solution, after which the amphiphilic polymer can coat the surface of the particles.^{23, 26} Steric stability of the resulting nanoparticles is due to the

repulsive steric force between the hydrophilic part of the polymers anchored to the particles. The MIVM was calibrated by forming beta-carotene nanoparticles and magnetite clusters formation stabilized by Pluronic F127, a triblock copolymer comprised of a poly(propylene oxide) (PPO) center block flanked by poly(ethylene oxide) (PEO) endblocks. Different parameters were investigated such as inlet organic concentrations, organic solvent to anti-solvent volume ratios, and the Reynolds numbers.

1.2 Objective 2: Formation of Colloidally Stable Magnetite Nanoparticle Clusters by Rapid Precipitation

1.2.1 Hypotheses

Magnetite cluster size and composition can be controlled using the MIVM via flash nanoprecipitation by controlling the Reynolds number and supersaturation value.

1.2.2 Approach:

Because of their unique behavior in the presence of a magnetic field, superparamagnetic (SPM) nanoparticles including magnetite have been used as T_2 (spin-spin or transverse relaxation time) contrast agents.²⁷ SPM nanoparticles respond to an external magnetic field as a single domain crystal and in the absence of a magnetic field, these nanoparticles will not retain any magnetization.²⁸ Also, it has been found that an increase in the size of MRI T_2 contrast agents led to a significant decrease in the T_2 relaxation time.²⁸ The reason for this behavior is that when an external magnetic field is applied, superparamagnetic iron oxide (SPIO) nanoparticles align in the direction of the magnetic field and enhance the magnetic flux. This provides substantial disturbances in the local magnetic field through large magnetic moments and leads to a rapid dephasing of surrounding protons, generating an enormous change in the MR signal images.²⁹ This suggests that polymer stabilized SPM magnetite clusters would be ideal contrast agents. We have used the MIVM to create clusters of SPM magnetite nanoparticles. The objective of the present work is to make clusters, comprised of hydrophobically modified magnetite nanoparticles (diameter ~6 nm) of magnetite coated with oleic acid dispersed in water. An amphiphilic triblock copolymer consisting of polyethylene oxide (PEO) and polypropylene oxide (PPO) (Pluronic F127) is used as the steric stabilizer. Figure 1.1 shows the flash

nanoprecipitation for magnetite clusters. The time to precipitate magnetite (cluster formation) should match the time to form a micelle (stabilization) to obtain stable magnetite clusters in solution as shown in Figure 1.1. This technique allows us to control the cluster size distribution with enhanced loading capacity.

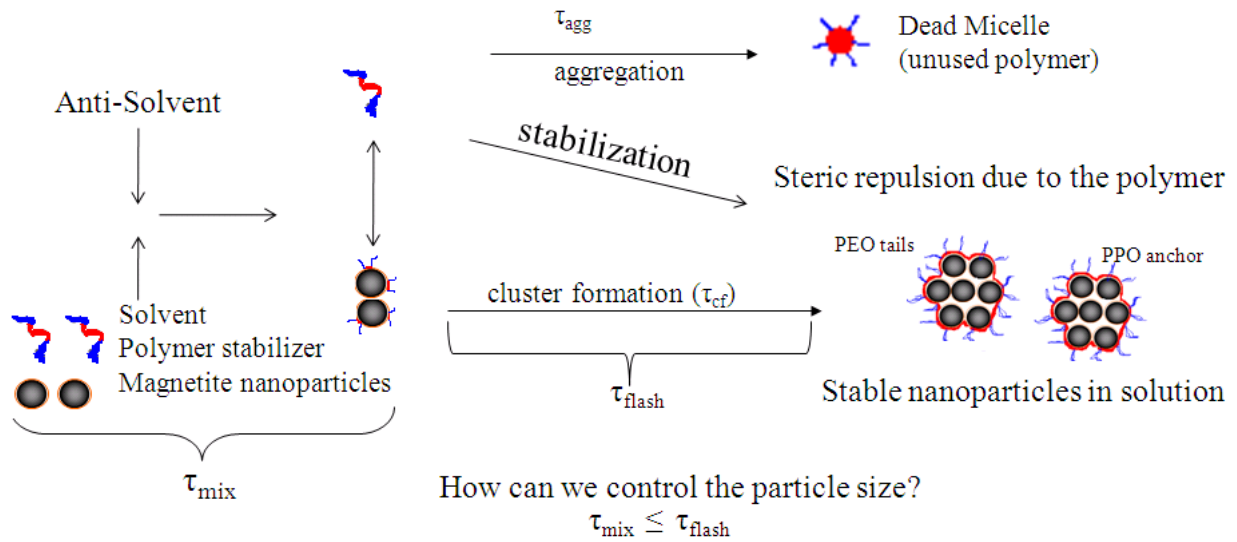


Figure 1.1- Flash nanoprecipitation of oleic acid-coated magnetite clusters modified from B. K. Johnson³⁰

2 Literature Review

This literature review is organized in the following manner. The first section explains the importance of different biological materials for use in biomedical applications such as drug delivery and imaging analysis. This includes micelles, liposomes, and block ionomer complexes. For each of these applications, advantages and examples of materials are discussed. These complex carriers are very important because they can load different types of molecules useful for different diseases. Finally, different requisites are explained to determine if these materials are suitable and safe to use in a living organism.

The second section includes the importance of using Magnetic Resonance Imaging (MRI) contrast agents. In practice, developing agents that can maximize the ability of current imaging tools is more economically feasible than developing new methods. MRI is very important because it provides real-time visualization at the organ and tissue levels in living organisms. MRI uses a powerful magnetic field to align hydrogen atoms in water in the body. In this section, different types of magnetism and properties of metal oxide such as iron oxide and magnetite are explained. Relaxivity measurements, image contrast, and nanoparticles for MRI are also topics of interest to understand the importance of inorganic nanoparticles to enhance contrast of different tissues.

The third section concerns nucleation and growth of compounds in a colloidal phase. This is very important because it explains how precipitation of particles occurs and the important parameters needed to obtain optimal precipitation. This section is divided into different subsections including homogeneous nucleation, surface nucleation, and particle formation and stability using Ostwald ripening. Nucleation theory explains how a solid phase is formed in the liquid medium. Also, it explains the role of colloidal theory to obtain particles with narrow size distribution. Here, we can study what parameters govern particle formation such as supersaturation values, interfacial energies, and physical properties of materials. The fourth section involves the theory and description of the confined impinging jet mixer and multi-inlet vortex mixer. This is important because the mixer can be well understood in order to create and control nanoparticles for biomedical applications.

The fifth section describes the flash nanoprecipitation of organic compounds that occurs in the mixer at the micromixing scale. This is important because it explains how stable particles can be formed using a stabilizer such as an amphiphilic block copolymer. Different times are relevant for forming stable nanoparticles such as the mixing time of inlet fluids, nucleation and growth of precipitation of molecules, and self-assembly of diblock polymers.

The sixth section concerns dynamic light scattering (DLS) which is very useful for measuring particle size, particularly when the particles are spheres and are relatively monodispersed in solution. This section studies nanoparticles' parameters in solution such as particle size and polydispersity. Particle size is measured in a range of 50-150 nm. Polydispersity indexes are useful to characterize the size distribution for a particle system.

2.1 Biological Materials

2.1.1 Liposomes and micelles

The most well investigated and defined drug nanocarriers are liposomes and micelles. Liposomes have been used to deliver water soluble drugs. By contrast, micelles can deliver poorly water soluble drugs.³¹

Liposomes are artificial phospholipid vesicles with a size range of 50-1000 nm. Liposomes load water soluble drugs into their hydrophilic core and sometimes water-insoluble drugs using their hydrophobic phospholipid bilayer. They are biologically inert (depending of composition), biocompatible, and they cause no toxic or antigenic reactions. Liposomes can be used like targeting ligands by binding targeting moieties such as antibodies to the liposome surface. However, they typically have short life times in the circulation. This problem can be solved by using specific binding molecules such as PEG chains.³¹

Many organic compounds are very poorly soluble in water or completely insoluble.^{32,33} These organic compounds are very important for certain applications such as pharmaceutical, dyes, and pesticides.²⁶ For that reason pharmaceutical research groups have been working to enhance the solubility of poorly soluble drugs.^{34, 35}

Micelles are very important in drug delivery because many new and current drugs are water-insoluble. Insoluble drugs have some serious problems: (1) Poor water-solubility results in poor adsorption and low bioavailability, (2) drug aggregation can occur upon intravenous administration and might lead to some complications, such as embolism and local toxicity. For these reasons, the use of micelles, particularly polymeric micelles, is very promising because they increase the solubility and bioavailability of poorly water soluble pharmaceuticals. Also, polymeric micelles can extend the blood half-life upon intravenous administration. Micelles are colloidal dispersions with a particle diameter between 5-100 nm. Because of this small particle size, micelles provide spontaneous penetration into the interstitium in the body compartments.³¹

2.1.2 Block ionomers complexes

Polymer micelles also form block copolymers composed of ionic and nonionic block known as “block ionomers”. These block copolymers have opposite charges and form block ionomer complexes by assembling themselves into core-shell micelles. These block ionomers

can encapsulate charged therapeutic molecules such as polynucleic acids into the micelle core to develop non-viral gene delivery systems. The stability of the block ionomer complexes and the amount of drug encapsulated depends on the ionic block lengths, charge density, and ionic strength of the solution. The triggered release of the active therapeutic agent depends on the pH and salt sensitivity of the block ionomer micelles.³⁶

2.1.3 Nanoparticles transport in circulation

Nanoparticles can be used in therapeutic approaches such as imaging and drug delivery systems. This is because nanoparticles can cross biological barriers throughout tissue diffusion, extravasation and escape from hepatic filtration, they can interact with cellular molecular and penetrate cells and they can conjugate with target specific biomolecules. Nanoparticles in the size range of 1-100 nm can travel through the human body lymphatic and blood vessels and they have the ability to enhance drug loading capacity and be stable in solution.³⁷

The human body has different biological barriers against foreign particles. Examples of these barriers are cellular and humoral arms from the immune system and mucosal barriers. In order to target nanoparticles in a particle site, these barriers must be overcome. Biodistribution and clearance of polymeric nanoparticles can be affected by different factors such as tissue defects, stealth properties, targeting, and nanoparticle size. Nanoparticles can overcome these biological barriers because of their unique size and amenability to surface functionalization.³⁷

The administration of therapeutic agents to tumor tissues has been limited by different factors, such as low stability, low solubility and rapid clearance. The consequences are low efficacy and a short circulation half-life of the therapeutic agent. For that reason, polymer-drug conjugates have been used to improve the blood residence times and side effects. Examples of these complexes are AP5346, PK1, PK2, Xyotax, and CT-2106 which have long circulation half-lives, passive targeting ability, and low toxicity with high dosages.³⁷

In order to use complexes of polymeric nanocarriers for targeting, they should be non-immunogenic, non-toxic, carry enough drug and release it. Polyethylene Glycol (PEG) has low toxicity, is non-immunogenicity and has already been approved by the Food and Drug Administration (FDA) to be used in humans. Polymer-drug complexes, which are conjugated with PEG are able to circulate for a long time. The advantage of PEG is its ability of absorption and covalently attaching to the surface of nanoparticles. Also, PEG provides steric repulsion between nanoparticles and reduces nonspecific interactions with proteins.³⁷

Particle size and composition are important parameters for biodistribution of long-circulating nanoparticles to achieve therapeutic efficacy. Specifically, they are important for tissue extravasation and diffusion, hepatic filtration, and kidney excretion. Results have shown that pegylated nanoparticles smaller than 100 nm reduce plasma protein adsorption on their surface and hepatic filtration. Also, these small nanoparticles have long residence times in the blood stream and a high rate of extravasation into permeable tissues.³⁷

2.2 Medical imaging

Imaging techniques are very useful in many scientific and technological applications. Developing new contrast agents that can maximize the ability of current imaging tools is more economically feasible than developing new imaging methods. A chemical compound known as an imaging probe or contrast agent is one of the most effective supplements to improve sensitivity in the image. Using a contrast agent, information-rich images can be obtained, where contrast refers to the signal differences between adjacent regions such as ‘tissue and tissue’, ‘tissue and vessel’, and ‘tissue and bone’.³⁸ For that reason, developing contrast agents is of great interest in biological and medical sciences. Various imaging techniques can be used such as computed x-ray tomography (CT), optical imaging, magnetic resonance imaging (MRI), positron emission tomography (PET), single-photon-emission computed tomography (SPECT), and ultrasound. These technologies have been used because they provide real-time visualization of cellular functions of living organisms and related with molecular interactions. They also make possible the diagnosis of diseases like cancers, neurodegenerative illnesses, and biological information and functions at preclinical stages.³⁹

2.2.1 Importance of MRI

MRI is a tomographic imaging technique that produces images of internal physical and chemical characteristics of an object by externally induced Nuclear Magnetic Resonance (NMR) signals. An MRI scanner outputs a multidimensional data array or image that represents the spatial distribution of a measured physical quantity. MRI generates two-dimensional sectional images at any orientation, three-dimensional volumetric images, and four-dimensional images. Moreover, since it does not require the injection of radioactive isotopes into the object for signal generation, images can be formed directly from the object itself.³⁹ Consequently, this is one of

the most powerful diagnostic tools in medical science and is a preferred tool for imaging the brain and central nervous system, to assess cardiac function, and to detect tumors. It is a very important tool for molecular and cellular imaging because it gives anatomic images of soft tissue with a typical in-plane spatial resolution of $1.4 \times 1.9 \text{ mm}^2$ for a 256×144 matrix.⁴⁰ To properly understand MRI, it is useful to first review some fundamental concepts in magnetism.³⁸

2.2.1.1 Magnetism

There are four different types of magnetism: paramagnetism, ferromagnetism, antiferromagnetism, and ferrimagnetism. They depend on the ordering (or randomness) of the spins of the unpaired electrons that are randomly oriented on different atoms. Figure 2.1 shows these different types of magnetism.⁴¹

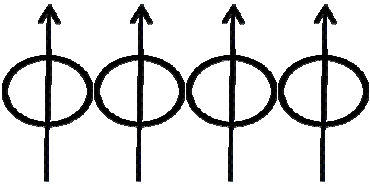
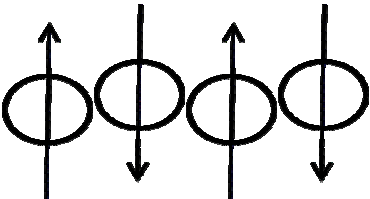
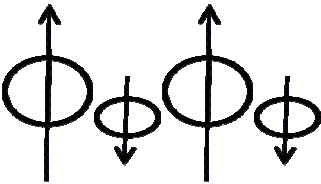
(a) Spontaneous domain formation:	(b) No domains:
<p>1. Ferromagnetism</p> 	<p>1. Paramagnetism No long range order; alignment under a magnetic field</p>
<p>2. Antiferromagnetism</p> 	<p>2. Diamagnetism No long range order; alignment opposes field</p>
<p>3. Ferrimagnetism</p> 	

Figure 2.1. Types of magnetic behavior modified from R. E. Rosensweig⁴²

Paramagnetic substances are attracted when a magnetic field is applied. These substances possess unpaired electrons that are randomly oriented on different atoms. Each atom, ion, or molecule is like a small magnet with its own inherent magnetic moment. When a magnetic field is applied, it causes partial alignment of these magnets parallel to the field. Such materials include liquid oxygen, rare-earth materials, and ferromagnets above their Curie temperature. In this materials the magnetic susceptibility (χ_M) varies with temperature and can be described by the Curie-Weiss law as follows:⁴¹

$$\chi_M = \frac{C_M}{T - T_C} \quad (2.1)$$

where C_M and T_C are the Curie constant and temperature. If T increases, the increased alignment of the magnetic moments in the substance is opposed by stronger thermal vibrations, and then χ_M decreases. Below the Curie temperature (which depends on the oxide itself), iron oxides experience a magnetically ordered state transition and become ferromagnetic, antiferromagnetic, or ferrimagnetic substances.⁴¹

Ferrimagnetic and ferromagnetic materials are very strongly attracted to a magnetic field. These substances contain unpaired electrons whose moments are a result of interactions between neighboring spins. Also, they are at least partially aligned in the absence of a magnetic field and have a positive spin energy.⁴¹

In ferromagnetic materials, when a magnetic field is applied, the alignments of the electrons spins are parallel. They have a net magnetic moment, a large magnetic permeability, and a large and positive susceptibility. If temperature increases, the orders of arrangement of the spins decrease due to thermal fluctuations of the individual magnetic moment and the susceptibility decreases.⁴¹

Antiferromagnetic materials have the electron spins of equal magnetic moments, and they are aligned in an antiparallel manner. They have zero overall magnetic moment, a positive permeability, and a small positive susceptibility. If temperature is increased, susceptibility increases due to the antiparallel ordering are disrupted.⁴¹

Ferrimagnetic materials are like antiferromagnetic materials that have the electron spins aligned in an antiparallel manner. The difference is that the spins have unequal moments, therefore, ferrimagnetic materials have a net magnetic moment.⁴¹

Ferromagnetic, antiferromagnetic, and ferrimagnetic materials have a domain structure with only particles in the range of 50-500 nm in size consisting of a single domain. Different domains have different spin orientations and the spins within a domain is either parallel or anti-parallel. For ferro and antiferromagnetic materials, a high magnetic field is needed to eliminate the domains. At very high magnetic field, saturation magnetization is achieved.⁴¹

Superparamagnetic materials have a magnetic anisotropy because of the existence of preferred crystallographic directions along which the electron spins are most aligned, and because the substance can be easily magnetized. These materials exhibit strong paramagnetic behavior and have large magnetic susceptibilities. When a sufficient magnetic field is applied, magnetism can be reversed along these axes. These substances can be ordered below a blocking temperature (T_B) as follows:⁴¹

$$T_B = \frac{K_{eff} V}{25K_B} \quad (2.2)$$

where K_{eff} is an isotropy constant that depends on particle size, V is the particle volume, and K_B is the Boltzmann constant.

2.2.1.2 Properties of Metal oxides (Iron oxide) and Magnetite

Iron oxides are common compounds present in almost all of the different compartments of the global system (i.e. hydrosphere, lithosphere, and biosphere). Iron oxide compounds consist of a close packed array of anions in which the octahedral and, sometimes, the tetrahedral interstices are partly filled with trivalent or divalent Fe.⁴¹

Magnetite is a ferromagnetic mineral containing Fe^{II} and Fe^{III}. Table 2-1 shows some properties for magnetite.⁴¹

Table 2-1- Magnetite (Fe₃O₄) properties modified from R. M. Cornell⁴¹

Properties	Value
Crystal system	Cubic
Cell dimension (nm)	a=0.839
Density (g/cm ³)	5.17
Néel (Curie) temperature (K)	850

Generally, almost all iron oxides exist in crystalline form. Their structures can be determined using single crystal X-ray diffraction or neutron diffraction, infrared spectroscopy, electron diffraction, and high resolution electron microscopy. X-ray diffraction has been used to determine the crystal structure of magnetite.⁴¹

2.2.2 Introduction to the Nuclear Resonance Imaging

The basic principle of MRI is based on nuclear magnetic resonance (NMR) jointly with the relaxation of proton spins in a magnetic field.^{38, 43} To create an image, Medical Magnetic Resonance (MR) imaging uses signals from the nuclei of hydrogen atoms. It uses the hydrogen atom because it contains a single proton and a single electron. The proton is the important part for this application because it has angular momentum and therefore acts like a spinning top. Also, the proton has a magnetic moment (B) and therefore behaves like a small magnet. This is important because the proton can be influenced by an external magnetic field and electromagnetic waves and when it moves, it emits an electromagnetic signal that is detected by a receiver coil. When a hydrogen nucleus is exposed to an external magnetic field (B_0), the nucleus begins to wobble (a process called precession) and gradually aligns with the magnetic field due to energy dissipation. Precession of the nuclei occurs at a frequency that is proportional to the strength of the applied magnetic field called the Larmor frequency.⁴⁴ This behavior is very important to MR imaging because this is the rate at which spins wobble when placed in a magnetic field. The Larmor frequency is defined as follows^{43, 44}:

$$\omega_0 = \gamma_0 B_0 \quad (2.3)$$

where ω_0 is the Larmor frequency (MHz), γ_0 is the gyromagnetic ratio, a constant specific to a particular nucleus (MHz/T), and B_0 is the strength of a magnetic field (T)

The magnetic field, B_0 of an MR imager is typically 60,000 times stronger than earth's magnetic field. This results in a stronger longitudinal magnitude. Spins tend to align parallel or anti-parallel to the magnetic field. Under steady-state conditions, slightly larger fractions align parallel to the magnetic field. This small difference produces the measurable net magnetization (M_z) that is represented by the net magnetization vector (NMV). Energy can be applied to a spin system by applying an electromagnetic wave of the same frequency as the Larmor frequency. This is called the resonance condition. This electromagnetic wave is generated by a powerful

radio transmitter and applied to the object to be imaged. This energy absorption is known as the excitation of the spin and it results in a longitudinal magnetization more tipped away from the z axis toward to the transverse xy- plane perpendicular to the direction of the main magnetic field. By applying a radiofrequency (RF) pulse, that is strong enough and applied to tip the magnetization by 90° , all the longitudinal magnetization is rotated into the transverse plane resulting in a transverse magnetization, M_{xy} . When transverse magnetization is present, it precesses about the z-axis and emits a signal at the same frequency as the Larmor frequency in a receiver coil: the MR signal. This signal is measured and processed by receivers and computers to generate an image.

2.2.3 Relaxation time and rate

After the spins have been excited, the magnetization rotates into the xy plane called the transverse magnetization (M_{xy}). The MR signal collects the M_{xy} in the receiver coil. The MR signal is rapidly reduced by two independent processes which reduce M_{xy} and cause a return to the stable state present before excitation. These processes are called spin-lattice interaction (T_1 relaxation) and spin-spin interaction (T_2 relaxation).

2.2.3.1 Longitudinal Relaxation

Transverse magnetization decays and the magnetic moments realign with the z-axis of the main magnetic field. The transverse magnetization remaining in the xy-plane decreases slowly, proportionally with the MR decay. As M_{xy} decays, the longitudinal magnetization, M_z is slowly restored. This process is called longitudinal relaxation or T_1 recovery as shown in Figure 2.2. The nuclei can return to the ground state by dissipating the excess of energy to their surroundings. T_1 is the time constant for this recovery and depends on the strength of the magnetic field and Brownian motion of the molecules.⁴⁴

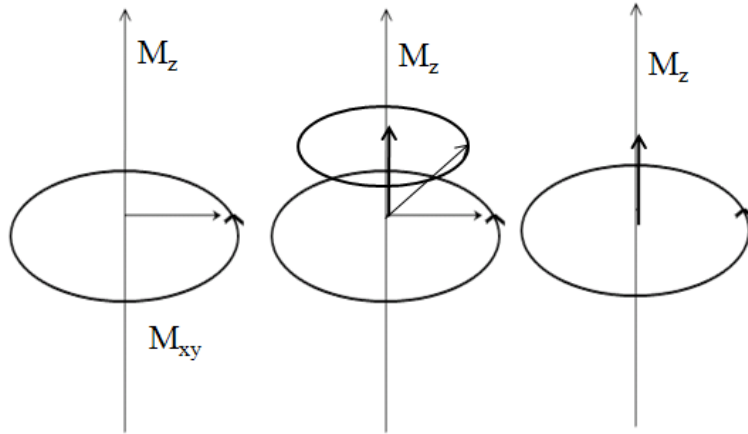


Figure 2.2. Longitudinal relaxation. Decay of M_{xy} and regrowth of magnetization along the z-axis modified from D. Weishaupt⁴⁴

T1 relaxation restores M_z as a function of time as shown in the following equation and Figure 2.3.⁴⁵

$$M_z(t) = M_0(1 - e^{-t/T_1}) \quad (2.4)$$

where M_0 is the initial magnetic moment, t is the time measured after the RF pulse, and T_1 is the longitudinal relaxation time.⁴⁵

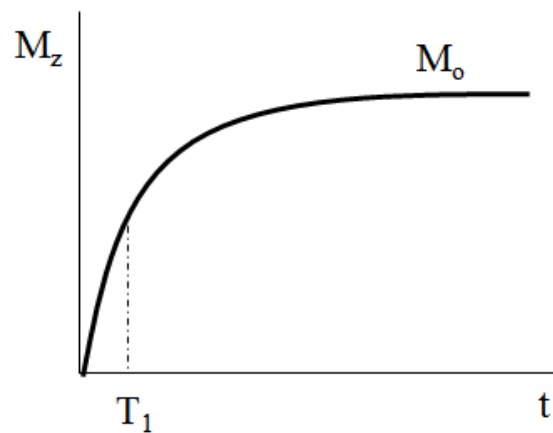


Figure 2.3. Longitudinal relaxation modified from H. B. Na et al.⁴⁵

2.2.3.2 Transverse Relaxation

After excitation, spins start to dephase until the transverse magnetization disappears. The dissipation of the transverse magnetization, M_{xy} can be shown in the following equation and Figure 2.4.⁴⁴

$$M_{xy}(t) = M_{xy} e^{-t/T_2} \quad (2.5)$$

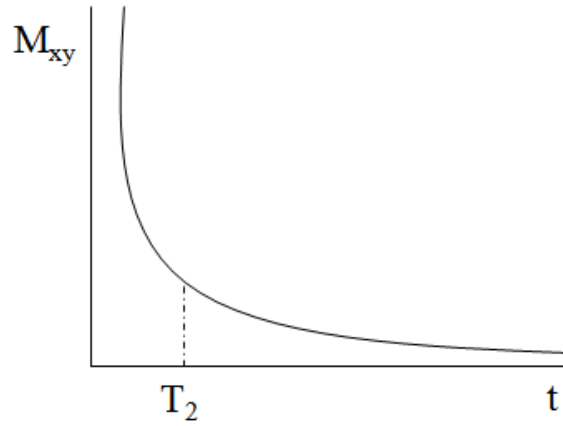


Figure 2.4. Transverse relaxation modified from B. N. Hyon⁴⁶

In summary, transverse relaxation is the decay of transverse magnetization when spins lose coherence or dephase.⁴⁴ Transverse relaxation is different from longitudinal relaxation in that the spins do not dissipate energy to their surroundings apart from exchanging energy among one another. T_2 and T_1 are completely independent of each other and occur almost simultaneously. The recovery of longitudinal magnetization M_z due to T_1 relaxation occurs between 0.5-5 sec while the decrease in the MR signal due to T_2 occurs between 100-300 msec.⁴⁴ To measure the relaxivities (R_1 and R_2), we need T_1 and T_2 and the concentration of the contrast agent, $[M]$ as shown in the following equations.⁴⁷

$$R_1 = \frac{1}{T_1[M]} \quad \text{and} \quad R_2 = \frac{1}{T_2[M]} \quad (2.6)$$

2.2.4 Contrast imaging

Three intrinsic features contribute to the signal intensity or brightness of an MR image and hence the image contrast. The three intrinsic features are the proton density, T_1 time, and T_2 time. The proton density is the number of excitable spins per unit volume and determines the maximum signal that can be obtained from a given tissue. The T_1 time of a tissue is the time required for the excited spins to recover and be accessible to the next excitation. T_2 time determines how quickly an MR signal fades after excitation of the spins. These intrinsic features can vary from one tissue to another. The resulting MR images can differ in their tissue-tissue

contrast depending on which of these parameters is emphasized. Because of these differences, tissues can be imaged by MRI. Images in which proton density is emphasized are called proton density weighted. Contrast images that are determined by T_1 are known as a T_1 -weighted image (T_{1w}). Contrast images that are determined by T_2 is known as a T_2 -weighted image (T_{2w}).⁴⁴

In order to produce a MR image, a slice must be excited and the resulting signal should be recorded many times. Repetition Time (TR) is very crucial to T_1 . TR is the length of the relaxation period between two excitation pulses. TR contributes to the re-growth of longitudinal magnetization. If more longitudinal magnetization is excited with the next RF pulse, a larger producing MR signal can be collected. Tissues with a short T_1 (less than 600 msec) relax quickly and give a large signal after the next RF pulse producing a bright image. Tissues with a long T_1 appear dark on an image as shown in Figure 2.5.⁴⁴

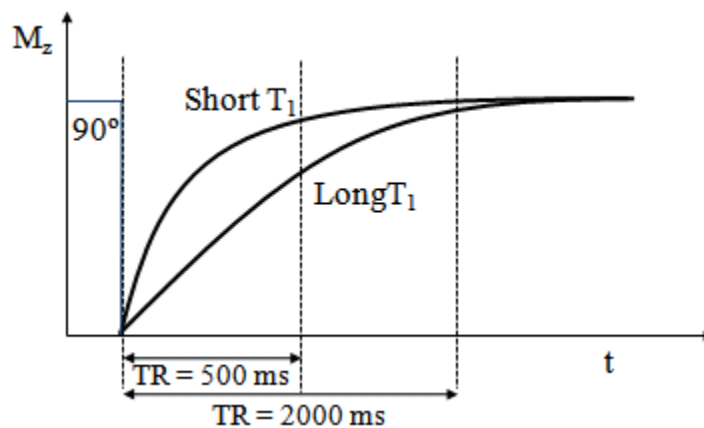


Figure 2.5. Relationship between TR and T_1 contrast. (a) Tissues with a short T_1 appear bright. (b) Tissues with a long T_1 appear dark modified from D. Weishaupt⁴⁴

Echo time (TE) is the interval between application of the excitation pulse and collection of the MR signal and depends on T_2 . Tissues with short T_2 lose most of their signal and appear dark. If a long TE is used (over 60 msec), tissues are depicted with different signal intensities on the MR image and produce a strong signal, thereby appearing bright on the MR image as shown in Figure 2.6. The relationship between TR and TE and the resulting imaging contrast are summarized in Table 2-2 and Table 2-3 lists the signal intensities of different tissues on T_{1w} and T_{2w} images.⁴⁴

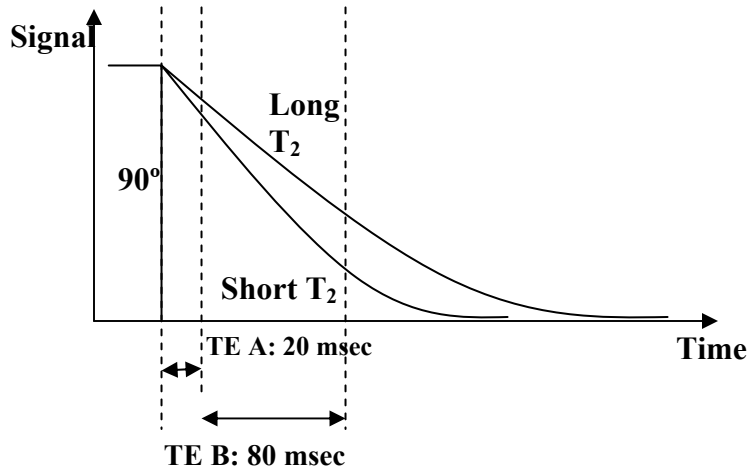


Figure 2.6. Relationship between TE and T₂ contrast. (a) Tissues with a short T₂ appear dark. (b) Tissues with a long T₂ appear bright modified from D. Weishaupt⁴⁴

Table 2-2. Image contrasts as a function of TR and TE modified from D. Weishaupt⁴⁴

	TE	TR
T _{1w}	Short	Short
T _{2w}	Long	Long
Proton density-weighted (intermediate-weighted)	Short	Long

Table 2-3. Signal intensities of different tissues on T₁- and T₂- weighted images modified from D. Weishaupt⁴⁴

Tissue	T_{2w}	T_{1w}
Fat	Bright	Bright
Aqueous liquid	Bright	Dark
Tumor	Bright	Dark
Inflammatory tissue	Bright	Dark
Muscle	Dark	Dark
Connective tissue	Dark	Dark
Hematoma, acute	Dark	Dark
Hematoma, subacute	Bright	Bright
Fibrous cartilage	Dark	Dark
Hyaline cartilage	Bright	Bright
Compact bone	Dark	Dark
Air	No signal	No signal

2.2.5 Different types of nanoparticles used in MRI

Different types of nanoparticles have been used as contrast agents. Examples of these are gadolinium-labeled nanoparticles such as liposomes, micelles, microemulsions, lipoproteins, viruses, and carbon nanotubes^{38, 48} These nanoparticles are contrast agents suitable for T₁-weighted MRI due to the paramagnetism of this element.⁴⁸ Superparamagnetic iron oxides (SPIOs) have been exploited to persuade contrast for T₂-weighted MRI. Targeted imaging is possible because nanoparticles have a large surface area and can be conjugated with biological and targeting probes, such as antibodies, oligonucleotides, and other imaging probes. Inorganic nanometer-sized colloidal particles have been extensively used in many imaging systems because of their many useful electronic, optical, and magnetic properties, which are derived from their compositions and nanometer sizes. Nanoparticle-based MRI contrast agents with targeting capabilities are composed of three parts: i) the core nanoparticles, which generate the signal

enhancement, ii) the water-dispersible shells, which endow compatibility in the biological environment, and iii) the bioactive materials for targeting purposes.⁴⁶

2.2.5.1 Inorganic Nanoparticles for T₂ Contrast Agents

Inorganic nanoparticles have been used in MRI contrast agents due to their unique properties, such as large surface area and the efficient contrasting effect.⁴⁶ Iron oxide nanoparticles less than 50nm in diameter can enhance the capabilities of available medical imaging techniques. Particles composed of iron oxide have been studied as magnetic contrast agents over a period of 45 years. Iron oxide nanoparticles have been used to target-specific in vivo or in vitro imaging, monitoring the migration and tracking, and in disease-targeted imaging.⁴⁶ Magnetic nanoparticles have proved useful in biomedical applications using SPIOs cores of magnetite or maghemite. Also, they have been used for their ability to shorten T₂ relaxation times in the liver, spleen, and bone marrow.⁴⁶

When an external magnetic field is applied to SPIO nanoparticles, their moments align in the direction of the magnetic field and enhance the magnetic flux. This provides substantial disturbances in the local magnetic field through large magnetic moments and leads to a rapid dephasing of surrounding protons, generating an enormous change in the MR signal images.²⁹ The imaging capability is not from the SPIOs intrinsically, but from their influence on longitudinal and transverse relaxation of the surrounding nuclei. This behavior reduces the T₂ time and generates sufficient T₁.²⁹ SPIOs possess both high R₁ and R₂ relaxivities. After the magnetic field is removed, Brownian motions randomize the SPIO and prevents the aggregations of SPIO nanoparticles due to magnetic attraction in solution.²⁹ The interaction between electrons and the hydrogen nuclei causes a loss of transverse coherence that produces T₂ relaxation of tissues. Transverse relaxation is influenced by inhomogeneous magnetic fields. This is because local magnetic field gradients can be induced by the differences in the magnetic susceptibility between the neighboring, different tissues, and by contrast agents. The total relaxation time (T₂^{*}) can be described as:

$$\frac{1}{T_2^*} = \frac{1}{T_2} + \gamma B_s \quad (2.7)$$

where γB_s is the relaxation by the field inhomogeneities and is called the susceptibility effect. SPIO nanoparticles are used besides other particles such as ferromagnetic or paramagnetic materials because when an external magnetic field is applied, they exhibit strong magnetization causing microscopy field inhomogeneity and activate the dephasing of protons. For that reason, SPIOs nanoparticles shorten T_2 and T_2^* relaxation times of the neighboring regions. This produces a decreased signal intensity in T_2 - and T_2^* -weighted MR images.⁴⁶

T_2 shortening by magnetic nanoparticles is due to the dephasing of the magnetic moments because of the magnetic-field gradients created by the small magnetization particles. The major relaxation is the dipolar outer-sphere interaction between the water protons spins and the magnetic moment of the nanoparticles.

To produce the most efficient T_2 contrast agents, two magnetic properties of nanoparticles have to be controlled, namely: (a) intrinsic material properties such as composition and crystal structure, and (b) extrinsic material properties such as size and shapes. Most T_2 contrast agents are based on iron oxide nanoparticles. Cheon and coworkers observed that larger iron oxide nanoparticles have large magnetization and high relaxivities (r_2). Table 2-4 shows two examples of T_2 contrast agents.⁴⁶

Table 2-4. Properties of T_2 contrast agents modified from B. N. Hyon ($B_0(T)$ is 1.5) ⁴⁶

Name	Core Material	Surface	Diameter of core (nm)	Hydrodynamic diameter (nm)	Magnetization (emu g^{-1})	r_2 [$\text{mM}^{-1}\text{S}^{-1}$]
Ferumoxides (Feridex)	Fe_3O_4 , γ - Fe_2O_3	Dextran	4.96	160	45	120
Ferumoxtran (combidex)	Fe_3O_4	Dextran	5.85	35	61	65

2.2.5.2 Nanoparticles for T_1 Contrast Agents

During the last 20 years, most nanoparticulate contrast agents have been T_2 contrast agents composed of iron oxides. Different MRI contrast agents have been commercialized such as Feridex, Resovist, and Combidex, which are superparamagnetic iron oxide (SPIO) or ultra small superparamagnetic iron oxide (USPIO) agents. These agents have several disadvantages that limit clinical applications. For example, they produce a signal-decreasing effect. This results

in a dark signal that can be confused with other pathogenic conditions and renders images of lower contrast than T_1 contrasted images. Also, T_2 contrast agents induce distortion of the magnetic field on neighboring normal tissues. This background distortion is known as the “blooming effect” and it generates and demolishes the background around the lesions. Because of these effects, most clinically used MRI contrast agents are gadolinium-complex based T_1 agents. T_1 relaxation is the equilibration of M_z after a RF pulse is applied. The change of M_z is due to an energy transfer between the proton spin system and the nearby matrix of molecules. Biological systems are composed of different molecules and organisms, and they have different relaxation behaviors and T_1 relaxation times. Paramagnetic ions near the tissues improve its relaxation and shorten the T_1 relaxation time. Examples of these paramagnetic ions are transition and lanthanide metal ions with a large number of unpaired electrons such as Gd^{3+} , Mn^{2+} , and Fe^{3+} . The advantage of T_1 compared to T_2 is that T_1 contrast agents produce positive images by signal enhancing, which maximizes the strength of MRI, that is, anatomic imaging with high spatial resolution. Their bright signal can also be distinguished clearly from other pathogenic or biological conditions. The majority of T_1 contrasting agents are paramagnetic. Due to the toxicity of heavy metal ions, contrast agents using them are in the form of ionic complexes with chelating ligands, which are thermodynamically and kinetically stable and less toxic. Most of the T_1 contrast agents reside within the extracellular space, and they interact with the blood. For that reason, they have some limitations as molecular probes for longer time tracking. An effective T_1 agent needs the ratio between the transverse and longitudinal (r_2/r_1) to be low. This means nanoparticles must have large paramagnetism (r_1) or negligible magnetic anisotropy (small r_2). The dependence of magnetic properties on a preferred direction is called magnetic anisotropy. Examples of large paramagnetic materials are lanthanide metals because their surface contains large amounts of metal ions with high magnetic moments such as gadolinium-based ones.

Table 2-5 and Table 2-6 show the physical properties and relaxivities of some T_1 contrast agents based on inorganic nanoparticles.⁴⁶

Table 2-5. Properties of T₁ contrast agents based on inorganic nanoparticles modified from B. N. Hyon⁴⁶

Name	Core Material	Surface	Diameter of core (nm)	Hydrodynamic diameter (nm)
PEG-Gd ₂ O ₃	Gd ₂ O ₃	PEG	2.2	
GadoSiPEG	Gd ₂ O ₃	Polysiloxane-PEG	3.8	3.3
			4.6	5.2
GdF ₃ :cit	GdF ₃	Citric acid		8.9

Table 2-6. Studies on r₁ relaxivities of T₁ contrast agents based in inorganic nanoparticles modified from B. N. Hyon⁴⁶

Name	Core Material	Diameter of core (nm)	Relaxivities based on concentration of whole atoms		B ₀ (T)
			r ₁ [mM ⁻¹ s ⁻¹]	r ₂ [mM ⁻¹ s ⁻¹]	
PEG-Gd ₂ O ₃	Gd ₂ O ₃	3	9.4	13.4	1.5
GadoSiPEG	Gd ₂ O ₃	2.2	8.8	11.4	
		3.8	8.8	28.8	
		4.6	4.4	28.9	
GdF ₃ :cit			3.17		14.2

2.2.5.3 Effect of particle size

Particle size is a very important parameter for magnetic particles used as MRI contrast agents for several reasons. Iron oxides are excellent contrast agents for MRI in a range from 1 nm to 1 μm. The size of nanoparticles is important in the excretion of the particles from the body.⁴⁸ For example, the diameters and surface characteristics of SPIO nanoparticles contrast agents are very important for clearance, cell response, and toxicity.²⁹ Some authors showed that nanoparticles with diameter equal to or smaller than 5.5 nm are excreted through the renal system.^{46, 48} Because the biological distribution is dependent on size, they have been classified as follows: (a) micrometer-sized paramagnetic iron oxide (MPIO, within several micrometers); (b) superparamagnetic iron oxide (SPIO, within hundreds of nanometers); and (c) ultra small

superparamagnetic iron oxide (USPIO, less than 50 nm).⁴⁸ The size of nanoparticles can be controlled by the component used in the synthesis and also by the coating used in the surface of the nanoparticles as discussed elsewhere in this chapter.

2.3 Nucleation and Growth

This thesis concerns the use of a continuous mixer technique to form nanoparticles for different biomedical applications. A key issue in this process is the controlled nucleation and growth of nanoparticles from soluble precursors. This section provides a review of relevant concepts in nucleation phenomena needed for understanding the mixing process.

For species that can crystallize, a new phase formation during precipitation depends on two stages: nucleation (the formation of centers of crystallization) and crystal growth. The relative rate of these processes determines the particle size of the precipitate formed. A colloidal dispersion can have a homogeneous mixture when a proper surfactant is used and when a high initial nucleation is obtained. The initial rate of nucleation depends on the degree of supersaturation that can be reached before phase separation occurs. The particle growth rate mainly depends on the following factors:⁴⁹

- The amount of material available.
- The viscosity of the medium. This parameter controls the rate of diffusion of the material to the particle surface.
- How easily the material is correctly oriented and incorporated into the crystal lattice of the particle if the particle is indeed crystalline.
- Adsorption of impurities on the surface of the particle. These impurities can act as growth inhibitors.
- Aggregation between particles

2.3.1 Homogenous nucleation

A new phase should nucleate so that the surface free energy of the new interface makes nucleation. This is important to explain the nucleation of a liquid phase from a vapor phase with a pressure p to form a drop with radius R as shown in equation 2.8. The free energy change (ΔG) to achieve the latter case is shown as follows:⁵⁰

$$\Delta G = -nkT \ln\left(\frac{p}{p_o}\right) + 4\pi R^2 \gamma = -\frac{3}{4} \pi \frac{R^3}{V_M} K_B T \ln\left(\frac{p}{p_o}\right) + 4\pi R^2 \gamma \quad (2.8)$$

where p is the vapor pressure, p_0 is the bulk saturation pressure, V_M is the molecular volume, K_B is the Boltzmann constant, and γ is the surface free energy.

Using Eq. (2.8) when $p > p_0$, the first parameter on the right hand will make $\Delta G < 0$ for very large R . For small R , the positive second term will dominate. A maximum of ΔG will occur with an intermediate value of R as shown in Figure 2.7.

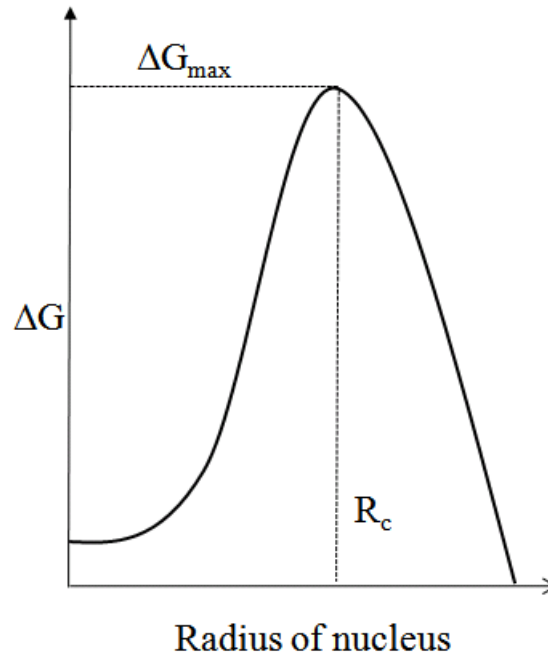


Figure 2.7. Free energy of water droplet in vapor versus nucleus radius modified from D. Fennell Evans⁵¹

At this maximum, p can be related to the radius as follows:

$$kT \ln\left(\frac{p}{p_0}\right) = \frac{2\gamma V_M}{R_c} \quad (2.9)$$

In Figure 2.7, if $R < R_c$, vaporizing the liquid gains free energy. If $R > R_c$, condensing more vapor on the drop gains free energy and leads to the formation of a bulk liquid phase.⁵⁰

For the case of a solute in a liquid slightly above its saturation concentration c_s , a similar nucleation procedure will occur. Changing the role of the vapor pressure p from previous equation to the solute concentration c and p_0 for c_s , the resulting Kelvin equation will be:

$$K_B T \ln\left(\frac{c}{c_s}\right) = \frac{2\gamma V_s}{R_c} \quad (2.10)$$

where γ is the surface free energy solution-precipitate, V_s is the solute volume, R_c is the particle's radius that by thermodynamics will nucleate forming a bulk solid.⁵⁰

Ring⁵² has employed a term when an embryo is subcritical and a nuclei is supercritical in size. Then, the equilibrium of number density of embryos for size R has been calculated as follows:⁵²

$$N_e(R) = \frac{N_A}{\bar{V}} \exp\left[\frac{-\Delta G(R)}{R_g T}\right] \quad (2.11)$$

Where N_A is the Avogadro's number, \bar{V} is the molar volume of the precipitate and R_g is the gas constant.

The following equation explains the nucleation rate of a critical nuclei size to assemble an embryo to an additional atom:⁵²

$$J = \frac{dN(R_c)}{dt} = \frac{2D}{d^5} \exp\left(-\frac{G(R_c)}{R_g T}\right) \quad (2.12)$$

where D is the diffusion coefficient and d is the molecular diameter.

A relationship between the nucleation, the maximum nucleation and the supersaturation value is shown below:⁵²

$$\log\left(\frac{J}{J_{\max}}\right) = -A(\log S)^{-2} \quad (2.13)$$

where A is:

$$A = \frac{4(4\pi)^3 \gamma^3 \bar{V}^2 N_A}{27\left(\frac{4\pi}{3}\right)^2 \cdot (R_g T \ln 10)^3} \quad (2.14)$$

2.3.2 Particle formation and stability-Ostwald Ripening

This section is very important to understand and predict the stability of nanoparticle dispersions after they are formed. The rate of nucleation (J) and growth of the nuclei control the initial particle size. This rate of nucleation can be calculated as follows:²⁴

$$J \propto \exp\left[-\frac{16\pi\gamma_{sl}^3 V_M^2}{3K_B^3 T^3 (\ln S)^2}\right] \quad (2.15)$$

where γ_{sl} is the solid-liquid interfacial tension of the solute, V_M is molar volume of the solute, and S is the supersaturation ratio. The γ_{sl} can be calculated as follows:⁵³

$$\gamma_{sl} = 0.414K_B T (N_A / V_M)^{2/3} \ln \left(\frac{1}{V_M c^\infty} \right) \quad (2.16)$$

The stability of nanoparticles in solution depends on agglomerations (due to their high surface energy), secondary crystallization, and Ostwald ripening. In Ostwald ripening, particles with small particle size shrink because of the enhanced solubility from their high curvature, and large particles grow. This theory of ripening was derived from the Lifshitz, Slyozov, and Wagner (LSW) theory for growth of particles from precipitation at supersaturated conditions. This process can be explained using the Kelvin equation.^{24, 54}

For the case of a solute in a liquid slightly above its saturation concentration c_s , a similar nucleation procedure will occur. Changing the role of the vapor pressure p from the previous equation to the solute concentration c and p_0 for c_s , the resulting Kelvin equation will be:⁵¹

$$c(R) = C_\infty \exp \left(\frac{2\gamma M}{\rho R_g T R} \right) = C_\infty \exp \left(\frac{\alpha_1}{R} \right) \quad (2.17)$$

where C_∞ is the bulk solubility and α_1 is the capillary length calculated as follows:²⁴

$$\alpha_1 = \frac{2\gamma V_m}{R_g T} \quad (2.18)$$

where γ is the surface free energy solution-precipitate, V_m is the molar volume, M is the molecular weight with density ρ , R_g is the gas constant and T is temperature. The capillary length is a very important parameter because it is a length scale under which curvature-induced solubility is important.²⁴

Liu et al.²⁴ have studied the aging particle size of beta-carotene stabilized with Polystyrene-block-polyethylene oxide (PS-b-PEO) using Ostwald ripening in combination with a model from Hoang et al. and compared them with experimental results using DLS.

Using LSW theory, the number of molecules in nanoparticles (n) were calculated as follows:²⁴

$$\frac{dn}{dt} = 4\pi D \cdot C_\infty \alpha \left(\frac{R}{R_c} - 1 \right) \quad (2.19)$$

Where D is the diffusion coefficient of a solute molecule in solution and n is calculated as follows:

$$n = \frac{4/3\pi R^3}{V_m} \quad (2.20)$$

The number average radius is the critical radius that is updated for each time step j :²⁴

$$R_{c,j} = \sum_{i=1}^N \frac{R_{i,j}}{N} \quad (2.21)$$

Kumar et al.⁵⁴ calculated the growth velocity by diffusion as follows:⁵⁴

$$\frac{dR}{dt} \approx \frac{\gamma V_M^2 D c^\infty}{3 R_g T R^2} \quad (2.22)$$

Equation 2.40 is integrated and the diffusion time (t_d) can be calculated as follows:⁵⁴

$$t_d \approx \frac{R_g T R^3}{\gamma V_M^2 D c^\infty} \quad (2.23)$$

2.4 Continuous mixer techniques

A continuous mixer technique has been used to form narrow sizes nanoparticles of 50-150 nm for different biomedical applications. This technique provides a way to control particle size, composition, and surface chemistry of nanoparticles. The following sub-sections provide the theory and parameters in order to use the mixer. There are two types of mixers, one is the Confined Impinging Jet (CIJ) mixer and the other is the Multi-Inlet Vortex Mixer (MIVM).

2.4.1 CIJ Mixer

The confined impingement jet mixer was designed to operate at a mixing time less than the characteristic process time for fast precipitation processes.²⁵ Two important parameters are required: first, produce a region of high turbulent energy dissipation. High energy dissipation occurs for impinging jets because the kinetic energy of each jet stream is converted into a turbulent-like motion through a collision and redirection of the flow in a very small volume. Second, ensure that the process streams for mixing pass through the high intensity region without bypassing. The first criteria ensure the proper scale of mix and the second ensures that the desired molar flow ratios are preserved during the rapid mixing process.¹⁸

To calculate the mixing time, three scales of the mixing process in the mixing chamber are studied. The classification of the mixing of two miscible fluids by three scales can be explained as following (1) the fluids mix in the mixing chamber by convection energy (macro scale). (2) Formation of turbulent eddies occur in the mixing chamber (meso scale) and daughter vortices by turbulent diffusion occurred. (3) Molecular diffusion occurred in the turbulent eddies and eliminate region of segregations.¹⁸

The characteristic mixing time can be estimated using the theory of the diffusion across a length scale characteristic of the mixing energy input into the system. The time for diffusion can be approximated using half the slab thickness, due to a repeating boundary condition using the following equations:

$$\text{Diffusivity} = \frac{(0.5\lambda_k)^2}{\tau_{\text{diffusion}}} \quad (2.24)$$

and

$$\tau_{\text{mix}} = \tau_{\text{diffusion}} = \frac{(0.5\lambda_k)^2}{\tau_{\text{diffusivity}}} \quad (2.25)$$

The length scale for the slab is chosen to be the Kolmogorov length scale or the smallest eddy dimension which is able to form in turbulence prior to the domination of viscous effects and a laminar flow microstructure. We can use the momentum diffusivity or the kinematic viscosity ν in m^2/s . One assumption is making that mixing down to the Kolmogorov scale is not rated limiting and a “lamellar” structure can be created quickly relative to the diffusion time of the reagents of the system. The length scale can be expressed in terms of the energy dissipation rate ε in $\text{J/s}\cdot\text{kg}$, and the kinematic viscosity existing at the point of the mixing.¹⁸ The key assumption for the smallest eddies is that the properties are determined only by the local flow conditions. Their scales are assumed to depend on ε and the kinematic viscosity.⁵⁵ The Kolmogorov length scale for the smallest eddy dimension is shown in the following equation.

$$\lambda_k = \left[\frac{\text{diffusivity}^3}{\varepsilon} \right]^{1/4} \quad (2.26)$$

The energy dissipation rate is the rate of energy input into the system P [=] J/s , divided by the mass over which the energy is dissipated. The mass can be calculated using the density of

the effluent product times the meso-mixing volume of the mixer chamber (V_{mixer}). The energy dissipation rate is described as the following equation.

$$\varepsilon = \frac{P}{\rho_3 V_{\text{mixer}}} \quad (2.27)$$

The energy input to the system can be derived from the redirection of each stream's velocity into the perpendicular direction. The energy input to the system is calculated using the addition of the kinetic energy of the organic and anti-solvent streams where it can be expressed in terms of the mass flow rate and the velocity of the two incoming solvents as the following equation:

$$P = \frac{1}{2} m_1 u_1^2 + \frac{1}{2} m_2 u_2^2 \quad (2.28)$$

Then, we can substitute the equations 2.26-2.28 into equation 2.25 to obtain a final mixing time with fluids' physical constants and parameters. The following equations are the mixing time using for the two streams in the final product.

$$\tau_{\text{mix}} = \frac{v_3^{1/2} \rho_3^{1/2} V_m^{1/2}}{4 \left(\frac{1}{2} m_1 u_1^2 + \frac{1}{2} m_2 u_2^2 \right)^{1/2}} \quad (2.29)$$

To calculate the residence time (τ_{res}), a mass balance can be used in the mixing chamber.

The effluent flow rate (F_E) is the addition of the organic flow rate (F_1) and anti-solvent flow rate (F_2) as shown in the following equation:

$$F_1 + F_2 = F_E \quad (2.30)$$

Then the effluent flow rate can be related to the mixer volume (V_{mixer}) to calculate the residence time as shown in the following equation:

$$F_E = \frac{V_{\text{mixer}}}{t_{\text{mix}}} \quad (2.31)$$

$$\tau_{\text{res}} = \frac{V_{\text{mixer}}}{F_E}$$

2.4.2 MIVM

2.4.2.1 Theory

The MIVM is designed to produce multifunctional nanoparticles. The mixer has four inlets tangential to the boundary of the mixing chamber. The final product exits the mixing chamber at the center as shown in Figure 2.8.

The dimensions of the MIVM are shown in Table 2-7. The concept of the MIVM is that the momentum from each stream contributes separately to drive fast micromixing into the chamber. For that reason, different volumetric flow rates in each stream can be run and still obtain good mixing. One of the advantages of using the MIVM is that the final fluid phase is mostly anti-solvent. Therefore, the stability of the nanoparticles increases in solution by depressing the rate of Ostwald ripening. Also, by having different inlet streams, we can introduce different reactive compounds and therefore the reactive precipitations can be accomplished.¹⁹

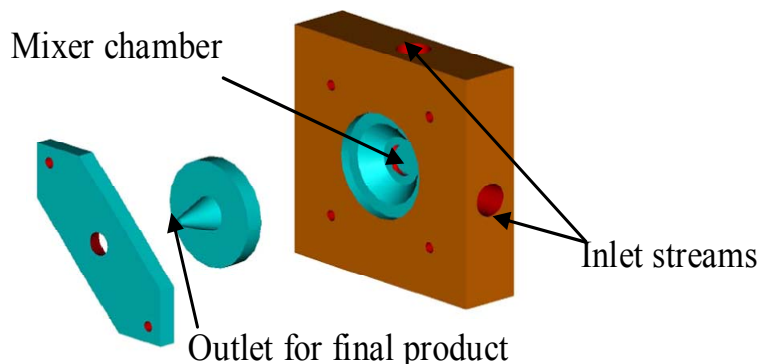


Figure 2.8. Schematic for the MIVM

Table 2-7. Different diameters for the MIVM

D_{mixer} (m)	0.0059
d_{is} (m)	0.0011
d_{os} (m)	0.0013

The importance of the vortex mixer is that a turbulent region can be created to provide a mixing environment to create and precipitate homogeneous nanoparticles. The turbulent region is created by the momentum of the inlet streams.

2.5 Flash Nanoprecipitation of organics

This section is important to understand the jet mixer and MIVM processes using a micromixing scale. The aim of flash nanoprecipitation is to produce nanoparticles which require fast mixing of two or more streams to create supersaturation. Flash nanoprecipitation process is described in Figure 2.9. This figure shows the precipitation of beta-Carotene stabilized with an amphiphilic polymer. This process requires several key components. The first key component is a rapid mixing time (τ_{mix} in milliseconds) of the materials shorter than the formation of nanoparticles (τ_{flash}). In other words, the mixing time must be less than induction time of the self assembly of the amphiphilic polymer and less than the induction time of nucleation and growth (τ_{ng}) of the organic material. These induction times can be tuned using different molecular weights of the polymer and by changing the concentration of the active concentration. When these two induction times are appropriately matched, the hydrophobic part of the amphiphilic polymer is attached on the surface of the growing organic particle. The hydrophilic portion of the amphiphilic polymer will provide the steric stabilization of particles in solution.²⁶

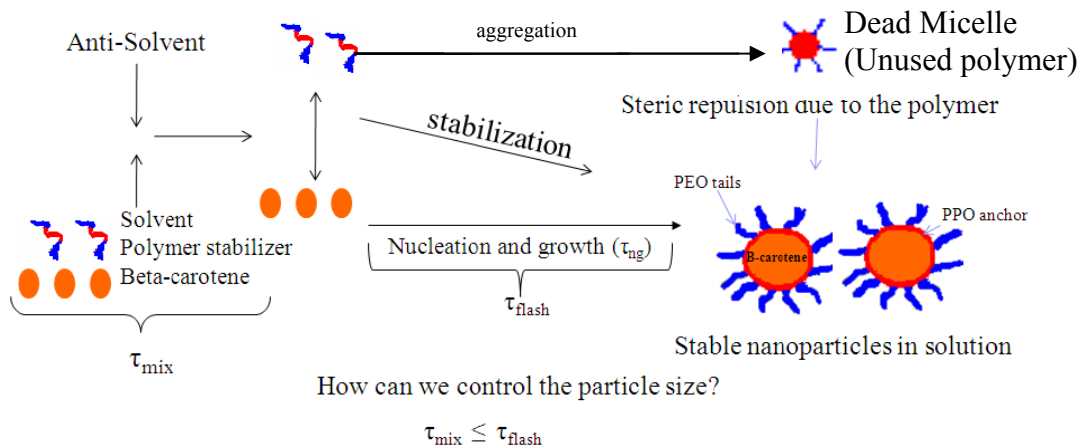


Figure 2.9. Flash NanoPrecipitation for Beta-Carotene modified from B. K. Johnson³⁰

2.6 Dynamic Light Scattering (DLS)

Particles suspended in a liquid are never stationary. Because of Brownian motion, particles are always moving due to the random collision between molecules of the liquid surrounding the particles. Small particles move quickly and large particles move more slowly.⁵⁶

Dynamic Light Scattering (DLS) is a light scattering method based on the time dependence of the scattered light intensity from the particles. Particles in suspension are illuminated with a laser and a sensitive photodetector monitors the scattered light. The scattering intensity varies with time (t) since the scattering centers are in a constant random motion due to their kinetic energy. This time-dependent intensity contains information on the random motion of the particles and thus can be used to measure the diffusion coefficient (D) of the particles which, in turn, provides information on the particle size distribution in colloidal dispersions.⁵⁷

2.6.1 Scattering intensity fluctuations

When small particles are illuminated by a laser, the particle will scatter light in all directions. When a screen is held close to the particle, the screen is illuminated by the scattered light. This speckle pattern consists of areas of bright light and dark areas (where no light is detected).⁵⁶

DLS measures the fluctuation in scattering intensity (I) using a correlator which measures the degree of similarity or the autocorrelation function $G(\tau)$ between two signals from some initial time t_0 out to a long delay time τ as shown in the following equations:^{56, 58} The time dependence of $G(\tau)$ can be described by various models. For the cumulants model, $G(\tau)$ is given by:

$$G(\tau) = \frac{I(t_0)I(t_0 + \tau)}{I(t_\infty)^2} = B + A \exp(-2q^2 D\tau) \quad (2.32)$$

This equation assumes a single exponential decay (i.e. one particle size). It gives only the z-average size and polydispersity index. Also, it is recommended by the International Standard Association.⁵⁸

For the multimodal model, $G(\tau)$ is given by:

$$G(\tau) = \frac{I(t_0)I(t_0 + \tau)}{I(t_\infty)^2} = B + \sum A \exp(-2q^2 D\tau) \quad (2.33)$$

where B is a coefficient related to the baseline of the autocorrelation function, A is the amplitude from the correlation function, and q is the scattering vector. The number of exponential functions is varied to obtain an optimal fit for $G(\tau)$.⁵⁸ This equation is used for various algorithms to calculate the diffusion coefficient D such as CONTIN, regularization, and Non-Linear Least

Squares. Using previous equations and the Nernst-Einstein equation, D can be calculated as follows:⁵⁷

$$D = \frac{kT}{\zeta} \quad (2.34)$$

This equation includes the calculation for a constant velocity (v) for a particle within a viscous medium. This requires a constant force ($F = v\zeta$), where ζ is the friction coefficient of the particles. For a spherical system $\zeta = 6\pi\eta R_H$. Using the previous equation, Nernst-Einstein equation reduces to Stokes-Einstein equation as follows:^{49, 57}

$$D = \frac{kT}{6\pi\eta R_H} \quad (2.35)$$

where η is the solvent viscosity and R_H is the hydrodynamic radius of the particles.

2.6.2 Rayleigh equation

Rayleigh scattering theory applies only when the scattering centers are small in dimension compared to the wavelength of the radiation used in the measurement experiments, i.e. when (particle diameter/laser wavelength) < 1/10. Also, it applies to non-absorbing and spherical particles in a gaseous medium.⁴⁹ The Rayleigh scattering equation was derived by Lord Rayleigh in 1871 and is:⁵⁷

$$\frac{i_s}{I_{0,u}} = \frac{2\pi^2 M}{r^2 \lambda_0^4 N_A \rho} (n-1)^2 (1 + \cos^2 \theta_x) = R_\theta (1 + \cos^2 \theta_x) \quad (2.36)$$

where i_s is the intensity, as measured at r and θ_x as shown in Figure 2.10 of the light scattered per unit volume by a gas of molecular weight (M), density (ρ), refractive index (n), and λ_0 is the wavelength in vacuum. Finally $I_{0,u}$ is the incident light unpolarized (subscript u). The term $R_\theta(1 + \cos^2\theta_x)$ is known as the Rayleigh ratio, $(1 + \cos^2\theta_x)$ is the scattered light's vertically polarized component, and $\cos^2\theta_x$ is the horizontally polarized component.⁴⁹

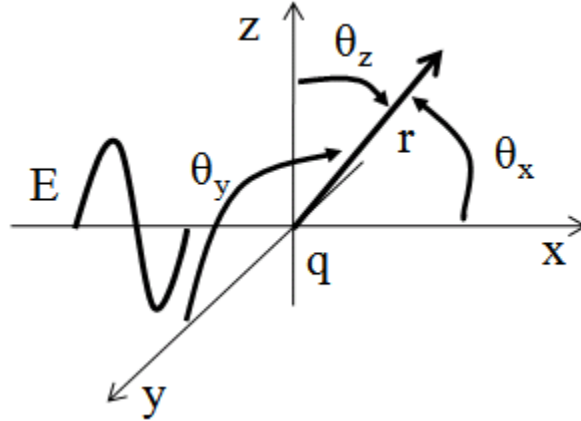


Figure 2.10. Electric field coordinates relative to the oscillating charge modified from P. Hiemenz⁵⁷

This theory does not apply when the scattering molecules are strongly absorbing. A modified Rayleigh equation that applies to solutions can be defined as follows:⁵⁷

$$\frac{i_s}{I_{0,u}} = \frac{\pi^2 (\overline{\delta p})^2}{2 \epsilon_0^2 r^2 \lambda^4} (n-1)^2 (1 + \cos^2 \theta_x) \quad (2.37)$$

where λ is the wavelength of light in the medium, p is the polarizability, and ϵ_0 is the permittivity in vacuum.

2.6.3 Mie scattering

Mie (1908) theory applies when particles are reasonably large, i.e. (particle diameter/laser wavelength) $> 1/10$. Mie theory models the scattering and adsorption of cross sections using power series that involve the size parameter β , defined as:⁵⁷

$$\beta = 2\pi \frac{R}{\lambda} \quad (2.38)$$

where R is the particle's radius.

This theory applies for particles within dimension less than the wavelength of light and to absorbing and non-absorbing particles. Mie developed expansion equations for absorbance and scattering efficiency factors such as χ_{abs} and χ_{sca} and are defined as follows:⁵⁷

$$\chi_{abs} = A_1 \beta + A_2 \beta^3 + A_3 \beta^4 \quad (2.39)$$

and

$$\chi_{sca} = A_4 \beta \quad (2.40)$$

Values of A_i are listed in Table 2-8.

Table 2-8. Constant values for A_1 - A_4 modified from P. Hiemenz⁵⁷

Coefficient	General case	When k=0
A1	$\frac{24nk}{(n^2 + k^2)^2 + 4(n^2 - k^2) + 4}$	0
A2	$\frac{4nk}{15} \frac{20nk}{3[(4n^2 + k^2)^2 + 12(n^2 - k^2) + 9]}$ $+ \frac{4.8nk [7(n^2 + k^2)^2 + 4(n^2 - k^2 - 5)]^2}{[(n^2 + k^2)^2 + 4(n^2 - k^2) + 4]^2}$	0
A3	$\frac{-192n^2k^2}{[(n^2 + k^2)^2 + 4(n^2 - k^2) + 4]^2}$	0
A4	$\frac{\frac{8}{3}[(n^2 + k^2)^2 + n^2 - k^2 - 2]^2 + 36n^2k^2}{[(n^2 + k^2)^2 + 4(n^2 - k^2) + 4]^2}$	$\frac{\frac{8}{3}(n^2 - 1)^2}{(n^2 + 2)^2}$

In Table 2-8, n is the refractive index and k is included in the refractive index using an absorbing material as a complex number $(n-ik)$ where $i=(-1)^{0.5}$. For non-absorbing complexes, k is zero, and n and k depend on the wavelength of the characteristics of the material.⁵⁷

3 Design and Characterization of the Multi Inlet Vortex Mixer to form uniform nanoparticles

R. Mejia-Ariza¹, O. Celebi¹, W. C. Miles², J. S. Riffle^{1, 3}, R. M. Davis^{1, 2}

¹Macromolecules and Interfaces Institute, ²Department of Chemical Engineering, ³Department of Chemistry, Virginia Polytechnic Institute and State University, Blacksburg, VA 24061

This chapter has not submitted for peer-reviewed publication

Mr. Oguzhan Celebi at Virginia tech synthesized the magnetite coated with oleic acid and oleyl amine.

3.1 Abstract

Control of nanoparticle size distribution is very important in biological systems for cellular uptake and targeted delivery. A Multi-Inlet Vortex Mixer (MIVM) is a continuous precipitation process that yields particles with relatively narrow and controlled size distributions. In the MIVM, four liquid streams collide under turbulent conditions in a mixing chamber where particle nucleation and precipitation occur within milliseconds. The MIVM is developed to form, control, and design nanomaterials. Using the MIVM, molecules nucleate and grow forming nanoparticles stabilized by self assembly of polymers into the nanoparticles surface. The formation of β -carotene nanoparticles and oleic acid and oleylamine coated magnetite clusters encapsulated with a diblock polyethyleneoxide-b-propyleneoxide was used to characterize a MIVM. The precipitation of molecules and the formation of oleic acid and oleylamine coated magnetite clusters were studied in the presence of an amphiphilic block copolymer containing poly (ethylene oxide) to provide steric stabilization and control of size distributions. After the nanoparticles were formed, they were dialyzed to remove the organic solvent and the unimer chains and were then characterized by dynamic light scattering, electron microscopy, and thermal gravimetric analysis. Nanoparticles were formed with intensity-weighted diameters in

the range 70-200 nm. The compositions of the magnetite varied between 0.13-0.36 weight fraction.

Keywords: Multi-inlet vortex mixer (MIVM), self assembly, β -carotene nanoparticles, clusters, oleic acid and oleylamine coated magnetite nanoparticles

3.2 Introduction

A continuous mixer technique has been used to form narrow size distribution of nanoparticles for different biomedical applications.^{18, 19, 58-62} This technique provides a way to control particle size, composition, and surface chemistry of nanoparticles. The MIVM is designed to produce multifunctional nanoparticles. The mixer has four inlets tangential to the boundary of the mixing chamber. The final product exits the mixing chamber at the center as shown in Figure 3.1.

The dimensions of the MIVM are shown in Table 3-1. The concept of the MIVM is that the momentum from each stream contributes separately to drive fast micromixing into the chamber. For that reason, different volumetric flow rates in each stream can be run and still obtain good mixing. One of the advantages of using the MIVM is that the final fluid phase is mostly anti-solvent. Therefore, the stability of the nanoparticles increases in solution by depressing the rate of Ostwald ripening when the solubility of the precipitating species is high enough to permit this process. Also, by having different inlet streams, we can introduce different reactive compounds and therefore the reactive precipitations can be accomplished.¹⁹

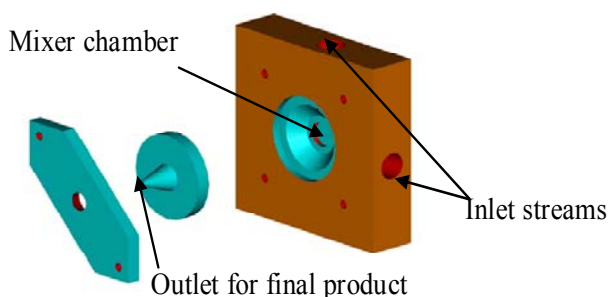


Figure 3.1. Schematic for the MIVM

Table 3-1. Specifications for the MIVM

D_{mixer} (m)	0.0059
d_{is} (m)	0.0011
d_{os} (m)	0.0013

The importance of the vortex mixer is that a turbulent region can be created to form and precipitate homogeneous nanoparticles. The turbulent region is created by the momentum of the four inlet streams through the mixing chamber. The mixing of the four miscible fluids can be explained as following (1) the fluids mix in the mixing chamber by convection energy (macro scale). (2) Formation of turbulent eddies occur in the mixing chamber (meso scale) and daughter vortices by turbulent diffusion occurred. (3) Molecular diffusion occurred in the turbulent eddies and eliminate region of segregations.¹⁸

The parameters used in the MIVM are Reynolds numbers, inlet velocities, and physical properties of the inlet streams. The inlet velocities depend on the desired Reynolds numbers and volume fractions in the mixing chamber. The four inlet flow rates can be controlled using mechanical pumps. The Reynolds number (Re) depends upon the inlet stream velocities (u_i) and kinematic viscosities (ν_i) of the inlet streams and is defined by¹⁹:

$$\text{Re} = D_{\text{Mixer}} \left(\frac{u_1}{\nu_1} + \frac{u_2}{\nu_2} + \frac{u_3}{\nu_3} + \frac{u_4}{\nu_4} \right) \quad (3.1)$$

where D_{Mixer} is the diameter of the mixer

The mass flow rate for stream “i” (m_i) is defined by:

$$m_i = Q_i \cdot \rho_i \quad (3.2)$$

where Q_i is the flow rate and ρ_i is the density of the “ith” inlet stream.

The flow rate is defined by:

$$Q_i = u_i A_{\text{is}} \quad (3.3)$$

where the area of the inlet stream (A_{is}) is:

$$A_{\text{is}} = \frac{\pi}{4} d_{\text{is}}^2 \quad (3.4)$$

where d_{is} is the diameter of the inlet streams.

The volume of fluid injected in the “ith” inlet stream (V_{is}) is defined by:

$$V_{is} = Q_i \cdot t \quad (3.5)$$

where t is the duration time of each experiment.

The mixer chamber is a flat cylinder with volume V_{Mixer} and is defined as:

$$V_{Mixer} = h_{Mixer} \cdot A_{Mixer} \quad (3.6)$$

where h_{Mixer} and A_{Mixer} are the height and area of the mixing chamber, respectively.

The total volume fraction of the “ith” stream (ϕ_i) in the mixer can be written as the flow rate fraction ratio as follows:

$$\phi_i = \frac{Q_i}{\sum_{i=n} Q_i} = \frac{u_i A_{is}}{A_{is} \sum_{i=n} u_i} \quad (3.7)$$

Assuming that there is no volume change in the liquid phase upon mixing, the volume fraction can be written as a function of inlet velocities in the mixer as follows:

$$\phi_i = \frac{u_i}{u_1 + u_2 + u_3 + u_4} \quad (3.8)$$

For one inlet stream of organic active in THF (u_1) and three inlet streams of DI-water (u_2 , u_3 , and u_4) and assuming that $u_2=u_3=u_4$, the organic active stream velocity can be written as:

$$u_1 = \frac{3\phi_{THF}}{1 - \phi_{THF}} u_2 \quad (3.9)$$

Now we can substitute equation 3.9 onto equation 3.1 and solve for u_2 :

If $v_2=v_3=v_4$

$$Re = 3u_2 \left(\frac{\phi_{THF}}{1 - \phi_{THF}} \frac{1}{v_1} + \frac{1}{v_2} \right) \quad (3.10)$$

and

$$x = \left(\frac{\phi_{THF}}{1 - \phi_{THF}} \frac{1}{v_1} + \frac{1}{v_2} \right) \quad (3.11)$$

where x is a collection of parameters to make the mathematic easier for the next equations. Then, u_2 can be calculated as follows:

$$u_2 = \frac{Re}{3D_{Mixer} x} \quad (3.12)$$

In the organic streams, the mass of organic materials can be calculated using the weight fraction of material in THF (wf_i) as follows:

For the mass of organic material (m_i):

$$wf_i = \frac{m_i}{m_i + m_{THF}} \Rightarrow m_i = \frac{wf_i}{1 - wf_i} \cdot m_{THF} \quad (3.13)$$

where m_{THF} is the mass of THF

The concentrations of organic materials (C_i) in the mixer are calculated as follows:

$$C_f = \frac{m_i}{V_T} = \frac{m_i}{\sum V_i} \quad (3.14)$$

The supersaturation value (S) of the organic materials can be calculated as follows:

$$S = \frac{C_f}{C_{cwc}} \quad (3.15)$$

where C_{cwc} is the critical water concentration of the inlet materials (i.e. β -carotene and oleic acid and oleylamine coated magnetite). The critical water concentration is the concentration of the material in a mixture of THF and water volumes where the precipitation of β -carotene and cluster formation begins.

The residence time (τ_{res}) can be calculated as follows:

$$\tau_{res} = \frac{V_{Mixer}}{\sum Q_i} \quad (3.16)$$

3.2.1 Flash Nanoprecipitation of organics

Flash Nanoprecipitation produces nanoparticles which require fast mixing of two or more streams to create supersaturation, typically on a time scale of milliseconds. Figure 3.2 shows the precipitation of β -carotene stabilized with an amphiphilic polymer. This process requires several key components. The first key component is a rapid mixing time (τ_{mix} in milliseconds) of the materials shorter than the formation of nanoparticles (τ_{flash}). In other words, the mixing time must be less than the induction time of the self assembly of the amphiphilic polymer and less than the induction time of nucleation and growth (τ_{ng}) of the organic material. When these two induction times are appropriately matched to one another, the hydrophobic part of the amphiphilic polymer

attaches to the surface of the growing organic particle to arrest the growth of the particles. The hydrophilic portion of the amphiphilic polymer will provide the steric stabilization of particles in solution.²⁶

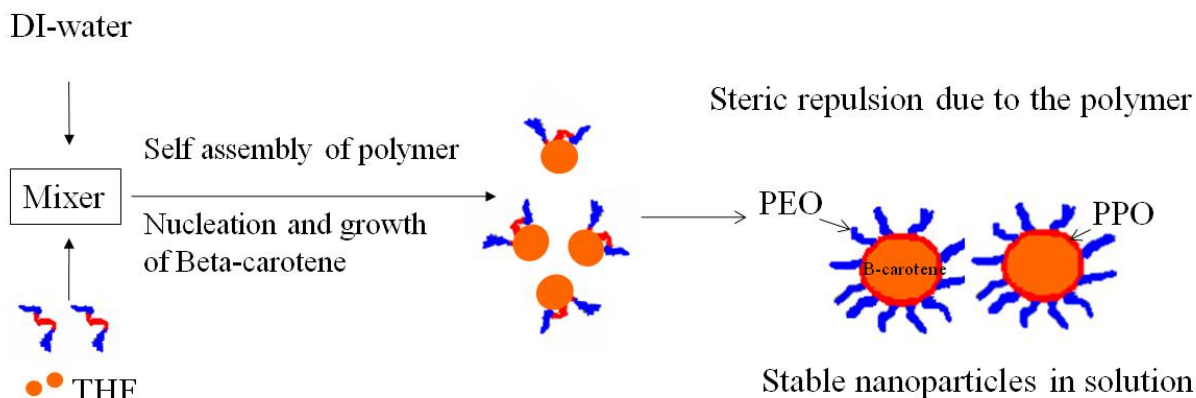


Figure 3.2. Flash NanoPrecipitation for Beta-Carotene modified from B. K. Johnson³⁰

To produce kinetically frozen nanoparticles, there are several requirements: (1) the supersaturation value should be higher than 10^2 ; (2) the copolymer should contain a hydrophilic block with sufficient length for steric or electrostatic repulsion. (3) The block copolymer should be soluble at the initial concentration and have a low Critical Micelle concentration (C_{cmc}), $C_{cmc} \leq 10^{-9}$ wt% (for Pluronic[®] F127) in the final conditions. Consecutively, the free energy to expel a chain from the nanoparticle's core should be higher than $5kT$ at the final conditions. This is very important to limit the exchange between unimers and micelles that leads to dynamic equilibrium.

This chapter concerns the testing of a newly constructed multi-inlet vortex mixer built according to the specifications of Figure 3.1. We first describe a series of experiments to form nanoparticles of β -carotene to compare the mixer's performance with a previous study.⁵⁹ This is followed by experiments to make clusters of oleic acid and oleylamine coated magnetite nanoparticles as part of a larger research project to make clusters as model materials for contrast agents in magnetic resonance imaging.

3.3 Materials and Methods

3.3.1 Materials

Tetrahydrofuran (THF) was purchased from EMD Chemicals and used without further purification. The β -carotene was purchased from Sigma-Aldrich (MW = 536.87 g/mol, Type I,

synthetic, $\geq 93\%$) and used without further purification. Pluronic[®] F127 was purchased from Fisher (MW = 4,300 PEO-4,000 PPO-4,300 PEO g/mol) and used without further purification. Water purified by reverse osmosis and passed through the NanoPure ion exchange system (18 M Ω -cm) was used for β -carotene nanoparticles, oleic acid and oleylamine coated magnetite cluster formation, dialysis, and size analysis. Oleic acid (90%), dibenzyl ether (99%), Iron(III) acetylacetonate (99.9%), and 1,2-hexadecanediol (90%) were purchased from Aldrich and used as received. Oleylamine ($\geq 70\%$, Fluka), hexane (Fisher Scientific, HPLC grade), and ethanol (Decon Labs, Inc.) were used without further purification.

3.3.2 Synthesis of Fe₃O₄ nanoparticles coated with oleic acid and oleylamine

Magnetite nanoparticles with diameter ~ 9 nm were synthesized using an adapted seed-mediated growth procedure.⁶⁰ Initially, 6 nm seed nanoparticles were synthesized as follows. Fe(acac)₃ (2.119 g, 6 mmol) was added to a mixture of dibenzyl ether (30 mL) and oleylamine (30 mL) in a 250-mL, three-neck, round-bottom flask. The reaction mixture was heated to 110 °C and sparged with nitrogen gas for 1 hour. The solution was then quickly heated to 300 °C and maintained at this temperature for 2 hours. The resulting suspension was cooled to room temperature and ethanol (150 mL) was added to the mixture. The precipitated nanoparticles were collected using a magnet and the supernatant was decanted. The product was dispersed in hexane (80 mL) and any undispersed residue was removed by magnetic decantation. Next, 8 nm nanoparticles were synthesized using the 6 nm seed nanoparticles as follows. Fe(acac)₃ (1.4127 g, 4 mmol), 1,2-hexadecanediol (5.169g, 20 mmol), dibenzyl ether (40 mL), oleic acid (0.37 mL, 4 mmol) and oleylamine (1.32 mL, 4 mmol) were mixed in a 250-mL, three-neck, round-bottom flask. Then, the seed nanoparticles (58 mg) dispersed in hexane (7 mL) was added to the reaction mixture. In a nitrogen atmosphere, the reaction mixture was heated at 100 °C for 30 min to evaporate the hexane, and then the temperature was increased to 200 °C for 1 h. The mixture was further heated to reflux (300 °C) for 30 min. The resulting suspension was cooled to room temperature and the same isolation procedure was applied as described above for the seed nanoparticles.

3.3.3 Determination of critical concentrations of oleic acid and oleylamine coated magnetite and F127

Determining the water-THF ratio at which both the hydrophobic oleic acid and oleylamine coated magnetite particles form clusters and the amphiphilic triblock polymers micellize was essential to determine how to synthesize uniform and stable clusters. To determine the critical micelle concentration (C_{cmc}) of F127 and the critical water concentration (C_{cwc}) of oleic acid and oleylamine coated magnetite, solutions of F127 and suspensions of oleic acid and oleylamine coated magnetite in THF were titrated with water. A Malvern NanoZS instrument was used to measure the scattering intensity, in terms of the count rate kilocounts/sec, of each sample as water was added incrementally. Samples were examined at $25 \pm 0.1^\circ\text{C}$ using a constant measurement placement of 4.65 mm and an attenuator setting of 9 (for F127 only) to ensure the incident light intensity was consistent. The count rate was monitored until a significant increase was noticed, which indicated the onset of aggregation. For oleic acid and oleylamine coated magnetite, the number diameter was measured by dynamic light scattering and reported as a function of water concentration. The number diameter was monitored until a significant increase was noticed, which indicated the onset of aggregation.

The supersaturation values of β -carotene ($S_{\beta\text{-carotene}}$) were calculated by:³⁰

$$S_{\beta\text{-carotene}} = \frac{C_f}{2.4(1.653 \exp(-0.0941 * wt\%_{\text{water}}))} \quad (3.17)$$

where C_f (mg/mL) is the concentration of β -carotene in the mixer and $wt\%_{\text{water}}$ is the water weight percent in the mixing chamber. The values of $S_{\beta\text{-carotene}}$ are shown in Figure 3.5.

3.3.4 Mixer Operation

The mixer has four inlets tangential to the boundary of the mixing chamber. The final product exits the mixing chamber at the center as shown in Figure 3.3.

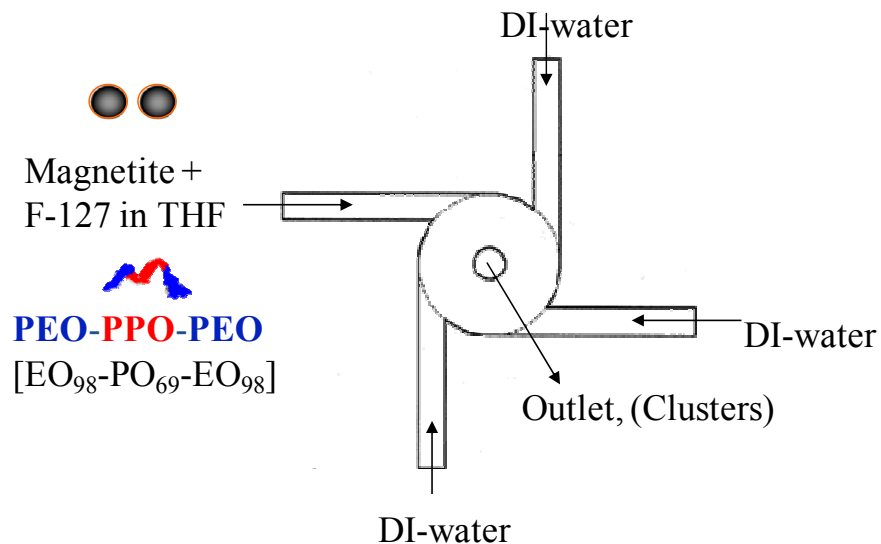


Figure 3.3. Schematic for the MIVM

Controlling the temperature was very important for controlling the solubilities of the organic materials which, in turn, affected the nucleation rate in the mixer. The temperature used in all oleic acid and oleylamine coated magnetite cluster experiments was controlled at $25 \pm 1^\circ\text{C}$ for oleic acid and oleylamine coated magnetite cluster formation and at $35 \pm 1^\circ\text{C}$ for β -carotene nanoparticles formation by passing the four inlet streams through stainless steel coils (OD: 1/8") submerged in a water bath (NESLAB RTE-100) that were connected to Teflon tubes (OD: 1/8") that feed into the mixer. For all β -carotene nanoparticle experiments and for oleic acid and oleylamine coated magnetite clusters formation at different supersaturation values, the organic stream was controlled by a KD Scientific 200 pump and the three water streams were controlled by a Harvard Apparatus Remote Infuse/Withdraw PHD 4000 Hpsi Programmable syringe pump. For oleic acid and oleylamine coated magnetite clusters formation at different Reynolds numbers, the organic stream and the three water streams were controlled by a Harvard Apparatus Remote Infuse/Withdraw PHD 4000 Hpsi Programmable syringe pump. Also, Labview 8.0™ was used to program and control the flow rates.

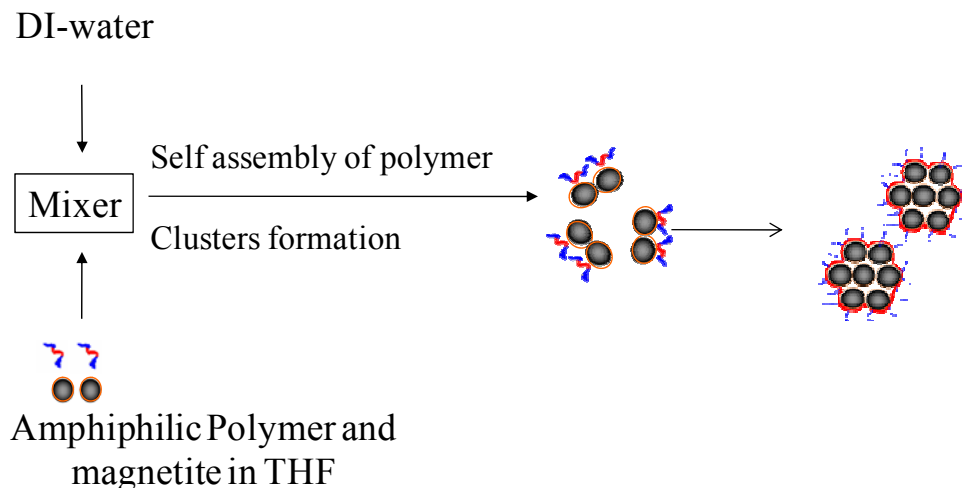


Figure 3.4. Flash Nanoprecipitation of clusters modified from Johnson, B. K³⁰

For the MIVM process the contents of four syringes were injected into a mixing chamber. One syringe held the “active organic” – the β -carotene or the dispersed oleic acid and oleylamine coated magnetite nanoparticles and the copolymer stabilizer suspended in the organic solvent, and other three syringes held the DI water. An amphiphilic copolymer was used to provide the steric repulsion and aid in the colloidal stability of these nanoparticles. The hydrophobic part of the polymer will attach to the surface of the oleic acid and oleylamine by hydrophobic interactions and the hydrophilic part will be in solution providing the steric repulsion between the nanoparticles. F127 was used in this study because is commercially available, biocompatible, biodegrade, and is a non-ionic macromolecular surface active agent. This important surfactant has been used in pharmaceutical applications such as drug solubilization and controlled release.⁶¹ Flow rates of the inlet streams were calculated using Reynolds numbers. The Reynolds number is defined as follows:¹⁹

$$\text{Re} = D_{\text{mixer}} \sum \frac{u_i}{\nu_i} \quad (3.18)$$

where D_{mixer} is the mixer diameter, u_i is the velocity of each inlet stream, and ν_i is the kinematic viscosity of each solvent.

For the rest of this chapter, concentrations of the organic “actives” – β -carotene, hydrophobic oleic acid and oleylamine coated magnetite, and F127 – are specified in terms of their concentrations in the injected stream #1 before it is mixed with DI water, i.e. their concentrations in the syringe used for the injection. The compositions of the liquid phase in the

mixer are expressed as volume % of water and THF after the 4 streams have mixed. This is the liquid phase composition of the effluent from the mixer.

Cluster formation was studied as a function of two variables: the Reynolds number which affects the mixing time τ_{mix} and the water (anti-solvent) composition in the mixer which affects supersaturation.

3.3.5 Preparation of β -carotene nanoparticles stabilized with F127

Pluronic F127[®] and dry β -carotene were dissolved in THF with a concentration of 19.58 mg/mL and 31.58 mg/mL for each material. The organic solution was fed at a fixed flow rate as shown in Table 3-2 (stream 1), along with DI-water at different flow rates (streams 2-4, see Table 3-2) into the MIVM to generate a final solvent composition of 90 volume percent of DI-water and 10 volume percent of THF in the mixer. The Reynolds number ranged between 50-5,000. The β -carotene nanoparticles were characterized after they were formed in the MIVM.

Table 3-2- Flow rates for organic and water solution in the mixer

Re	Q ₁ * (mL/min)	Q ₂₋₄ * (mL/min)
50	0.03	0.10
100	0.07	0.20
200	0.13	0.40
300	0.20	0.60
400	0.27	0.80
600	0.40	1.21
750	0.50	1.51
1000	0.67	2.01
2000	1.34	4.02
3000	2.01	6.03
4000	2.68	8.04
5000	3.35	10.0

* Calculated from equation 3.3

3.3.6 Preparation of oleic acid and oleylamine coated magnetite clusters stabilized with F127 as a function of Reynolds number

A solution of polyethylene oxide-b-poly propylene oxide-polyethylene oxide (PEO-PPO-

PEO) (Pluronic F127[®], 12,600 g/mol), and dry Fe₃O₄ nanoparticles coated with oleic acid and oleylamine were dispersed in THF with a concentration of 0.5 mg/mL for each material. The organic solution was fed at a fixed flow rate (stream 1), along with DI-water at different flow rates (streams 2-4) into the MIVM to generate a final solvent composition in the mixer of 75 volume percent DI-water and 25 volume percent THF. The Reynolds number ranged from 50 to 30,000.

After the clusters were formed, they were dialyzed for 12 hours using a Slide-A-Lyzer[®] Dialysis process (20,000 MWCO) (Cassette G2) with 3 changes of DI-water. The volume of DI-water was about 10 times the sample volume for each change of DI-water. The samples were freeze-dried with a vacuum of 3 mBar at -50 °C for 72 h. Then, thermogravimetric analysis (TGA) was performed to measure the experimental compositions.

3.3.7 Magnetite cluster formation at different supersaturation values

A solution of PEO-PPO-PEO (Pluronic F127[®], 12,600 g/mol), and dry Fe₃O₄ nanoparticles coated with oleic acid and oleylamine were dispersed in THF with a concentration of 0.5 mg/mL for each material. The organic solution was fed at a fixed flow rate (stream 1), along with DI-water at different flow rates (streams 2-4) to obtain a Reynolds number of 15,500 and at three different liquid phase compositions in the mixer and the effluent: 75, 83, and 90 volume% water. The clusters were then dialyzed for twenty-four hours using Spectra/Por membrane tubing (25,000 MWCO) (6 Spectra / Por[®] dialysis) with 5 changes of DI-water. The volume of DI-water was about 10 times of the sample volume for each change of DI-water. Finally, the samples were freeze-dried as described above. Thermogravimetric analysis was also performed to measure the experimental compositions.

3.3.8 Characterization of Clusters

The hydrodynamic sizes and polydispersity indices (PDI) of the oleic acid and oleylamine coated magnetite nanoparticles and clusters were characterized by dynamic light scattering at 25 ± 0.1 °C using the Zetasizer Nano ZS. The autocorrelation functions of the scattered intensity were fitted using cumulants analysis to extract the average translational diffusion coefficient and the hydrodynamic diameters were determined through the Stokes-

Einstein relation.⁶² Typically, samples were diluted in de-ionized water to ~ 0.01 - 0.02 mg/mL, sonicated using a water bath sonicator (Model 8890, Cole-Parmer, Chicago, IL) for 10 minutes and passed through a $1.0 \mu\text{m}$ PTFE syringe filter before measurements. The intensity-average diameter (D_I), volume-average diameter (D_V), number-average diameter (D_N), and polydispersity index (PDI) were recorded for each sample and averaged from three measurements.

The number-average (D_N) and volume-average (D_V) diameters of the nanoparticle clusters in aqueous suspensions were also measured by nanoparticle tracking analysis (NTA) using a NanoSight NS500-HSBF (NanoSight, Amesbury, U.K.). The instrument was equipped with a sample chamber illuminated by a 405 nm laser source operating at 75 mW and a 20X microscope objective collected the scattered light on an EMCCD camera (Andor SOLIS).⁶³ The nanoparticle clusters were directly visualized as point-scatterers moving under Brownian motion and videos were recorded at 30 frames per second. Each sample was measured for 180 s with manual shutter and gain settings. The camera settings used in this technique were a gain of 10, a blur size of 3×3 , an auto detection threshold and a minimal track length of 10 steps. The NTA 2.1 image analysis software was used to individually track the nanoparticle clusters on a frame-by-frame basis and generate number- and volume-average size distribution profiles. The sample preparation protocol was the same as that for DLS measurements except that the samples typically had to be diluted by a factor of 10-100 further for NTA analysis.

Transmission electron microscopy was performed with a Philips EM-420 field emission gun TEM at an acceleration voltage of 100 kV. The oleic acid and oleylamine coated magnetite nanoparticles and the nanoparticle clusters were deposited onto amorphous carbon-coated copper grids from dilute solutions (~ 0.02 mg/mL) of THF and de-ionized water respectively. Images were acquired at a magnification of 96,000X, corresponding to a resolution of $3.88 \text{ pixels nm}^{-1}$. For the oleic acid-coated nanoparticles, particle distribution analysis was performed using Reindeer Graphics' Fovea Pro 4 plug-in for Adobe Photoshop 7.0.

Thermogravimetric analysis (TGA) was used to determine the weight fraction of magnetite in the oleic acid-oleylamine-coated nanoparticles and the copolymer-stabilized nanoparticle clusters. Measurements were performed on a TA Instruments Q500 TGA under a constant flow of nitrogen of 30 mL min^{-1} . Samples were held at 115°C for 15 minutes to drive off any moisture and ramped at $10^\circ\text{C min}^{-1}$ up to a maximum of 650°C . The mass remaining at the end of the experiment was used to calculate the magnetite weight percentages in the clusters.

The typical masses used for TGA experiments were from 2-10 mg with 2-3 replicates. The polymer and oleic acid compositions in the clusters were calculated as follows:

$$x_{F127,final} = 1 - x_{mag,final} \left(1 + \frac{x_{OA,initial}}{x_{mag,initial}} \right) \quad (3.19)$$

$$x_{OA,final} = 1 - x_{mag,final} - x_{F127,final} \quad (3.20)$$

where $x_{F127,final}$ is the polymer mass fraction, $x_{OA,initial}$ and $x_{mag,initial}$ are the mass fractions of oleic acid-oleylamine and magnetite in the individual magnetite nanoparticles, and $x_{OA,final}$ is the oleic acid-oleylamine mass fraction in the clusters.

The number of polymer chains per nm^2 (ξ) in the magnetite clusters was calculated as follows.⁶⁴

$$\xi = \frac{\left(\frac{x_{F127,final} N_A \rho_{cluster}}{M_n x_{mag,final}} \frac{4}{3} \pi R_N^3 \right)}{4 \pi R_N^2} \quad (3.21)$$

where $x_{mag,final}$ is the mass fraction of magnetite, respectively, N_A is Avogadro's number, $\rho_{cluster}$ is the density of magnetite clusters, R_N is the number average radius of clusters, and M_n is the number-average molecular weight of F127. The assumptions made in the above equation are (1) the clusters are spherical in suspension, (2) the PEO chain length in the attached layer on the surface of the clusters does not contribute significantly to the observed hydrodynamic diameter of the clusters (3) all of the F127 in the suspension was used to encapsulate the clusters.

3.4 Discussion of Results

3.4.1 Formation of β -carotene nanoparticles

The mixing time of the materials depends on the Reynolds number. For that reason, β -carotene nanoparticles at different Reynolds numbers were formed to study the mixing times of the β -carotene and F127 in the mixer and how they can affect nanoparticle formation. Diameters were measured after the formation of the β -carotene nanoparticles coated with F127 at different Reynolds numbers using DLS (without any dialysis procedure) as shown in Table 3-3. For sizes analysis, the nanoparticles were diluted with DI water with a dilution factor as shown in Table 3-3 and then filtered with a 220 nm PVDF filter before the sizes were measured by DLS. Sizes

of nanoparticles were measured three consecutive times using the same sample in the cuvette. From these data, an average size and standard deviation were calculated.

For DLS, the Nano ZS instrument used the cumulants analysis to calculate a mean value for the size and a width parameter for the PDI. The cumulants analysis fits a polynomial log of the correlation function (G) as follows:⁵⁶

$$\ln(G) = a + bt + ct^2 \quad (3.22)$$

where t is time, b is known as the second order cumulant or the z-average diffusion coefficient. Then PDI can be calculated as follows:

$$PDI = \frac{2c}{b^2} \quad (3.23)$$

The equation used to calculate the standard deviation is the following:

$$\sqrt{\frac{\sum (x - \bar{x})^2}{n-1}} \quad (3.24)$$

where x is each numerical value, \bar{x} is the sample mean average value, and n is the sample size.

The dilution factor (ℓ) used for the DLS experiments was calculated using the following equation:

$$\ell = \frac{v_{sample}}{v_{sample} + v_{DI-water}} \quad (3.25)$$

where v_{sample} is the volume of the sample after the nanoparticles were formed in the mixer and $v_{DI-water}$ is the volume of DI-water.

The viscosity and refractive index values used in the DLS experiments were from water. After diluting each sample for DLS as shown in Table 3-3, the water volume percent for each experiment was approximately 99.9 v% and 0.1 v% of THF.

Table 3-3. Intensity Diameter, Volume diameter, and PDI for Beta-carotene nanoparticles stabilized with F127 at 1:9 v/v after filtration with 220 nm PVDF membrane filter at T= 35°C in the mixer [The DLS experiment was done at 25°C]

Table 3A. 2.2:2.2 wt% β -carotene:stabilizer (F127) in THF streams with a $C_{\text{Beta-carotene-THF}} = 19.58 \text{ mg/mL}$, and super-saturation value =228.

Dilution factor	$C_{\text{Beta-carotene}}$ (mg/mL) for DLS	Re	Intensity diameter (nm)	PDI
1:125	0.016	50	163 ± 5.5	0.22
1:120		100	156 ± 1.0	0.23
		200	148 ± 1.0	0.26
		300	149 ± 1.0	0.26
		400	150 ± 5.6	0.28
		500	149 ± 1.0	0.27
		750	139 ± 9.6	0.31
		1,000	144 ± 5.5	0.28
		2,000	130 ± 2.5	0.35
		3,000	135 ± 8.4	0.36
		4,000	133 ± 9.5	0.38
		5,000	136 ± 9.0	0.38

Table 3B. 3.5: 3.5 wt% beta-carotene: stabilizer (F127) in THF streams with a $C_{\text{Beta-carotene-THF}} = 31.58 \text{ mg/mL}$ and Super-saturation value =429.

Dilution factor	$C_{\text{Beta-carotene}}$ (mg/mL) for DLS	Re	Intensity diameter (nm)	PDI
1:100	0.031	50	149 ± 4.5	0.19
1:167	0.019	100	147 ± 3.3	0.22
1:22	0.137	200	147 ± 7.2	0.24
1:33	0.093	300	153 ± 12	0.23
1:133	0.024	400	133 ± 10	0.32
1:133	0.024	500	140 ± 5.8	0.36
1:100	0.031	750	130 ± 6.6	0.31
1:133	0.024	1,000	131 ± 8.8	0.31
1:200	0.016	2,000	117 ± 7.9	0.39
1:167	0.019	3,000	119 ± 6.7	0.40
1:167	0.019	4,000	116 ± 8.7	0.42
1:200	0.016	5,000	120 ± 16	0.42

*Calculated from equation 3.25.

Figure 3.5 shows the intensity diameter D_I as a function of Reynolds number for two supersaturation values of 228 and 428. At $Re < 1,500$, D_I decreases with increasing Reynolds numbers and depends primarily on Reynolds numbers and only weakly on the supersaturation S . In this region, the mixing time is slower (larger) than the nucleation and growth and the micellization times. At $Re = 1,500$, a break point was observed where diameters were constant and mixing time was equal to the nucleation and growth time of β -Carotene and the micellization time for F127. At $Re > 1,500$, D_I was approximately constant and depended only upon supersaturation values. The intensity diameters decreased with increasing S because more nuclei were formed which grew to form a higher number concentration of smaller particles compared to the process at lower values of S where fewer nuclei were formed.

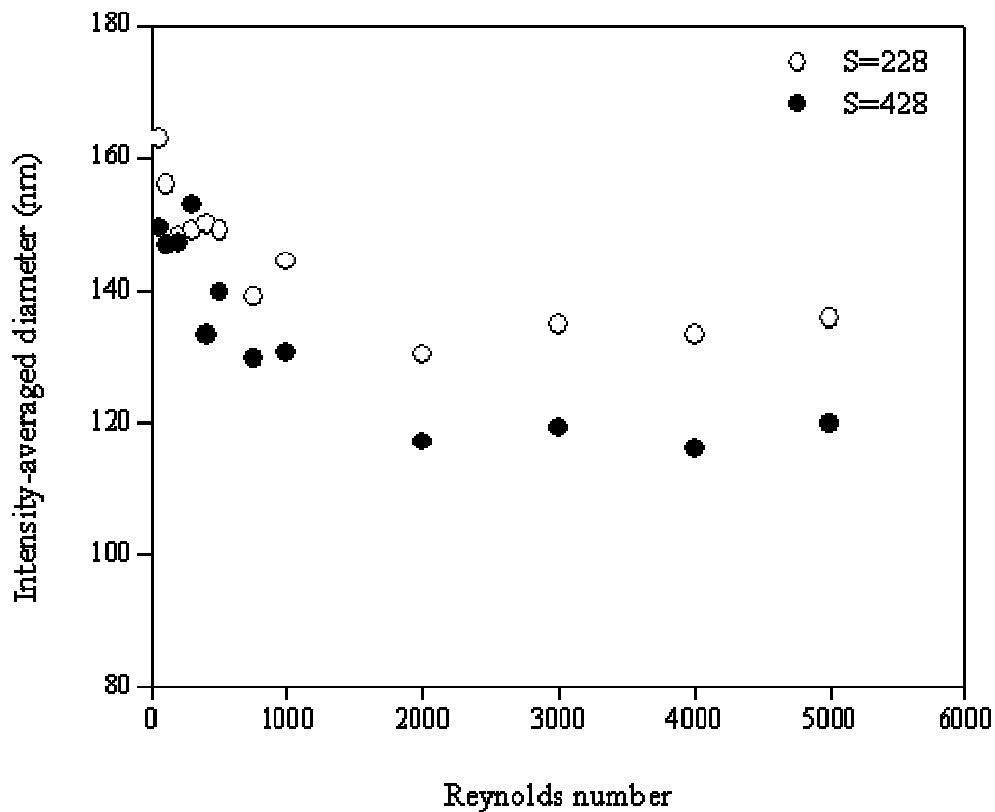


Figure 3.5. Intensity diameter for Beta-carotene nanoparticles at different Reynolds numbers for supersaturation values of 228 and 428, 1:9 v/v ratio in the mixer

3.4.2 Formation of magnetite clusters nanoparticles

Two different batches of magnetite coated with oleic acid and oleylamine were synthesized (using the same synthesis procedure) for the completion of this work. Batch 1 was used for magnetite cluster formation at different Reynolds numbers and batch 2 was used for magnetite cluster formation at different supersaturation values.

3.4.3 Characterization of individually magnetite nanoparticles coated with oleic acid and oleylamine

A TEM image of individual iron oxide nanoparticles is shown in Figure 3.6 and Figure 3.7. Image analysis was used to obtain a probability distribution of particle size for only the magnetite's core with a number-average diameter of 8.8 ± 1.3 nm for Batch 1 (as shown in Figure 3.6b) and 8 ± 3 nm for Batch 2, and magnetite and organic weight percentages of 75 and

25 for Batch 1 and 86 and 14 for Batch 2, as measured by TGA. Particles were dispersed in THF and their size was measured via DLS. The number diameter obtained for magnetite coated with oleic acid and oleylamine was 11-12 nm. This number is higher than 8-9 nm due to the oleic acid and oleylamine layers on the surface of the magnetite. The diameter results are summarized in Table 3-4. The magnetite was coated with oleic acid and oleylamine to avoid aggregation between the iron oxide cores. The nanoparticles are hydrophobic; this is important to form magnetite clusters when mixed with water.

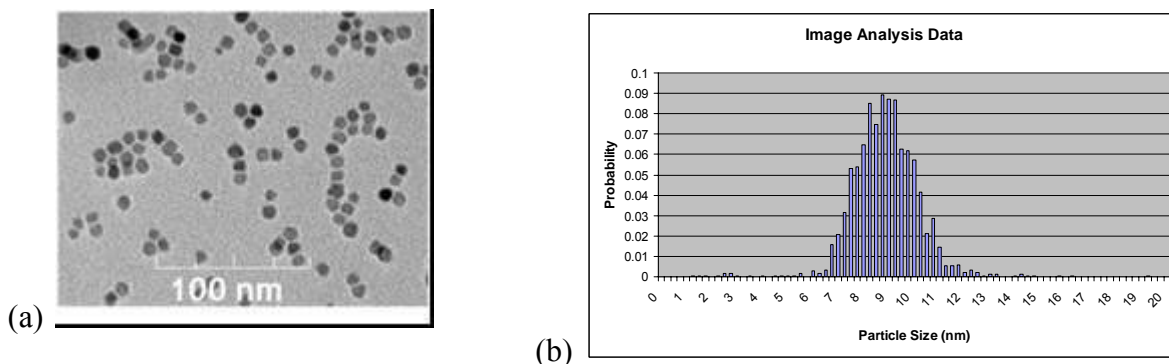


Figure 3.6. TEM image of individual magnetite nanoparticles and (b) particle size distribution from image analysis for Batch 1

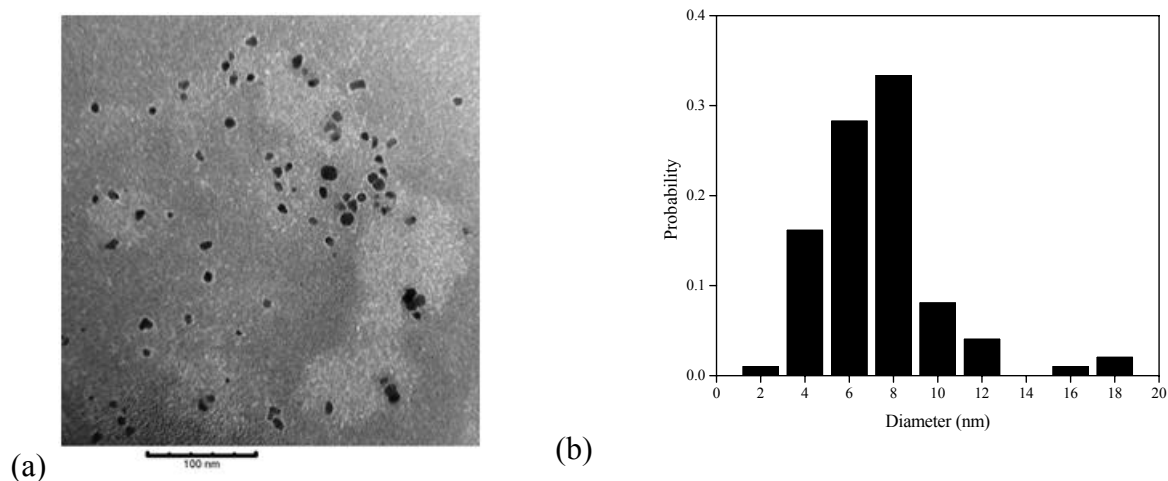


Figure 3.7. (a) TEM image of individual magnetite nanoparticles and (b) particle size distribution from image analysis for Batch 2

Table 3-4- Summary diameter results for individual magnetite nanoparticles

Sample name	Diameter by TEM (nm)	Number diameter by DLS (nm)
Batch 1	9±1	11
Batch 2	8±3	12

3.4.4 Critical Water Concentrations of F127 and oleic acid and oleylamine coated Magnetite

Figure 3.8 shows the critical micelle concentration of F127 at 25°C as a function of the volume% water in the liquid phase in the mixer. Also, it shows the critical water concentration for oleic acid and oleylamine coated magnetite at different concentrations and at 25°C. In the mixer, the concentrations of magnetite and F127 have to be highly supersaturated so that cluster formation and micellization occurs at similar time scales. Also, it shows the operating line which illustrates the flash nanoprecipitation process. This involves passing from point A (the organic injection) to Point D (the effluent from the mixer) in milliseconds. At point A, the oleic acid and oleylamine coated magnetite and F127 are soluble in THF. At point B, unprotected magnetite clusters start to form but the F127 polymer will not start to stabilize the magnetite clusters until the water concentration reaches point C where micellization of the polymer commences. By passing from point A to point D in milliseconds, it is possible to attain high supersaturation values of the magnetite nanoparticles which leads to controlled formation of the clusters where the F127 can be utilized to stabilize and encapsulate the magnetite clusters.²⁶ The following equations show the correlating equations developed for the critical water concentration (C_{cwc}) for oleic acid and oleylamine coated magnetite and the critical micelle concentration (C_{cmc}) for F127.

$$C_{cwc} = 0.425 \exp(-0.626 * v\%water) \quad (3.26)$$

and

$$C_{cmc} = 3685 \exp(-0.3696 * v\%water) \quad (3.27)$$

where $v\%_{water}$ is the volume percent of water.

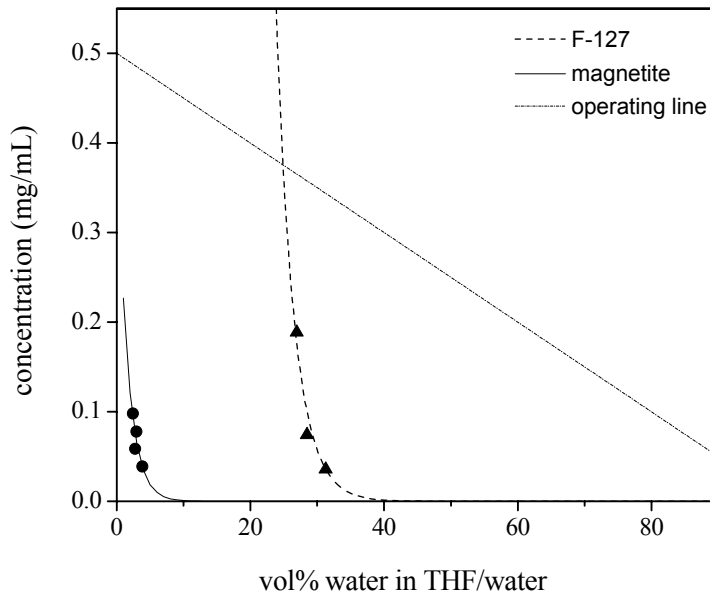


Figure 3.8. Critical micelle concentration of F127 and critical water concentration of oleic acid and oleylamine for forming clusters of magnetite at 25 °C

3.4.5 Effect of Reynolds number on Cluster Diameter

The mixing time of the streams depends on the Reynolds number. For that reason, clusters made with magnetite from Batch 1 were formed at different Reynolds numbers to learn how the mixing times of the magnetite and F127 affect cluster formation. The cluster diameters (measured before dialysis) were measured using DLS as shown in Figure 3.9. For size analysis, the effluent stream from the mixer was not dialyzed but was diluted with DI water. The samples from the effluent streams were diluted with a dilution factor of 1:5 (sample to DI-water) with a final volume composition of 95.8 v% of water and 4.2 v% of THF and without any filtration. The refractive index used in the volume and number calculations was 2.3 (refractive index value of magnetite⁶⁵). The intensity diameter does not depend on refractive index but the volume D_v and number average D_N do.

Figure 3.9 shows how the turbulence and mixing of the fluids affect the formation of magnetite cluster nanoparticles. At $Re < 8,000$, the D_t increased as the Re decreased suggesting that the mixing time τ_{mix} was larger than the time required for cluster formation and for copolymer self-assembly, τ_{cf} and τ_{sa} . At $Re > 8,000$, the diameters were approximately constant.

In this regime, $\tau_{\text{mix}} < \tau_{\text{cf}}$ and τ_{sa} so that the cluster diameter should depend primarily on the supersaturation values¹⁹.

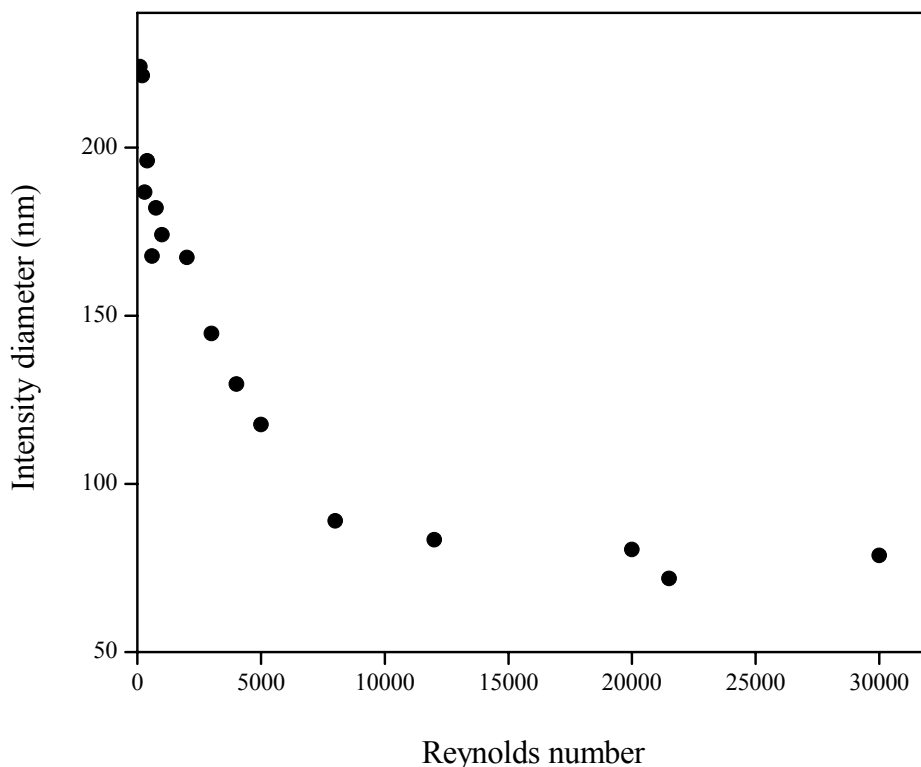


Figure 3.9. Intensity diameters of magnetite clusters measured using DLS. Cluster were made by injecting into the mixer a stream with magnetite and F127 concentrations = 0.5 mg/mL. The liquid phase composition in the mixer was 75 volume % water and 25 volume % THF.

3.4.6 Magnetite Cluster Composition

Magnetite clusters using oleic acid and oleylamine coated magnetite from Batch #1 were formed at $Re = 21,500$ in quantities of 10 mg so that their compositions and size stability could be measured using TGA and DLS, respectively. Compositions of particles were analyzed by TGA and are listed in Table 3-5. Table 3-5 summarizes the experimental weight percents of organic material and magnetite composition in the magnetite clusters at different Reynolds numbers. These numbers are essential to calculate how many chains are in 1 nm^2 of the surface of magnetite.

Table 3-5. Organic and magnetite composition in clusters using magnetite from batch #1 at Reynolds number = 21,500 with injected concentrations of 0.5 mg/ mL for magnetite and F127 and exit liquid phase concentration of 75 volume % water and 25 volume % THF (Calculated from equation 3.19 and 3.20).

Reynolds numbers	$x_{mag,final}$	$X_{OA,final}$	$x_{F127,final}$
21,500	0.36	0.12	0.52
NA*	0.37	0.13	0.50

***Theoretical composition of magnetite clusters when the magnetite and F127 polymer are injected in the MIVM at a wt/wt ratio of 1/1. The $x_{OA,final}$ and x_{F127} compositions were calculated using equations 19 and 20.**

The average chain density (ξ) on the cluster surface was estimated for magnetite clusters at Reynolds number of 21,500. Table 3-6 shows the experimental number of PEO chains per nm² of polymer on the surface of magnetite clusters made at Re = 21,500 and at 75 volume % water in the mixer. This is important to determine the effect of the polymer compositions and steric repulsion energies between nanoparticles for the stabilization of clusters in solution.

Table 3-6. Estimated PEO chain density on the surface of magnetite clusters described in Table 4.

Intensity diameter (nm)	Surface area (nm²)	# chains per cluster (f)	ξ^* chains / nm²
69	55 E+2	1.1 E+4	1.9

*Calculated from equation 3.21; the clusters were assumed to be spheres.

Before their sizes were measured by DLS as shown in Table 3-7, the clusters were dialyzed (Spectrum Laboratories™, MWCO 25,000) and then were diluted by a factor of 1:5 (nanoparticle solutions to water volume ratio).

Table 3-7. Intensity, Volume, and number diameters of magnetite clusters measured by DLS with initial concentrations of 0.5 mg/ mL for magnetite and F127. Liquid phase composition in mixer was 75 volume % water and 25 volume % THF and $Re = 21,500$. The refractive index used in the volume and number calculations was 2.3⁶⁵

Sample Name	Diameter (nm)			PDI
	Number	Volume	Intensity	
Run 1	45	53	69	0.21
Run 2	44	53	71	0.15
Standard Latex (Thermo Scientific®)			73	0.07

Dispersions of magnetite clusters were cast onto carbon grids and analyzed by TEM. representative TEM micrograph of clusters is shown in Figure 3.10. These images only show contrasts of magnetite because the amphiphilic polymer is unstained. In a given cluster, the separation of individual particles is clearly shown. Also, using these images, individual magnetite nanoparticles can be counted in the clusters. The average number of particles per cluster in Figure 3.10 is 23 ± 12 . In Figure 3.10, the clusters appearance at room temperature appears fluid-like in that appeared to wet and spread on the TEM grid, generating a 2D image.

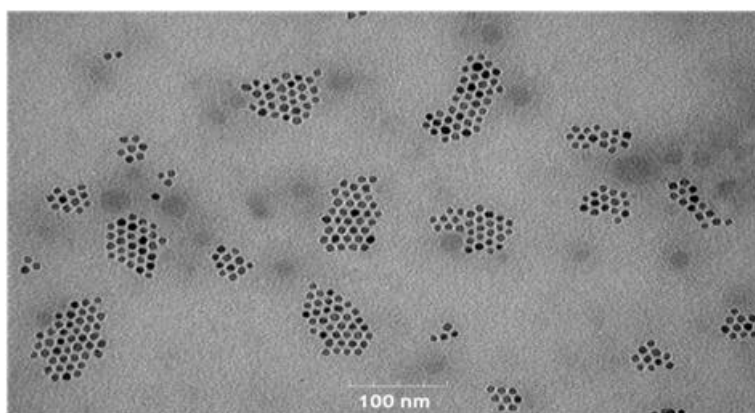


Figure 3.10. TEM image of magnetite clusters prepared with $Re=21,500$ and 75 wt% of water in the mixing chamber

3.4.7 Effect of supersaturation on magnetite cluster formation

The supersaturation of the magnetite nanoparticles, S_{mag} , is a very important parameter for controlling the distribution and size of the clusters and can be calculated from:²²

$$S = \frac{C_{mag-mix}}{C_{cwc}} \quad (3.28)$$

where $C_{mag-mix}$ is the concentration of magnetite in the mixer.

The nucleation rate, J , depends on the supersaturation values according to:²²

$$J \propto \exp \left[\frac{16\pi\gamma_{sl}^3 V_M^2}{3K_B^3 T^3 (\ln S)^2} \right] \quad (3.29)$$

where γ_{sl} is the solid-liquid interfacial tension of the solute, V_M is the molar volume of the solute, K_B is the Boltzmann constant, and T is the temperature (K).

Magnetite clusters were formed from magnetite synthesized in batch #2 at different mixer exit water volume compositions of 75, 83, and 90 and at a fixed Reynolds number of 15,500. The Reynolds number of 15,500 was chosen because this was the mixer operating regime where cluster size would mainly vary with S .

Table 3-8 and Table 3-9 show the sizes of magnetite clusters at different water volume percent in the mixer using DLS and NTA, respectively. After the clusters were formed and dialyzed (Spectrum Laboratories™, using a MWCO 25,000), they were diluted and then filtered with a 1µm PTFE filter. These results also show low polydispersity indexes with PDI values between 0.099 and 0.112 and good reproducibility in particle sizes. These results show that diameters of the clusters are independent of the water concentration between 75-90 volume percents. This may be due to the very high supersaturation ($\gg 1,000$) values in the mixer leading to a plateau region which suggests that supersaturation values do not have any more effect in the precipitation of magnetite clusters and polymer micellization.

Table 3-8. Intensity, Volume, and number diameters using DLS with injected concentrations of 0.5 mg/ mL for magnetite and F127 at Reynolds numbers = 15,500 and at different water volume % in the mixer effluent. The refractive index used in the volume and number calculations is 2.3 (magnetite refractive index value⁶⁵).

Water volume percent in the mixer	ℓ^*	Supersaturation value**	Diameter (nm)			PDI
			Number	Volume	Intensity	
75	1:5	7.2 E19	57 ± 1	71 ± 2	91 ± 2	0.09
83	1:1.5	8.8 E21	55 ± 1	71 ± 2	94 ± 5	0.11
90	1:1	3.5 E23	54 ± 1	70 ± 1	93 ± 1	0.11

*Calculated from equation 25, **calculated from equation 26

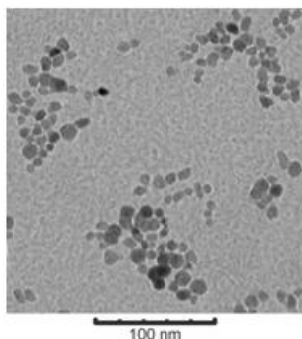
Table 3-9. Volume and number diameters using Nanosight with initial concentrations of 0.5 mg/ mL for magnetite and F127 at Reynolds numbers of 15,500 and at different water volume percents in the mixer

Water volume percent in the mixer	Supersaturation value	Concentration (E6 particles / mL)	Diameter (nm)	
			Number	Volume
75	7.2 E19	5.3	73	92
83	8.8 E21	4.1	74	90
90	3.5 E23	3.4	70	93

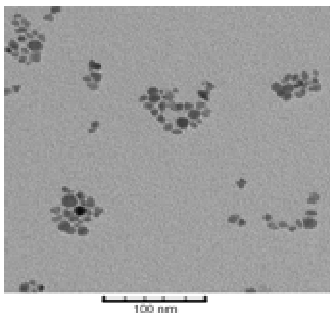
Dispersions of magnetite clusters were cast onto carbon grids and analyzed by TEM. Representative TEM micrographs of clusters are shown in Figure 3.11 at three different water volume percents.

Figure 3.11 only shows contrasts of magnetite because the amphiphilic polymer is unstained. In these images, the separation of individual particles is not clearly shown inside the clusters. Transmission electron micrographs of the clusters show mostly flattened structures, suggesting that their hydrophobic cores may be fluid-like at room temperature which could be due to the oleic acid coating around the magnetite nanoparticles.

(a) 75 volume percent



(b) 83 volume percent



(c) 90 volume percent

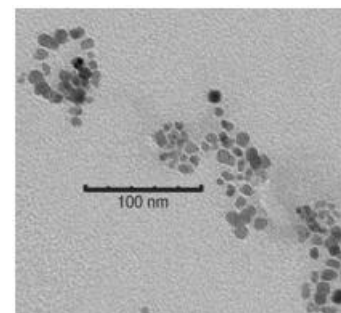


Figure 3.11- Images of magnetite clusters at different supersaturation values in the mixer
 This is because some small amount of magnetite precipitated during the dialysis procedure.

Table 3-10 summarizes the experimental weight percents of organic material and magnetite composition in the magnetite clusters at different supersaturation values. These results show lower magnetite composition than expected. This is because some small amount of magnetite precipitated during the dialysis procedure.

Table 3-10. Organic and magnetite composition in clusters using oleic acid at Reynolds number 15,500
 (Calculated from equation 3.19 and 3.20).

Water volume percent in the mixer	Supersaturation value	$X_{mag,final}$	$X_{OA,final}$	$X_{F127,final}$
75	7.2 E19	$0.31 \pm 0.05^{**}$	0.05	0.64
83	8.8 E21	0.32	0.05	0.63
90	3.5 E23	$0.13 \pm 0.01^{**}$	0.02	0.85
NA*		0.43	0.07	0.50

***Theoretical composition of magnetite clusters when the magnetite and F127 polymer are injected in the MIVM at a wt/wt ratio of 1/1. ** Expected error values**

The average chain density (ξ) on the cluster surface was estimated for three samples at three different Reynolds numbers using the number average diameter from NTA and compositions of the magnetite clusters. This assumes that all of the injected F127 polymer was incorporated into the clusters and that all of the PEO chains in the F127 were at the surface of the

clusters. Table 3-11 shows the experimental number of chains per nm^2 of polymer in the surface of magnetite clusters at different water volume percent in the mixer. This is important to determine the effect of the polymer compositions and steric repulsion energy between nanoparticles on the stabilization of clusters in solution.

Table 3-11. Experimental number of chains per 1 nm^2 on the surface area of magnetite clusters at different Reynolds numbers with initial concentrations of 0.5 mg/ mL for magnetite and F127 and at different Water volume percent in the mixer

Water volume percent in the mixer	Number Diameter (nm)	Surface area (nm^2)	Chains (f)	ξ^* chains/nm^2
75	73	17 E+03	5.2 E+04	3.1
83	74	17 E+03	5.1 E+04	2.9
90	70	15 E+03	1.4 E+05	9.4

*Calculated from equation 3.21 and the clusters were assumed to be spheres.

3.4.8 Stability of Nanoparticles

The stability of particle sizes of magnetite clusters made at two different Reynolds numbers - 21,500 and 15,500 - and at 75 volume % water in the mixer was studied as shown in Figure 3.12 and Figure 3.13 for several days. For magnetite clusters at $Re = 21,500$, the sizes were constant during 90 days. For magnetite clusters at $Re = 15,500$, the sizes were constant for five days. After 5 days, sizes of clusters were slowly increasing over time. Magnetite clusters at Reynolds number of 21,500 are more stable than cluster formation at 15,500 may be due to the very high turbulence formation in the first case. These results suggest that particles were colloidally stable over time during this period where no sedimentation or flocculation occurred.

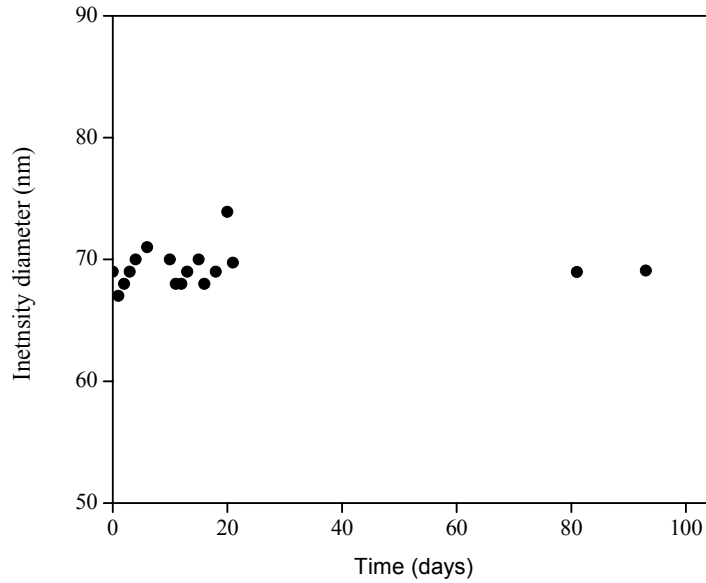


Figure 3.12. The stability of magnetite clusters encapsulated in F127 as a function of time with initial concentrations of 0.5 mg/ mL for magnetite and F127 at Reynolds numbers of 21,500 and at 75 water volume percent in the mixer

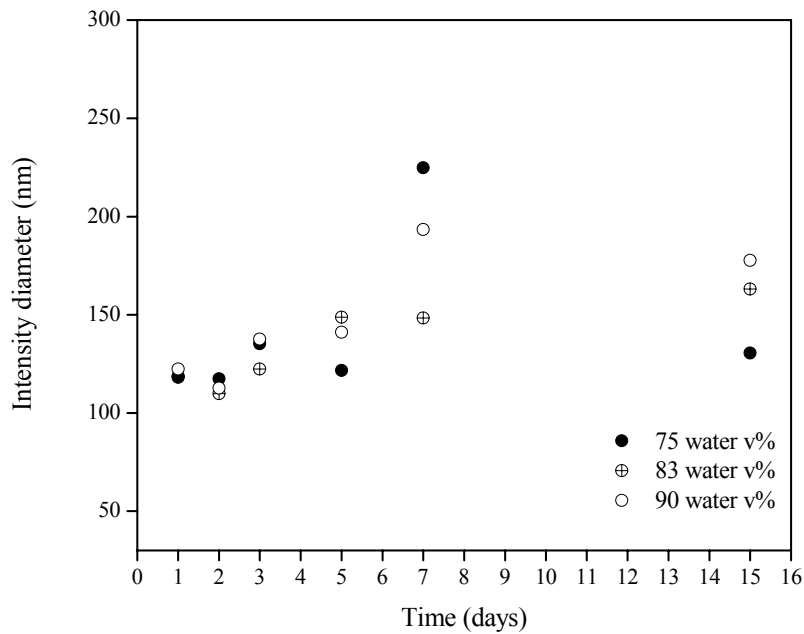


Figure 3.13. The stability of magnetite clusters encapsulated in F127 as a function of time with initial concentrations of 0.5 mg/ mL for magnetite and F127 at Reynolds numbers of 15,500 and at different water volume percent in the mixer

3.4.9 Effect of magnetic field

A magnetic field was applied to the magnetite clusters made at $Re = 5,000$ before they were dialyzed without any dilution as shown in Figure 3.14. The magnet used was semi-circular with a diameter of 3.5 inch and a thickness of 0.25 inch. The field strength at the surface of the magnet's center was 0.48 Tesla. Particle sizes were measured by DLS before and after a magnetic field were applied for 5 days as shown in Table 3-12. The clusters were aggregated after the magnetic field was applied and these aggregates could not be broken up even after 30 min of sonication using a water bath sonicator (Cole Parmer model 8890 Ultrasonic Cleaner).



Figure 3.14. Magnetite clusters at Reynolds number of 5,000 under the influence of a magnetic field

Table 3-12. Magnetite clusters made at $Re = 5,000$ aggregate after applying a magnetic field (Before dialysis procedure)

Application of Magnetic field	PDI	Intensity Diameter (nm)
Before	0.172	117
After (no mixing)	0.097	180
After followed by sonication for 10 mins	0.111	177
After followed by sonication for 30 mins	0.116	175

3.5 Conclusions

This study demonstrates the technology to produce homogeneous nanoparticles using the MIVM by flash-nanoprecipitation. The mixer was successfully characterized using stabilized β -carotene nanoparticles with F127 with a range of intensity diameters between 120–160 nm. Also, formation of magnetite clusters at different parameters was possible with a range of number diameters between 70–200 nm and with a composition range of 0.13-0.36 weight percent of magnetite. Reynolds numbers and supersaturation values are very important parameters to control the rate of nucleation and micellization of nanoparticle formation using flash nanoprecipitation in the MIVM. Sizes of nanoparticles depended greatly on the Reynolds number in the mixer until critical a Reynolds number of 1,500 for β -carotene nanoparticles and 8,000 for magnetite clusters were reached. For $Re > 1,500$ and 8,000 for the β -carotene nanoparticles and magnetite clusters, respectively, the nanoparticle sizes were constant and independent of Reynolds numbers. For the magnetite clusters made at $Re > 8000$, the sizes were independent of supersaturation values. Particle size was primarily studied using Dynamic Light Scattering and NTA tracking techniques. Also, the morphology of the magnetite clusters could be studied using electron microscopy with a typical number of magnetite particles per clusters of 23 ± 11 . Magnetite nanoparticles were shown to be stable up to at least 5 days at room temperature and control of magnetite cluster composition could be possible by controlling the injected oleic acid-coated magnetite and F127 weight ratio, the Reynolds number and the water content in the mixer.

3.6 Acknowledgements

The authors gratefully acknowledge support from: NSF/ARC Materials World Network for the Study of Macromolecular Ferrofluids (DMR-0602932), Omnova Solutions, NSF IGERT Grant #DGE-0114346, NSF MILES-IGERT program, Institute for Critical Technology and Applied Science at VT. The authors also wish to thank Professor Robert K. Prud'homme for advice and help in constructing the mixer.

4 Formation of Colloidally Stable Magnetite Nanoparticle Clusters by Rapid Precipitation

*Raquel Mejia-Ariza, Sharavanan Balasubramaniam, Oguzhan Celebi, Philip P. Huffstetler, William C. Miles, Judy S. Riffle, Richey M. Davis**

Macromolecules and Interfaces Institute, Virginia Tech, Blacksburg, Virginia 24061

This chapter will be submitted to Langmuir

4.1 Abstract

Clusters of ~7 nm magnetite nanoparticles with controlled size and composition were produced by rapid precipitation using a Multi-Inlet Vortex Mixer (MIVM). Aqueous suspensions of magnetite nanoparticle clusters were formed by rapid mixing of an organic phase containing the hydrophobically-modified nanoparticles and a stabilizing amphiphilic copolymer (Pluronic® F127) with an antisolvent to create high supersaturation. The clusters were characterized by dynamic light scattering, transmission electron microscopy, nanoparticle tracking analysis, and thermogravimetric analysis. Clusters were formed with hydrodynamic diameters in the range of 80–150 nm and with compositions ranging from 20-45 weight percent of magnetite. The nanoparticle clusters were found to be colloidally stable over the range of sizes and compositions studied. These clusters have potential applications in MRI diagnostics and targeted drug delivery.

Keywords Clusters, magnetite nanoparticles, contrast agents, multi-inlet vortex mixer (MIVM)

4.2 Introduction

There has been great interest recently in colloidal iron oxide nanoparticles because of their potential biomedical applications such as contrast-enhanced magnetic resonance imaging (MRI),^{66, 67} retinal detachment therapy,^{66, 67} hyperthermia,^{68, 69} bioseparation and targeted drug delivery.^{70, 71} Magnetite (Fe₃O₄) nanoparticles below *ca.* 20 nm in diameter are in the

superparamagnetic regime - they exist as independent magnetic monodomains that align with an external magnetic field resulting in large saturation magnetizations.⁷² When the external field is removed, thermal energy is sufficient to randomize the magnetic dipoles by overcoming dipole-dipole interactions. This absence of hysteresis and the ability to be externally manipulated, combined with low cytotoxicity, biocompatibility and stability makes superparamagnetic magnetite nanoparticles very promising candidates in physiological applications.⁷³ Furthermore, several synthetic efforts have succeeded in the creation of well-defined magnetite nanoparticles with high degree of control over particle size and size distribution,⁷⁴⁻⁷⁶ and suitable surface functionalization to render them water-dispersible.⁷⁷⁻⁸²

The controlled fabrication of secondary magnetic nanostructures, such as magnetite nanoparticle clusters, is desirable from the standpoint of easier external manipulation using magnetic fields. In order to increase the net magnetic moment, the formation of controlled clusters of magnetite nanoparticles is a better strategy than increasing the size of the primary nanoparticles, as the latter would result in a loss of superparamagnetic characteristics. Moreover, controlled clusters are also known to yield higher transverse relaxivity (r_2) than the primary nanoparticles, leading to better contrast in T_2 -weighted MRI.⁸³ Several works have reported the synthesis/fabrication of magnetic nanoparticle clusters.⁸⁴⁻⁸⁷ Berret et al. have described the controlled clustering of maghemite nanoparticles by electrostatic complexation using asymmetric diblock copolymers where one block was of opposite charge to that of the nanoparticles and the other block was neutral to provide colloidal stability.⁸⁸ The clusters were polydisperse aggregates with elongated structures which was likely caused by the broad size distribution of the maghemite nanoparticles synthesized by the alkaline coprecipitation method. Others have reported multi-functional magnetic nanoparticle clusters formed by emulsification and solvent evaporation methods.⁸⁵⁻⁸⁷ Although these particles produced favorable results, such as high transverse relaxivities for MRI applications, the emulsion/solvent evaporation method has some disadvantages. For example, it requires the use of stabilizing surfactants and several purification stages to obtain homogeneous cluster sizes.

Flash nanoprecipitation in a multi-inlet vortex mixer (MIVM) has been demonstrated to be an efficient and robust process for the formation of multifunctional nanoparticles by the assembly of hydrophobic solutes and amphiphilic block copolymers.^{18, 19, 89-93} In this process, an organic solution containing hydrophobic molecules or hydrophobically-modified nanoparticles

and a stabilizing copolymer is rapidly mixed with water (anti-solvent) in a small mixing chamber. Attaching an amphiphilic copolymer to the surface of nanoparticles provides steric stabilization to the colloidal dispersions and prevents aggregation due to attractive van der Waals forces.⁹⁴ The MIVM provides an approach for the formation of controlled clusters of a variety of optically and biologically active compounds, over a range of sizes and compositions with narrow size distributions. Recently, Gindy et al. have used the MIVM approach for the formation of multi-component copolymer-protected nanoparticles comprised of a model therapeutic agent and gold nanoparticles.⁸

The aim of our work is to form colloiddally stable clusters of magnetite nanoparticles with control over the size and the magnetite loading capacity. We have employed Pluronic® F127, a commercially-available, biocompatible, non-ionic macromolecular surfactant to encapsulate hydrophobically-modified magnetite nanoparticle clusters. Clusters in a range of sizes (80–150 nm) and compositions (magnetite-polymer, w/w) were formed by varying the turbulence of mixing (i.e., the Reynolds number) and supersaturation in the mixer by controlling the volume ratios of anti-solvent to solvent.

4.3 Experimental Section

4.3.1 Materials

Iron (III) acetylacetonate (99.9%), benzyl alcohol (anhydrous, 99.8%), and oleic acid (90%) were purchased from Aldrich and used as received. Pluronic® F127 triblock copolymer [(EO)₁₀₀-(PO)₆₅-(EO)₁₀₀] was obtained from Fisher and used as received. Tetrahydrofuran (THF) was purchased from EMD Chemicals and used without further purification. Reagent-grade acetone and chloroform were used as received. Water was purified by reverse osmosis and ion exchange using the Barnstead ROpure ST (Barnstead/Thermolyne, Dubuque, IA, U.S.A.) purification system.

4.3.2 Synthesis of magnetite nanoparticles coated with oleic acid

Magnetite nanoparticles were synthesized according to a published procedure using benzyl alcohol both as the solvent and reducing agent.⁷⁵ Fe (III) acetylacetonate (2.14 g, 8.4

mmol) was added to benzyl alcohol (45 mL, 0.43 mol) in a 250-mL, three-neck round bottom flask equipped with a water condenser and placed in a Belmont metal bath with an overhead mechanical stirrer with thermostatic (± 1 °C) and stirring rate control. The reaction mixture was heated to 100 °C and sparged with nitrogen gas for 1 hour. While stirring under nitrogen, the solution was heated to 205 °C over 4 hours and maintained at this temperature for 40 hours. The resulting suspension was cooled to room temperature and the nanoparticles were separated by centrifugation (2500 rpm, 15 mins). The isolated nanoparticles were washed thoroughly with acetone, collected by magnetic decantation and dried by sparging nitrogen at 25 °C for 1 hour. The product was dispersed in chloroform (25 mL) with the addition of oleic acid (0.3 mL). Subsequently, the chloroform was removed by rotary evaporation and the resulting oleic acid-coated-magnetite nanoparticles were washed with acetone and dried under nitrogen at 25 °C for 24 hours.

4.3.3 Determination of critical concentrations of magnetite and F127

The simultaneous aggregation of oleic acid-coated magnetite nanoparticles and micellization of Pluronic® F127 triblock copolymer is desired to prevent the formation of dead micelles and unprotected clusters. The kinetics of this process depends on the composition of the liquid phase in the mixer (water/THF ratio).^{23, 59, 95} The concentration of oleic acid-coated magnetite, C_{cwc} , at which oleic acid-coated magnetite nanoparticles start to aggregate and the critical micelle concentration, C_{cmc} , of the F127 for a given liquid phase composition in the MIVM are important considerations for the formation of stable oleic acid-coated magnetite nanoparticle clusters. Values of C_{cwc} and the C_{cmc} were measured at 25 ± 0.1 °C by dynamic light scattering (DLS) using a Zetasizer Nano ZS (Malvern Instruments Ltd., Malvern, U.K.) equipped with a 4 mW He-Ne laser source operating at 633 nm and 173o backscatter detection. We started with suspensions of dispersed oleic acid-coated magnetite nanoparticles in THF and fully dissolved solutions of F127, also in THF, and determined the onset of aggregation (oleic acid-coated magnetite) and micellization (F127) as water was added incrementally. The number-average diameter and scattering intensity count rate were measured and reported as a function of water concentration for oleic acid-coated magnetite and F127, respectively. In the case of F127, a constant measurement placement and attenuator setting were used to ensure that the incident light intensity was consistent. The experimentally obtained data were fitted to exponential

equations (see Figure 4.1) to yield the respective critical water concentration curve for oleic acid-coated magnetite and micellization curve for F127. An exponential fit was used because it has the highest correlation coefficient compared with other fits. This plot was used to choose the operating conditions (e.g. 75 vol% water) to afford stable clusters where all the injected F127 encapsulated the nanoparticle clusters. For the critical water concentration experiments, ~8 nm magnetite nanoparticles coated with oleic acid/oleylamine were synthesized following a published ‘seed-mediated growth’ technique.⁶⁰ The similarity of the coating on these particles to that on the particles used to make the clusters with the MIVM meant that the measured values of C_{ccw} could be used to estimate the supersaturation in the mixer experiments.

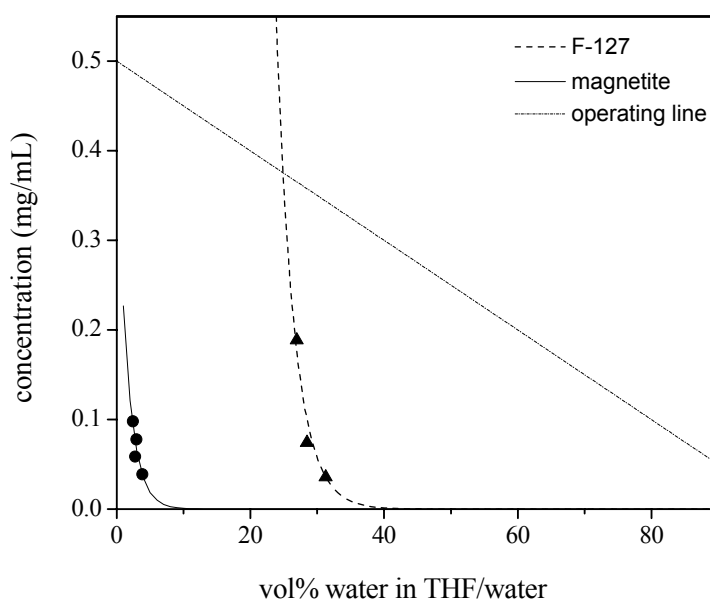


Figure 4.1. Critical micelle concentration of F127 and critical water concentration of oleic acid and oleylamine coated magnetite for forming clusters of magnetite at 25 °C

4.3.4 Preparation of magnetite clusters stabilized with F127

The multi-inlet vortex mixer had four inlets tangential to the boundary and an outlet at the center of the mixing chamber as depicted in Figure 4.2. The four inlet streams were connected to four syringes – one holding the magnetite and F127 dissolved in THF and three others holding the aqueous solvent (de-ionized water). The mixer chamber had a diameter of 5.9 mm and the inlet and the outlet stream inner diameters were 1.1 mm and 1.3 mm, respectively. The temperature for the formation of clusters was maintained at 25 ± 1 °C by passing the injected

flow streams through stainless steel coils (OD: 3.175 mm) submerged in a water bath (NESLAB RTE-100) which in turn were connected to Teflon tubes (OD: 3.175 mm) that fed into the mixer. For all experiments, the organic stream flow rate was controlled by a syringe pump (KDS 200, KD Scientific Inc., New Hope, PA) and the three water stream flow rates were controlled by a programmable syringe pump (Harvard Apparatus PHD 4000, Holliston, MA). Labview 8.0™ was used to program the pumps and control the flow rates. Flow rates of the inlet streams were calculated by first specifying the Reynolds number (Re) at which the mixer was to be operated. The Reynolds number is defined by the following equation:

$$\text{Re} = D_{\text{mixer}} \sum \frac{u_i}{\nu_i} \quad (4.1)$$

where D_{mixer} is the mixer diameter, u_i is the velocity of each inlet stream, and ν_i is the kinematic viscosity of each solvent.

Clusters formation was studied as a function of three variables: the Reynolds number (Re) which affects the mixing time, the water (anti-solvent) composition in the mixer which affects supersaturation, and the magnetite-polymer weight ratio which affects the cluster composition and steric stabilization. The initial concentration of magnetite nanoparticles in THF was kept constant at 0.5 mg mL^{-1} . This concentration was chosen because the oleic acid-coated magnetite nanoparticles were fully dispersed in THF. The concentration of F127 was varied to obtain F127-magnetite ratios of 0.1:1, 0.5:1, and 1:1 (w/w). The Reynolds number was 15500 and the water composition in the mixer was 75 vol%. The initial F127-magnetite composition of 1:1 was selected to investigate the effect of varying the (i) Reynolds number in the range 100-15500 (at a fixed water concentration in the mixer of 75 vol%), and (ii) water composition in the mixer at 75%, 83% and 90% (at fixed $\text{Re} = 15500$). The formed clusters were subsequently dialyzed against de-ionized water for 24 hours using a 25,000 g/mol MWCO cellulose acetate dialysis bag to remove THF and free unimers of F127. For each change of de-ionized, the volume of de-ionized was about 10 times the sample volume. Each dialysis step included 5 changes of de-ionized water. The samples were then freeze-dried for 72 hours at 3 mBar vacuum and $-50 \text{ }^\circ\text{C}$. Finally, thermogravimetric analysis of the clusters was performed to determine the experimental compositions of magnetite, oleic acid and F127.

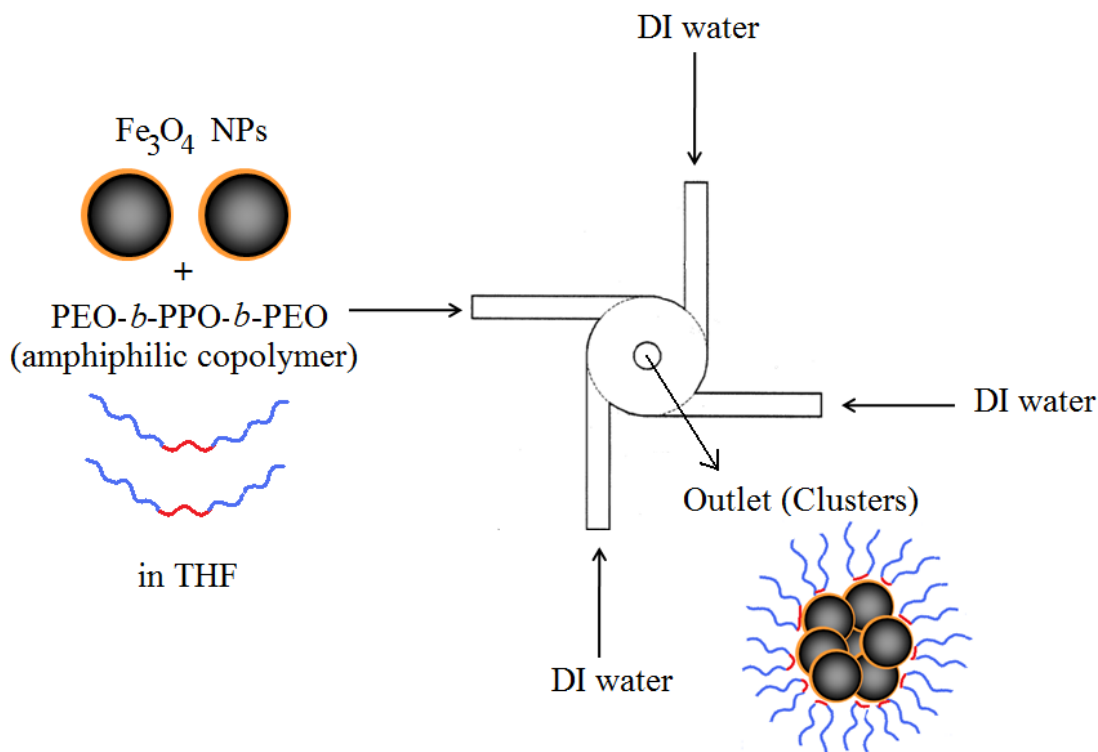


Figure 4.2. Schematic illustration of the formation of copolymer stabilized-magnetite nanoparticle clusters via rapid precipitation using a multi-inlet vortex mixer (MIVM). (Adapted from Gindy et. al).³⁴

4.3.5 Characterization of Clusters

The hydrodynamic sizes and polydispersity indices (PDI) of the magnetite nanoparticles and clusters were characterized by dynamic light scattering at 25 ± 0.1 °C using the Zetasizer Nano ZS. The autocorrelation functions of the scattered intensity were fitted using cumulants analysis using ZS 6.12 software to extract the average translational diffusion coefficient and the hydrodynamic diameters were determined through the Stokes-Einstein relation.⁶² Typically, samples were diluted in de-ionized water to ~ 0.01 - 0.02 mg/mL, sonicated using a water bath sonicator (Model 8890, Cole-Parmer, Chicago, IL) for 10 minutes and passed through a $1.0 \mu\text{m}$ PTFE syringe filter before measurements. The intensity-average diameter (D_I), volume-average diameter (D_V), number-average diameter (D_N), and polydispersity index (PDI) were recorded for each sample and averaged from three measurements.

The number-average (D_N) and volume-average (D_V) diameters of the nanoparticle clusters in aqueous suspensions were also measured by nanoparticle tracking analysis (NTA)

using a NanoSight NS500-HSBF (NanoSight, Amesbury, U.K.). The instrument was equipped with a sample chamber illuminated by a 405 nm laser source operating at 75 mW and a 20X microscope objective collected the scattered light on an EMCCD camera (Andor SOLIS).⁶³ The nanoparticle clusters were directly visualized as point-scatterers moving under Brownian motion and videos were recorded at 30 frames per second. Each sample was measured for 180 s with manual shutter and gain settings. The camera settings used in this technique were a gain of 10, a blur size of 3 x 3, an auto detection threshold and a minimal track length of 10 steps. The NTA 2.1 image analysis software was used to individually track the nanoparticle clusters on a frame-by-frame basis and generate number- and volume-average size distribution profiles. The sample preparation protocol was the same as that for DLS measurements except that the samples typically had to be diluted by a factor of 10-100 further for NTA analysis.

Transmission electron microscopy was performed on a Philips EM-420 field emission gun TEM at an acceleration voltage of 100 kV. The oleic acid-coated magnetite nanoparticles and the nanoparticle clusters were deposited onto amorphous carbon-coated copper grids from dilute solutions (~0.02 mg/mL) of THF and de-ionized water respectively. Images were acquired at a magnification of 96,000X, corresponding to a resolution of 3.88 pixels nm⁻¹. For the oleic acid-coated nanoparticles, particle distribution analysis was performed using Reindeer Graphics' Fovea Pro 4 plug-in for Adobe Photoshop 7.0.

Thermogravimetric analysis (TGA) was used to determine the weight fraction of magnetite in the oleic acid-coated nanoparticles and the copolymer-stabilized nanoparticle clusters. Measurements were performed on a TA Instruments Q500 TGA under a constant flow of nitrogen of 30 mL min⁻¹. Samples were held at 115°C for 15 minutes to drive off any moisture and ramped at 10 °C min⁻¹ up to a maximum of 650°C. The mass remaining at the end of the experiment was used to calculate the magnetite weight percentages in the clusters. The polymer and oleic acid compositions in the clusters were calculated as follows:

$$x_{F127,final} = 1 - x_{mag,final} \left(1 + \frac{x_{OA,initial}}{x_{mag,initial}} \right) \quad (4.2)$$

$$x_{OA,final} = 1 - x_{mag,final} - x_{F127,final} \quad (4.3)$$

where x_{F127} is the polymer mass fraction, $x_{OA,initial}$ and $x_{mag,initial}$ are the mass fractions of oleic acid and magnetite in the individual magnetite nanoparticles, and $x_{OA,final}$ is the oleic acid mass fraction in the clusters.

The number of polymer chains per nm² (ξ) in the magnetite clusters was calculated as follows.⁶⁴

$$\xi = \frac{\left(\frac{x_{F127,final} N_A \rho_{cluster} \frac{4}{3} \pi R_N^3}{M_n x_{mag,final}} \right)}{4\pi R_N^2} \quad (4.4)$$

where $x_{F127,final}$ and $x_{mag,final}$ are the mass fractions of F127 and magnetite, respectively, N_A is the Avogadro's number, $\rho_{cluster}$ is the density of magnetite clusters, R_N is the number average radius of clusters, and M_n is the number-average molecular weight of F127. The assumptions made in the above equation are (1) the clusters are spherical in suspension, (2) the PEO chain length in the attached layer on the surface of the clusters does not contribute significantly to the observed hydrodynamic diameter of the clusters (3) all of the F127 in the suspension was used to encapsulate the clusters.

4.4 Results and Discussion

4.4.1 Characterization of oleic acid-coated magnetite nanoparticles

A representative TEM image of individual magnetite nanoparticles coated with oleic acid is shown in Figure 4.3a. While the organic shell was not distinguishable, the strong electronic contrast of the iron atoms enabled visualization of the magnetite cores. Size analysis of at least 650 particles yielded a mean diameter of 6.2 ± 1.9 nm. The observed particle sizes were described by the two-parameter Weibull distribution function with shape parameter = 3.96 and scale parameter = 6.59. The amount of oleic acid coating on the nanoparticles was determined by TGA to be 15.5%. The theoretical calculated end-to-end distance for oleic acid monolayer is 2.35 nm. The theoretical size of the oleic acid-coated magnetite is 10.9 nm and the experimental number diameter (measured by DLS) of oleic-acid coated magnetite in THF is 10.5 nm. The theoretical composition of oleic acid assuming a monolayer is absorbed on magnetite surface is 43 wt%. This suggests that the coating of oleic acid on the magnetite surface was less than one monolayer.

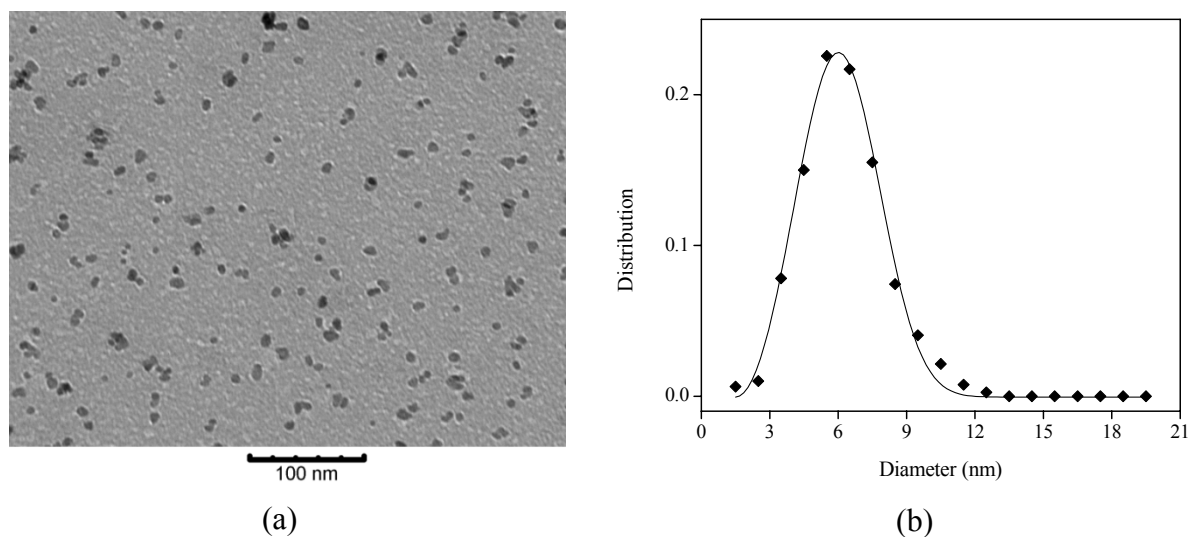


Figure 4.3. (a) TEM image of oleic acid-coated magnetite nanoparticles. (b) Size distribution obtained from image analysis performed on ~650 particles. The data points are fitted using a Weibull distribution function (continuous line).

4.4.2 Cluster size as a function of Reynolds numbers

The mixing time of the streams depends on the Reynolds number. For that reason, cluster formation at different Reynolds numbers were performed to learn how the mixing times of the magnetite and F127 affect the cluster size. After dialysis, the cluster diameters were measured using DLS and NTA and are shown in Figure 4.4b and Figure 4.5c. For size analysis, the nanoparticles were diluted by a factor of 1:5 (nanoparticles solutions to water volume ratio) and then filtered with a 1 μm PTFE filter (Whatman). Figure 4.4a shows particle size distribution of magnetite clusters at three different Reynolds numbers. This is an example of how particle size is experimental measured by DLS where the mode intensity diameter for each sample is reported. Figure 4.4b and Figure 4.5c show how the turbulence and mixing of the fluids affect the formation of the magnetite clusters. At $Re < 7,000$, the intensity-average diameter increased as Re decreased, suggesting that the mixing time τ_{mix} was larger than the time required for formation of the magnetite clusters and for copolymer self-assembly, τ_{cf} and τ_{sa} . At $Re > 7,000$, the diameters were approximately constant. In this regime, $\tau_{\text{mix}} < \tau_{\text{cf}}$ and τ_{sa} so that the cluster diameter would depend primarily on the supersaturation values.^{23, 59, 95}

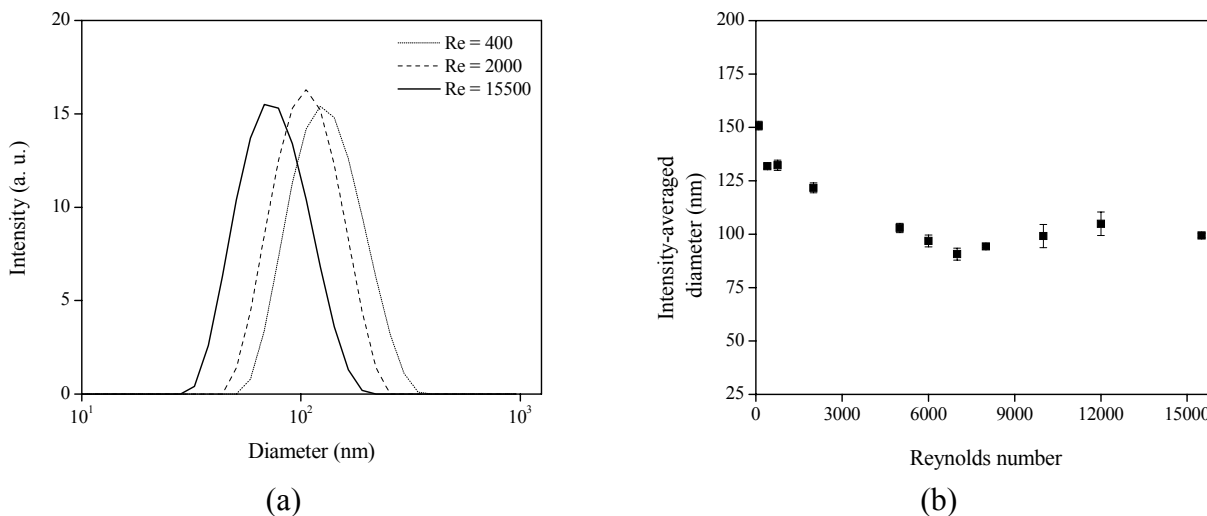
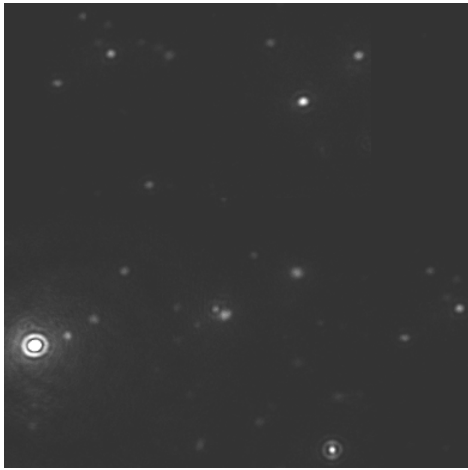


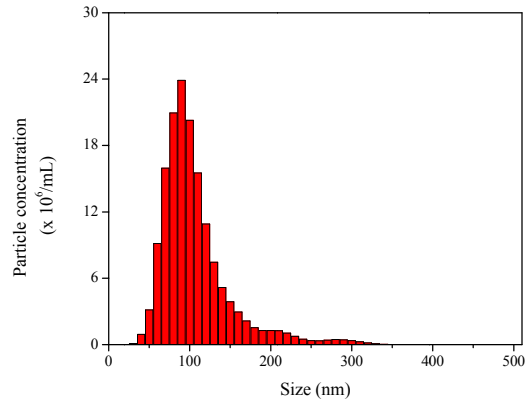
Figure 4.4. (a) Representative particle size distributions (b) Variation of D_1 as a function of Reynolds number (F127:magnetite = 1:1, 75 vol % water in the mixer)

The refractive index used in the DLS analysis was 2.3, the value for pure magnetite.⁶⁵ When weight fraction-based average of value of $n = 1.619$ (for clusters at $Re = 400$) was used, based on the typical compositions of the clusters and the known refractive indices for magnetite and F127⁹⁶, the difference in the calculated values of the volume average hydrodynamic diameter D_v compared to that calculated assuming the clusters were pure magnetite was $\sim 1\%$. [The intensity diameter does not depend on refractive index but the volume D_v and number average D_N do.] Size distributions obtained by DLS size are very sensitive to the larger sizes in the distributions.

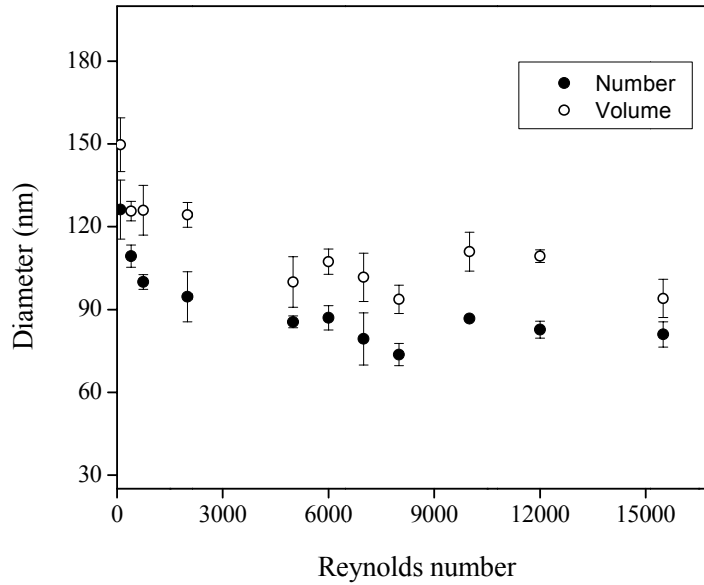
NTA enables sample visualization as shown in Figure 4.5a and provides approximate particle concentrations as a function of diameter as shown Figure 4.5b, which is a very useful feature for understanding the particle size distribution. In NTA, nanoparticles are tracked and counted individually and then related to their Brownian motion and thus the technique complements DLS. In DLS, if particles are in the Mie regime (diameter approximately > 60 nm in the present case), the refractive indexes of the materials have to be known in order to calculate number and volume diameters. However, the refractive indexes of the materials are not required for NTA measurements. This and other differences between DLS and NTA means that the comparison of number and volume-average diameters measured by the two techniques is not necessarily straightforward.



(a) $Re = 2000$



(b) $Re = 2000$



(c)

Figure 4.5. (a) Visualization of nanoparticles using NTA (b) Representative particle size distributions (c) Number and volume diameters using NTA (F127:magnetite = 1:1 wt/wt, 75 vol % water in the mixer).

In Figure 4.5c, the number and volume diameters exhibit the same trend with Re as seen with the intensity diameters obtained by DLS shown in Figure 4.4b.

A detailed comparison of the effect of Reynolds numbers on cluster size is shown in Table 4-1. After the clusters were formed and dialyzed (Spectrum Laboratories™, MWCO 25,000), they were diluted by a factor of 1:5 (nanoparticles solutions to water volume ratio) and then filtered with a 1 um PTFE filter. As with Figure 4.4b and Figure 4.5c, also shows that the cluster diameter decreased as Re increased. Particle sizes measured by DLS had PDI values between 0.09-0.12 which typically correspond to narrow size distributions like those found with calibration latex particles.⁹⁷

Table 4-1- Intensity diameters using DLS and Nanosight for clusters made with injected concentrations of [magnetite] and [F127] = 0.5 mg/mL. The liquid phase composition in the mixer = 75 vol % water. In the NTA experiments, particle concentrations were measured in the range 2.95-3.56 x 10⁶ particles/mL, and triplicates were run on a given sample.

Re	Diameter by DLS (nm)			PDI	Diameter by NTA (nm)	
	Number	Volume	Intensity		Number	Volume
400	87 ± 1	121 ± 2	137 ± 2	0.089	115 ± 10	133 ± 9
2000	70 ± 0.1	91 ± 1	111 ± 1	0.094	83 ± 1	96 ± 6
15500	46 ± 1	59 ± 1	79 ± 1	0.122	68 ± 3	77 ± 5

4.4.3 Formation of magnetite clusters at different polymer compositions

Table 4-2 summarizes the organic and magnetite composition in the magnetite clusters obtained while varying the polymer:magnetite wt/wt ratios in the stream injected into the MIVM and the Reynolds number. The polymer:magnetite wt/wt ratio had the greatest effect on magnetite weight fraction in the clusters, reaching a maximum value of 0.45 for a 0.1:1 ratio. For clusters formed at Re = 15,500 and at 75 volume % water in the mixer, the cluster diameter decreased. The F127 stabilizer more effectively arrested the growth of clusters at higher polymer concentrations as shown in Table 4-3. It is interesting to note that the magnetite composition of the clusters did not vary significantly with Re. These results show lower magnetite composition than what would be expected if all of the magnetite nominally in the THF suspension that was injected was incorporated into clusters.

Table 4-2. Organic and magnetite weight fraction in clusters at different Reynolds numbers calculated with equations 2-4 (F127:magnetite = 1:1, mg/mL, 75 vol % water in the mixer)

Polymer to magnetite weight fraction composition	Reynolds number	$X_{mag,final}$	$X_{OA,final}^2$	$X_{F127,final}^3$
0.1:1	15500	0.45 ± 0.08	0.07	0.48
NA ¹		0.76	0.15	0.09
0.5:1	15500	0.31 ± 0.07	0.05	0.65
NA ¹		0.56	0.11	0.33
1:1	400	$0.20 \pm 0.04^*$	0.04	0.74
	2000	$0.22 \pm 0.02^*$	0.04	0.69
	15500	0.29 ± 0.08	0.05	0.66
NA ¹		0.42	0.08	0.50

*Expected error

- (1) Theoretical composition of magnetite clusters assuming no loss of magnetite when the F127 polymer and magnetite injected in the MIVM at wt/wt ratios of 1:1, 0.1:1, and 0.5:1.
- (2) Calculated from equation (4.3).
- (3) Calculated from equation (4.2).

Table 4-3. Intensity diameters using DLS and Nanosight for clusters made with F127:magnetite compositions of 0.1:1, 0.5:1, 1:1 w/w. The liquid phase composition in the mixer = 75 vol % water. In the NTA experiments, particle concentrations were measured in the range $1.13\text{-}3.36 \times 10^6$ particles/mL, and triplicates were run on a given sample.

Weight fraction of polymer to magnetite in the mixer	Intensity diameter (DLS), nm	PDI	Diameter by NTA (nm)	
			Number	Volume
0.1:1	98 ± 1	0.055	73 ± 3	84 ± 3
0.5:1	76 ± 1	0.086	72 ± 4	83 ± 12
1:1	79 ± 2	0.122	68 ± 3	77 ± 5

The average chain density (ξ) was calculated for three samples at three different polymer/magnetite compositions ($Re = 15,500$) using the number average diameter from NTA, and compositions of the magnetite clusters with a 2 chains/nm² for 0.1:1 (F127:magnetite w/w), 5.29 chains/nm² for 0.5:1 (F127:magnetite w/w), and 2.04 chains/nm² for 1:1 (F127:magnetite w/w). This is important to determine the effect of the polymer compositions and steric repulsion energies between nanoparticles for the stabilization of clusters in solution. More polymer chains are attached to surface of the clusters at lower Reynolds numbers.^{64, 98, 99}

Dispersions of magnetite clusters were cast onto carbon grids and analyzed by TEM. Representative TEM micrographs of clusters of Reynolds number of 2000 are shown in Figure 4.6. These images only show magnetite particles because the amphiphilic polymer is unstained. The separation of individual particles in a cluster is clearly seen. Also, using these images, individual magnetite can be counted in the clusters. The average number of magnetite nanoparticles per cluster in Figure 4.6 is approximately 23 ± 12 . The micrograph on the left suggests that the clusters were well-dispersed which is consistent with the DLS (Figure 4.4) and NTA results.

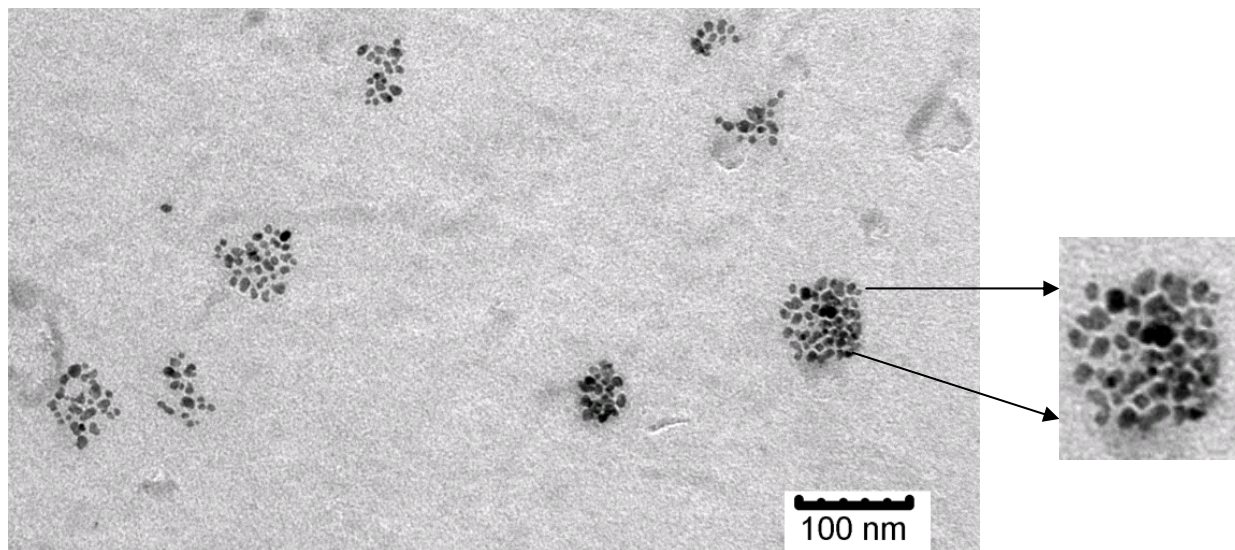


Figure 4.6. Images of magnetite clusters at Reynolds number of 2000 (F127:magnetite = 1:1, 75 vol % water in the mixer)

A representative TEM micrograph of clusters formed at injection conditions of 0.1:1 polymer:magnetite wt:wt is shown in Figure 4.7. Just as in Figure 5, the micrograph suggests that the clusters were well-dispersed. The average number of nanoparticles per cluster, $[71 \pm 35]$, is further proof that the magnetite loading in the clusters increases as the injected polymer:magnetite ratio decreased.

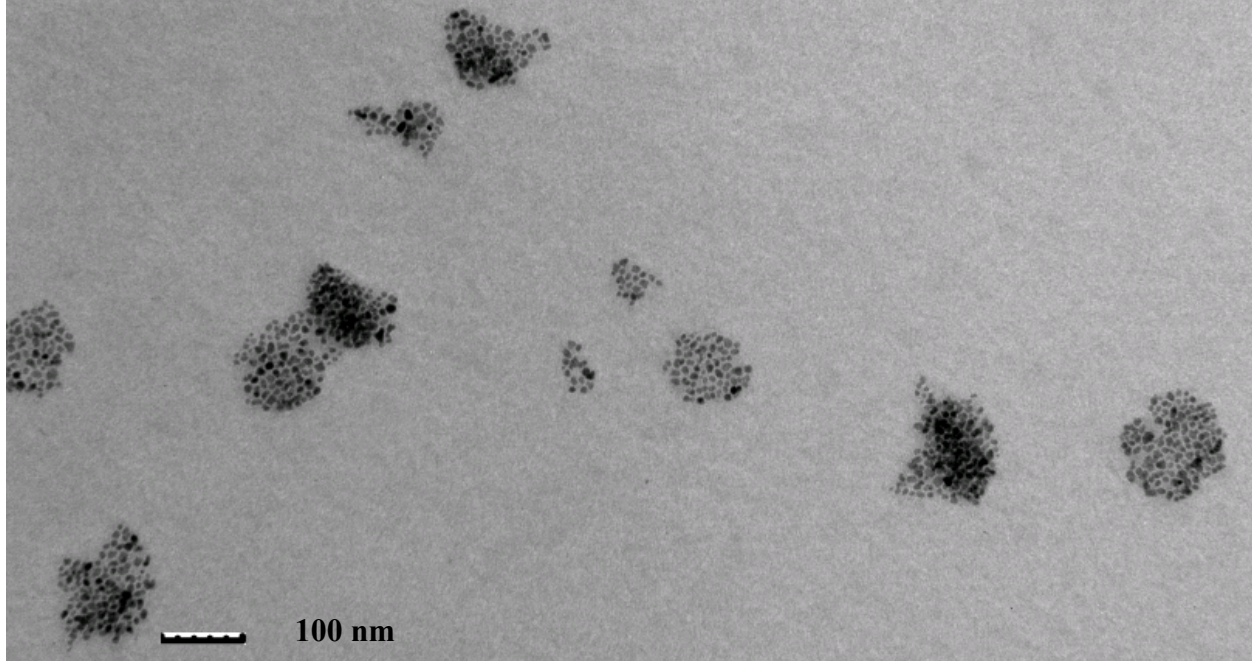


Figure 4.7. Images of magnetite clusters formed with the injection condition F127:magnetite (0.1:1) ($Re = 15,500$, 75 vol % water in the mixer).

4.4.4 Oleic acid-coated magnetite Cluster Formation at Different Supersaturation Values

The oleic acid-coated magnetite nanoparticles used in this section was synthesized from another batch (different from the rest of the experiments) within a core magnetite diameter of 6.3 ± 0.31 nm, a number diameter of 12 nm (nanoparticles suspended in THF) and a weight percent of magnetite and oleic acid of 82 wt% and 18 wt%, respectively. Oleic acid-coated magnetite clusters were formed at different water concentrations in the mixer of 75, 83, and 90 volume% and at a fixed Reynolds number of 15,500. The Reynolds number of 15,500 was chosen because this was the mixer operating regime where the mixing time was demonstrably shorter than the nucleation and aggregation time and so the cluster size would mainly vary with supersaturation S , defined as:

$$S = \frac{C_{mag-mixer}}{C_{cwc}} \quad (4.5)$$

where $C_{mag-mixer}$ is the concentration of magnetite in the mixer and C_{cwc} is the water concentration of oleic acid-coated magnetite.

Table 3 shows the sizes of magnetite clusters at different water volume percent in the mixer using DLS and NTA, respectively.

Table 4-4. Intensity diameters using DLS and Nanosight at different supersaturation values in the MIVM. F127:magnetite 1:1 w/w, Re = 15,500.

Water volume % in the mixer	Supersaturation value	Intensity diameter by DLS (nm)	PDI	Concentration # particles/mL x10 ⁶	Diameter by NTA (nm) Number Volume	
75	7.2 E19	106 ± 3	0.224	3.06	66 ± 2	92 ± 2
83	8.8 E21	95 ± 13	0.292	3.56	66 ± 3	85 ± 3
90	3.5 E23	96 ± 4	0.161	2.49	68 ± 8	99 ± 10

After the clusters were formed and dialyzed (Spectrum Laboratories™, using a MWCO 25,000), they were diluted and then filtered with a 1µm PTFE filter. The results also show good reproducibility in term of particle size. These results show that diameters of the clusters are independent of the water concentration in the mixer in the range 75-90 volume %. The reason for this is not well-understood but it may be due to the very high values of S for even the lowest water concentration. The TEM of clusters made at different supersaturations of 83 and 90 are similar in appearance to those shown in Figure 4.6.

4.4.5 Stability of Nanoparticles in Suspension

The colloidal stability of the magnetite nanoparticle clusters in de-ionized water at different polymer compositions and Reynolds numbers was studied using DLS. The intensity-weighted diameter was recorded every 30 minutes for 24 hours. The intensity average diameter was reported because of its sensitivity to the presence of aggregates. As shown in Figure 4.8, the hydrodynamic sizes of the clusters formed at various mixing conditions and compositions did not change significantly over a period of 24 hours. The nanoparticle clusters were stable in suspension without any noticeable sedimentation or flocculation for a week.

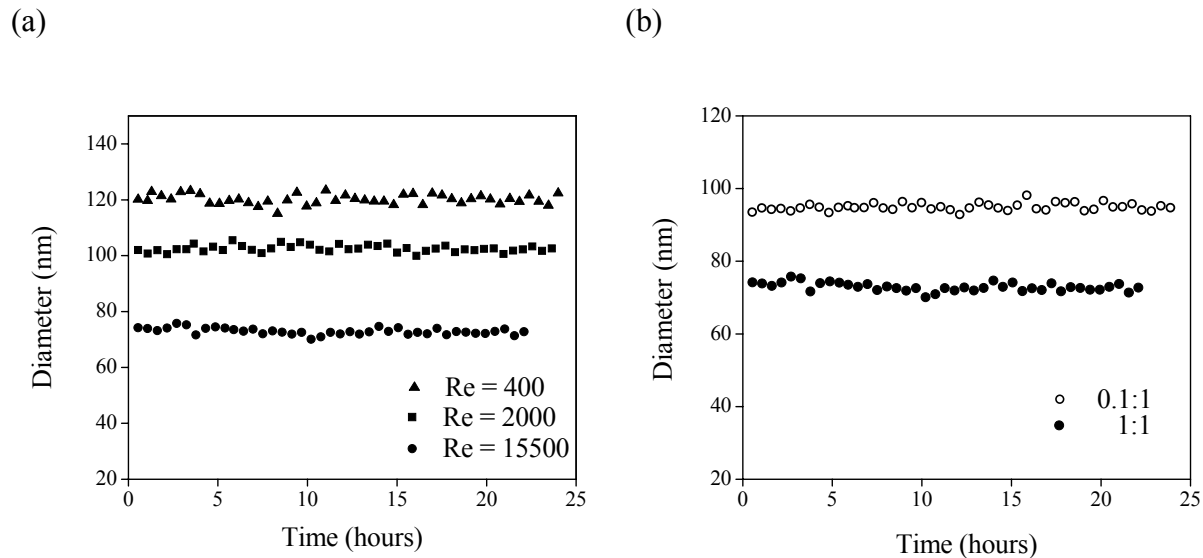


Figure 4.8. Colloidal stability of magnetite nanoparticle clusters formed at (a) different Reynolds numbers (F127:magnetite = 1:1, 75 vol % water in the mixer) (b) different compositions of injected F127:magnetite (Re = 15,500, 75 vol % water in the mixer).

4.4.6 Magnetite Cluster Stability in a Magnetic Field

A magnetic field was applied to magnetite clusters as shown in Figure 4.9. The magnet used was 88.9 mm by 161.29 mm magnet with a field strength of 0.48 Tesla. Particle sizes were measured by DLS before and after a magnetic field were applied. Before the magnetic field is applied, magnetite clusters have a diameter of 124 ± 2 nm (PDI is 0.111 ± 0.010). After 15 hrs under the influence of a magnetic field, aggregation of the clusters was observed in the bottom of the cuvette as shown in Figure 4.9b within diameter of 105 ± 2 nm (PDI is 0.105 ± 0.012). The diameters decreased after the magnetic field was applied because aggregations were removed. After the solution was sonicated for 5 mins, nanoparticles solution had the same size as before within an intensity-averaged diameter of 125 ± 4 nm (PDI is 0.112 ± 0.018) suggesting that magnetite clusters diameters could redisperse in solution using sonication.

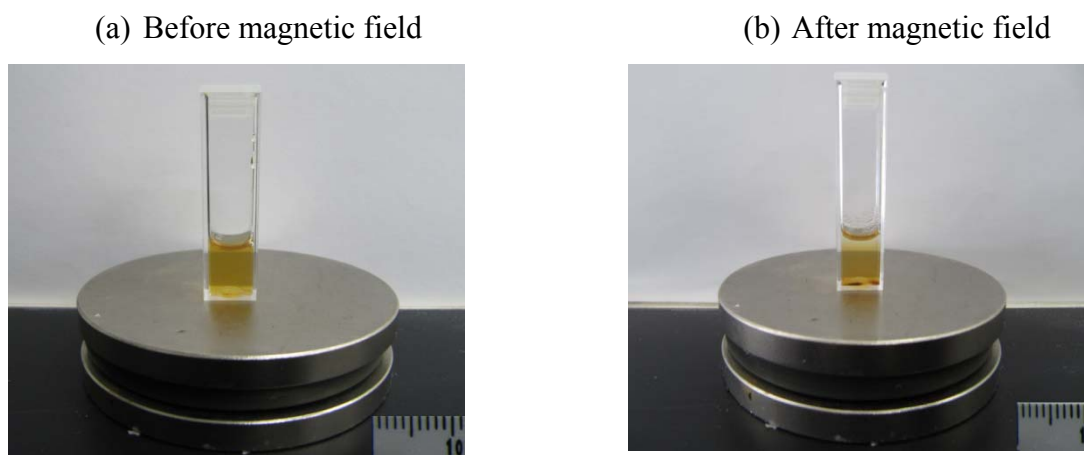


Figure 4.9. Magnetite clusters at Reynolds number of 2000 under the influence of a magnetic field

4.5 Conclusions

This study demonstrates a technique for producing colloidally stable clusters of hydrophobically modified magnetite nanoparticles encapsulated by an amphiphilic polymer with cluster diameters ranging from 50–150 nm and compositions ranging from 20–45 weight percent of magnetite. Using a rapid precipitation method, the magnetite cluster size decreased as the Reynolds number of the mixing process increased for $Re < 7,000$. Above this value, the cluster sizes were constant and independent of Reynolds numbers and supersaturation values that were controlled by varying the water volume content in the mixer. The clusters were sterically stabilized using the triblock copolymer Pluronic F127 that was injected into the mixer along with the hydrophobically modified magnetite particles. When the polymer:magnetite weight ratio was increased from 0.1:1 to 1:1, the intensity weighted hydrodynamic diameter of the cluster, as measured by dynamic light scattering, decreased from approximately 100 nm to 80 nm but the cluster composition did not change significantly. Transmission electron micrographs of the clusters show mostly flattened structures, suggesting that their hydrophobic cores may be fluid-like at room temperature which could be due to the oleic acid coating around the magnetite nanoparticles. The number of magnetite particles per clusters could be counted with a typical average number of 23 ± 12 using electron microscopy. The clusters were colloidally stable for as long as 24 hours and for at least six days. The clusters could be aggregated using a 0.48 Tesla permanent magnet but could be redispersed after the magnetic field was removed using sonication.

4.6 Acknowledgement

The authors are grateful for the financial support of the NSF/ARC Materials World Network for the Study of Macromolecular Ferrofluids (DMR-0602932), Omnova Solutions, NSF IGERT Grant #DGE-0114346, NSF Miles-IGERT program, and the Institute for Critical Technology and Applied Science at VT. The authors thank Professor Robert K. Prud'homme for advice and help in constructing the mixer.

5 Conclusions and Future Work

The work concerns the formation of colloiddally stable magnetite clusters using a Multi Inlet Vortex Mixer (MIVM) via rapid flash nanoprecipitation. The knowledge gained from this work is intended to aid in the design of new nanoparticle systems by controlling their size and composition for biomedical applications. The results obtained from size analysis and the composition of these materials has been interpreted from a colloidal perspective. The first half of this chapter describes the conclusions and the second half describes possible future work.

5.1 Conclusions

In Chapter 3, we demonstrated the technology to produce homogeneous nanoparticles using the MIVM by flash-nanoprecipitation. The mixer was successfully characterized using stabilized β -carotene nanoparticles with F127 with a range of intensity-average diameters between 120–160 nm. Particle size was primarily studied using dynamic light scattering (DLS) and nanoparticle tracking analysis (NTA). Formation of magnetite clusters at different parameters was possible with a range of number-average diameters between 70–200 nm and with a composition range of 0.13-0.36 weight percent of magnetite. Reynolds numbers (Re) and supersaturation values are very important parameters to control the rate of nucleation and micellization of nanoparticles formation using flash nanoprecipitation in the MIVM. Sizes of nanoparticles depended greatly on the Reynolds number of the fluids for Re below 1,500 for β -carotene nanoparticles and 8,000 for magnetite clusters. For Re greater than 1,500 for β -carotene nanoparticles and 8,000 for magnetite clusters, the nanoparticles sizes were constant and independent of Re. For β -carotene nanoparticle formation, the size depends on supersaturation in the range of 200-500 whereas, for magnetite cluster formation, the size did not vary significantly for supersaturations in the range of 4×10^{19} - 4×10^{22} . Also, the structure of the magnetite clusters could be studied using electron microscopy. Magnetite nanoparticles were shown to be stable over time and magnetite cluster composition was studied.

In chapter 4, we demonstrated the technology to produce colloiddally stable clusters of magnetite nanoparticles encapsulated by amphiphilic polymer for contrast agents with a range of number-average diameters (from DLS) between 50–151 nm and with a composition range of 0.16-0.39 weight percent of magnetite using a MIVM. This was possible by using an operating

region developed by the use of critical water concentrations for magnetite-oleic acid and polymer F127. Sizes of magnetite clusters depended greatly on Re in the mixer for $Re < 7,000$. For $Re > 7,000$, the cluster sizes were constant and independent of Re and supersaturation values (water volume content in the mixer). The stability of the magnetite clusters nanoparticles depended on mixing properties of the fluids such as Re and the compositions of the injected streams. The magnetite clusters were colloidally stable for several days.

5.2 Future work

5.2.1 Use of different stabilizers to study the effect of sizes in magnetite clusters

The use of different hydrophobic coatings and hydrophilic layers (polymer stabilizer structures) for the formation of magnetite clusters should be investigated. One could determine the effect of different types of polymers, hydrophilic and hydrophobic block lengths, and their block length ratios on nanoparticle formation and stability. Finally, one could examine the stability of various anchor groups that help attach polymers to the magnetite cluster surface in the presence of different solvents such as phosphate buffered saline.

5.2.2 Apply DLVO model in the magnetite clusters

The size of different complexes and their stability in suspension can be predicted over time using the density distribution model (by Vagberg et al.¹⁰⁰) and the Derjaguin-Landau-Verwey-Overbeek (DLVO) model. The latter theory concerns the effect of interparticle electrostatic, Van der Waals, magnetic (if applied), and steric forces on cluster stability at different polymer compositions and structures. These studies will be very important to design clusters that are colloidally stable in a given liquid medium for specified times.

5.2.3 Investigate how to tailor the structure and properties of magnetite clusters for MRI applications

One could measure the relaxivities of the magnetite clusters as a function of size and composition. The magnetite clusters should have higher relaxivities compared to the relaxivities of well-dispersed individual magnetite nanoparticles with core radii ~ 10 nm. When an external

magnetic field is applied, superparamagnetic nanoparticles align in the direction of the magnetic field and enhance the magnetic flux. This provides substantial disturbances in the local magnetic field through large magnetic moments and leads to a rapid dephasing of surrounding protons, generating an enormous change in the MR signal images. Polymer-stabilized SPM magnetite clusters could be very promising contrast agents.^{28, 87}

5.2.4 Create multifunctional nanoparticles for drug delivery and image analysis

Encapsulation of different hydrophobic drugs with hydrophobic polymers, F127, and magnetite clusters can be accomplished using the MIVM. The proposed method is shown in Figure 5.1.

The drug, carrier polymer, magnetite, and polymer F127 can be dissolved in an organic solvent (THF) and mixed in the mixing chamber with an anti-solvent (DI water) to precipitate the hydrophobic organic material. The nanoparticles sizes can be investigated using DLS and nanoparticle tracking analysis (NTA), the morphology can be studied using TEM and SEM, and thermogravimetric analysis, high pressure liquid chromatography (HPLC), and UV-spectroscopy can be used to measure the material compositions and drug release.

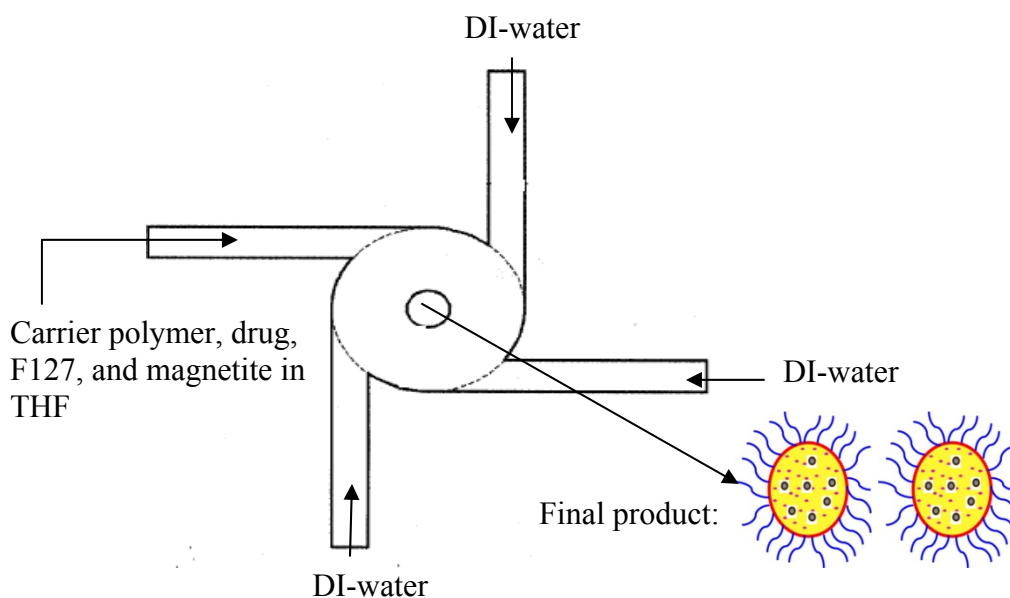


Figure 5.1. Encapsulation of hydrophobic drug via Flash Nanoprecipitation modified from Y. Liu et al.¹⁹

Appendix A: Geometry and dimensions of the MIVM

Table 6-1. Different diameters for the MIVM

D_{mixer} (inches)	0.2333
d_{is} (inches)	0.0433
D_{os} (inches)	0.0520

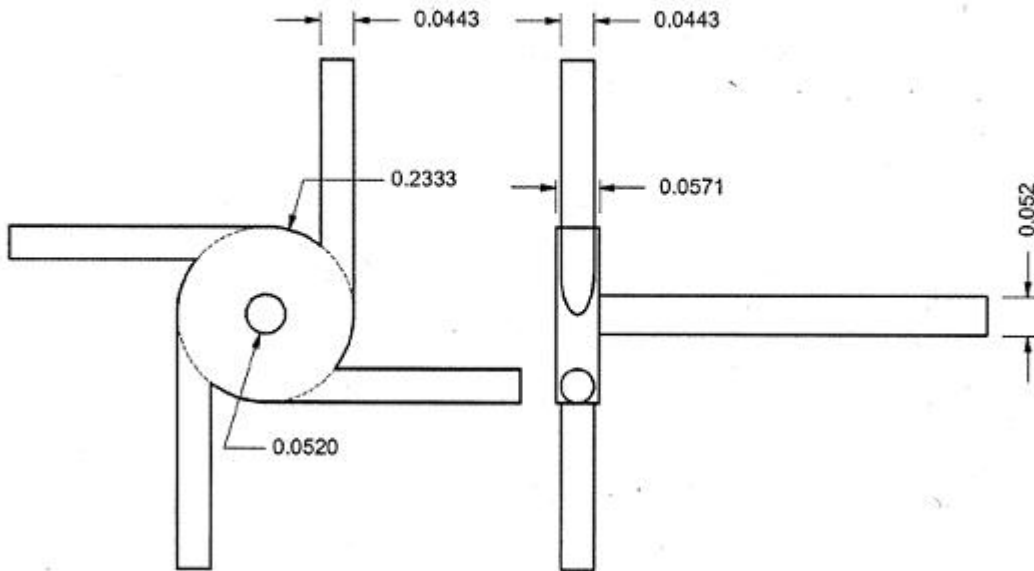


Figure 6.1. Schematics and dimensions of the MIVM

Appendix B: Appendix C - Physical Properties of Solvents Used

Table 7.1. Viscosities and Densities of THF and Water at 35 °C from thesis from Dr. Brian K. Johnson³⁰

$\rho_1 = \rho_{\text{THF}}$ (kg/m ³)	870.6
$\rho_2 = \rho_{\text{water}}$ (kg/m ³)	994.1
$\eta_1 = \eta_{\text{THF}}$ (mPa*s)	0.411
$\eta_2 = \eta_{\text{water}}$ (mPa*s)	0.741

Table 7.2. Viscosities and Densities of THF and Water at 25 °C from thesis from Dr. Brian K. Johnson³⁰

$\rho_1 = \rho_{\text{THF}}$ (kg/m ³)	881.4
$\rho_2 = \rho_{\text{water}}$ (kg/m ³)	997.1
$\eta_1 = \eta_{\text{THF}}$ (mPa*s)	0.456
$\eta_2 = \eta_{\text{water}}$ (mPa*s)	0.890

Appendix C: Calculations for the MIVM in Excel

Parameters:			
Variables:			
Parameters	Units	Value	Description
T	Celcius	25	Temperature in the mixer
Wmag	-	0.000567	weight fraction of Magnetite in THF
wf _{dib}	-	0.000567	weight fraction of F127 in THF
D _{mixer}	m	0.00592582	Diameter of the mixer
Height	m	0.0014478	Height of the mixer
A _{mixer}	m ²	2.75795E-05	Area of the mixer
V _{mixer}	m ³	3.99296E-08	Volume of the mixer
	mL	0.039929637	
d _{is}	m	0.00112522	Diameter of the inlet streams
A _{is}	m ²	9.94408E-07	Area of the inlet streams
	kg/m ³	997.10	
P _{water}	g/mL	0.9971000	density of water at 25 C'
	kg/m ³	881.40	
ρ _{THF}	g/mL	0.88140	density of THF at 25 C
η _{THF}	kg/(m*s)	0.000456	viscosity of THF at 25 C
η _{water}	kg/(m*s)	0.00089	viscosity of water at 25 C
ν _{THF}	m ² /s	5.17359E-07	Kinematic viscosity of THF
ν _{water}	m ² /s	8.92589E-07	Kinematic viscosity of water
φ _{THF}	-	0.25	Volume fraction of THF in the mixer
φ _{water}	-	0.75	Volume fraction of water in the mixer
x	s/m ²	1764635.324	Parameter to calculate velocities

Calculations:

	Equation 3.12	Equation 3.9	Equation 3.3
Re	u ₂₋₄ (m/s)	U ₁ (m/s)	Q ₁ (m ³ /s)
15000	0.478152665	0.478152665	4.75479E-07

equation 0.3

Equation 3.3		Equation 3.3	
Magnetite + F127		Water	
Q2-4(m ³ /s)	Q1(mL/min)	Q2-4(mL/min)	t _{experimental} (sec)
4.75479E-07		28.53	113.50
		28.53	

	THF	Water	Collected
	Volume in the syringes		
t(min)	$V_{is1}(mL)$	$V_{is2-4}(mL)$	$V_{totalexp}(mL)$
	1.89	53.97	53.97
Vol(ml)		59.97	59.97
	THF	Water	
	Vis2-4 can not be higher than 60 mL		This Volume include dead volume of 6 mL (for tubings)

equation 3.2		equation 3.2	
$m_1(g/min)$	$m_{2-4}(g/min)$	$m_{Magnetite}(g/min)$	$m_{Magnetite}(g)$
25.14523182	28.44600709	0.014265435	0.026985448

equation3.2			
$m_{F127}(g/min)$	$m_{F127}(g)$	$x_{Magnetite}$	x_{F127}
0.014265435		0.027	0.5
			0.5

To double check input volume fractions			
equation 3.7			In the mixer
v_{fTHF}	$v_{f(totalwater)}$	$density_{mix}(mg/mL)$	$wt\%(water)$
0.25	0.75	968.175	77.24068479

injected concentrations			equation 3.14
$wt\%(THF)$	$c_{Magnetite}(mg/mL)$	$c_{F127}(mg/mL)$	concentration in the mixer
22.75931521	0.500	0.500	$c_{Magnetite}(mg/mL)$
			0.125

concentration in the mixer		Total mass of complex
$c_{F127}(mg/mL)$	$c_{complex}(mg/mL)$	$m_{exp}(mg)$
0.125	0.250	53.971

Theoretical mass of complex (mg)	Theoretical volume (ml)
100	399.9701453

References

1. Svetlana Gelperina, K. K., Michael D. Iseman and Leonid Heifets, The Potential Advantages of Nanoparticle Drug Delivery Systems in Chemotherapy of Tuberculosis. *American Journal of Respiratory and Critical Care Medicine* **2005**, 172.
2. Sasaki, T.; Iwasaki, N.; Kohno, K.; Kishimoto, M.; Majima, T.; Nishimura, S. I.; Minami, A., Magnetic nanoparticles for improving cell invasion in tissue engineering. *Journal of Biomedical Materials Research Part A* **2008**, 86A (4), 969-978.
3. Yanase, M.; Shinkai, M.; Honda, H.; Wakabayashi, T.; Yoshida, J.; Kobayashi, T., Antitumor immunity induction by intracellular hyperthermia using magnetite cationic liposomes. *Jpn. J. Cancer Res.* **1998**, 89 (7), 775-782.
4. Liu, W.-T., Nanoparticles and their biological and environmental applications. *Journal of Bioscience and Bioengineering* **2006**, 102 (1), 1-7.
5. Brahler, M.; Georgieva, R.; Buske, N.; Muller, A.; Muller, S.; Pinkernelle, J.; Teichgraber, U.; Voigt, A.; Baumler, H., Magnetite-loaded carrier erythrocytes as contrast agents for magnetic resonance imaging. *Nano Lett.* **2006**, 6 (11), 2505-2509.
6. He, X. X.; Wang, K. M.; Tan, W. H.; Xiao, D.; Li, J.; Yang, X. H., A novel fluorescent label based on biological fluorescent nanoparticles and its application in cell recognition. *Chinese Science Bulletin* **2001**, 46 (23), 1962-1965.
7. Barratt, G., Colloidal drug carriers: achievements and perspectives. *Cellular and Molecular Life Sciences* **2003**, 60 (1), 21-37.
8. Gindy, M. E.; Panagiotopoulos, A. Z.; Prud'homme, R. K., Composite block copolymer stabilized nanoparticles: Simultaneous encapsulation of organic actives and inorganic nanostructures. *Langmuir* **2008**, 24 (1), 83-90.
9. Kwon, G. S., Diblock copolymer nanoparticles for drug delivery. *Critical Reviews in Therapeutic Drug Carrier Systems* **1998**, 15 (5), 481-512.
10. Michalet, X.; Pinaud, F. F.; Bentolila, L. A.; Tsay, J. M.; Doose, S.; Li, J. J.; Sundaresan, G.; Wu, A. M.; Gambhir, S. S.; Weiss, S., Quantum dots for live cells, in vivo imaging, and diagnostics. *Science* **2005**, 307 (5709), 538-544.
11. Loo, C.; Lin, A.; Hirsch, L.; Lee, M. H.; Barton, J.; Halas, N.; West, J.; Drezek, R., Nanoshell-enabled photonics-based imaging and therapy of cancer. *Technology in Cancer Research & Treatment* **2004**, 3 (1), 33-40.
12. Mornet, S.; Vasseur, S.; Grasset, F.; Duguet, E., Magnetic nanoparticle design for medical diagnosis and therapy. *Journal of Materials Chemistry* **2004**, 14 (14), 2161-2175.
13. Laurencin, C. T.; Nair, L. S. In *Polyphosphazene nanofibers for biomedical applications: Preliminary studies*, Conference of the NATO-Advanced-Study-Institute on Nanoengineered Nanofibrous Materials, Belek-Antalya, TURKEY, Sep 01-12; Guceri, S.; Gogotsi, Y. G.; Kuznetsov, V., Eds. Belek-Antalya, TURKEY, 2003; pp 283-302.
14. Duncan, R., Designing polymer conjugates as lysosomotropic nanomedicines. *Biochemical Society Transactions* **2007**, 35, 56-60.
15. Nori, A.; Kopecek, J., Intracellular targeting of polymer-bound drugs for cancer chemotherapy. *Advanced Drug Delivery Reviews* **2005**, 57 (4), 609-636.
16. Satchi-Fainaro, R.; Duncan, R.; Barnes, C. M., Polymer therapeutics for cancer: Current status and future challenges. *Polymer Therapeutics II: Polymers as Drugs, Conjugates and Gene Delivery Systems* **2006**, 193, 1-65.

17. Wilson, K. S.; Goff, J. D.; Riffle, J. S.; Harris, L. A.; St Pierre, T. G. In *Polydimethylsiloxane-magnetite nanoparticle complexes and dispersions in polysiloxane carrier fluids*, 7th International Symposium on Polymers for Advanced Technologies, Ft Lauderdale, FL, Sep 21-24; Ft Lauderdale, FL, 2003; pp 200-211.
18. Johnson, B. K.; Prud'homme, R. K., Chemical processing and micromixing in confined impinging jets. *Aiche J.* **2003**, *49* (9), 2264-2282.
19. Liu, Y.; Cheng, C. Y.; Prud'homme, R. K.; Fox, R. O., Mixing in a multi-inlet vortex mixer (MIVM) for flash nano-precipitation. *Chem. Eng. Sci.* **2008**, *63* (11), 2829-2842.
20. Allen, C.; Maysinger, D.; Eisenberg, A., Nano-engineering block copolymer aggregates for drug delivery. *Colloids and Surfaces B-Biointerfaces* **1999**, *16* (1-4), 3-27.
21. Song, C. X.; Labhasetwar, V.; Murphy, H.; Qu, X.; Humphrey, W. R.; Shebuski, R. J.; Levy, R. J., Formulation and characterization of biodegradable nanoparticles for intravascular local drug delivery. *Journal of Controlled Release* **1997**, *43* (2-3), 197-212.
22. Kumar, V.; Prud'Homme, R. K., Thermodynamic Limits on Drug Loading in Nanoparticle Cores. *Journal of Pharmaceutical Sciences* **2008**, *97* (11), 4904-4914.
23. Johnson, B. K.; Prud'homme, R. K., Mechanism for rapid self-assembly of block copolymer nanoparticles. *Physical Review Letters* **2003**, *91* (11).
24. Liu, Y.; Kathan, K.; Saad, W.; Prud'homme, R. K., Ostwald ripening of beta-carotene nanoparticles. *Physical Review Letters* **2007**, *98* (3).
25. Mahajan, A. J.; Kirwan, D. J., Micromixing effects in a two-impinging-jets precipitator. *Aiche J.* **1996**, *42* (7), 1801-1814.
26. Johnson, B. K.; Prud'homme, R. K. In *Flash NanoPrecipitation of organic actives and block copolymers using a confined impinging jets mixer*, Australian Colloid and Interface Symposium (ACIS), Sydney, Australia, Feb; C S I R O Publishing: Sydney, Australia, 2003; pp 1021-1024.
27. Schwert, D. D.; Richardson, N.; Ji, G. J.; Raduchel, B.; Ebert, W.; Heffner, P. E.; Keck, R.; Davies, J. A., Synthesis of two 3,5-disubstituted sulfonamide catechol ligands and evaluation of their iron(III) complexes for use as MRI contrast agents. *Journal of Medicinal Chemistry* **2005**, *48* (23), 7482-7485.
28. Kuhn, S. J.; Hallahan, D. E.; Giorgio, T. D., Characterization of superparamagnetic nanoparticle interactions with extracellular matrix in an in vitro system. *Annals of Biomedical Engineering* **2006**, *34* (1), 51-58.
29. Thorek, D. L. J.; Chen, A.; Czupryna, J.; Tsourkas, A., Superparamagnetic iron oxide nanoparticle probes for molecular imaging. *Annals of Biomedical Engineering* **2006**, *34* (1), 23-38.
30. Johnson, B. K., Flash nanoprecipitation of organic actives via confined micromixing and block copolymer stabilization. *PhD thesis, Princeton University* **2003**.
31. Torchilin, V. P., Targeted pharmaceutical nanocarriers for cancer therapy and Imaging. *Aaps Journal* **2007**, *9* (2), E128-E147.
32. Dieter Horn; Jens Rieger, Organic Nanoparticles in the Aqueous Phase - Theory, Experiment, and Use. *Angewandte Chemie International Edition* **2001**, *40* (23), 4330-4361.
33. Lipinski, C. A., Drug-like properties and the causes of poor solubility and poor permeability. *Journal of Pharmacological and Toxicological Methods* **2000**, *44* (1), 235-249.
34. Shelton, M. C. P.-D., JD; Lingerfelt, LR Jr.; Kirk, SR; Klein, S; Dressman, JR; Zoller, T; Edgar, KJ, Enhanced dissolution of poorly soluble drugs from solid dispersions in

carboxymethylcellulose acetate butyrate matrices. *ACS Symposium Series 2009, accepted for publication 2009*.

35. Agarwal, A.; Lvov, Y.; Sawant, R.; Torchilin, V., Stable nanocolloids of poorly soluble drugs with high drug content prepared using the combination of sonication and layer-by-layer technology. *Journal of Controlled Release* **2008**, *128* (3), 255-260.

36. Bontha, S.; Kabanov, A. V.; Bronich, T. K., Polymer micelles with cross-linked ionic cores for delivery of anticancer drugs. *Journal of Controlled Release* **2006**, *114* (2), 163-174.

37. Alexis, F.; Pridgen, E.; Molnar, L. K.; Farokhzad, O. C., Factors Affecting the Clearance and Biodistribution of Polymeric Nanoparticles. *Molecular Pharmaceutics* **2008**, *5* (4), 505-515.

38. Liu, H. L.; Li, J., Preparation and Characterization of Poly(PEGMA) Modified Superparamagnetic Nanogels Used as Potential MRI Contrast Agents. *Iranian Polymer Journal* **2008**, *17* (9), 721-727.

39. Z. Liang, P. C. L., *Principles of Magnetic Resonance Imaging*. 2000.

40. Kellman, P.; Ched'hotel, C.; Lorenz, C. H.; Mancini, C.; Arai, A. E.; McVeigh, E. R., High Spatial and Temporal Resolution Cardiac Cine MRI from Retrospective Reconstruction of Data Acquired in Real Time Using Motion Correction and Resorting. *Magnetic Resonance in Medicine* **2009**, *62* (6), 1557-1564.

41. R.M. Cornell, U. S., *The Iron Oxide: Structure, Properties, Reactions, Occurrences and Uses*. **1996**, VCH: New York, 1996.

42. Rosensweig, R. E., *Ferrohydrodynamics*. Cambridge University Press: New York, 1985.

43. Levitt, M. H., *Spin Dynamics: Basics of Nuclear Magnetic Resonance*. John Wiley & Sons, Ltd.: New York **2001**.

44. D. Weishaupt, V. D. K., B. Marincek, *How does MRI work?* Berlin, 2006.

45. Na, H. B.; Song, I. C.; Hyeon, T., Inorganic Nanoparticles for MRI Contrast Agents. *Advanced Materials* **2009**, *21* (21), 2133-2148.

46. Hyon Bin Na, I. C. S., Taeghwan Hyeon., Inorganic Nanoparticles for MRI Contrast Agents. *Advanced Materials* **2009**, 9999 (9999), NA.

47. Peter Caravan, Strategies for Increasing the Sensitivity of Gadolinium Based MRI Contrast Agents. *ChemInform* **2006**, *37* (35).

48. Cormode, D. P.; Skajaa, T.; Fayad, Z. A.; Mulder, W. J. M., Nanotechnology in Medical Imaging. Probe Design and Applications. *Arterioscler Thromb Vasc Biol* **2009**, ATVBAHA.108.165506.

49. Shaw, D. J., Introduction to Colloid and Surface Chemistry. *Butterworth-Heinemann, Ltd.: Oxford, 1992 4th ed.*

50. D. Fennell Evans, H. W., *The Colloidal Domain where Physics, Chemistry, Biology, and Technology Meet*. **1999**, Second Edition.

51. D. Fennell Evans, H. W., *The Colloidal Domain where Physics, Chemistry, Biology, and Technology Meet*. **1999**, Second Edition.

52. Ring, T. A., Fundamentals of Ceramic powder processing and Synthesis. **Academic Press, 1996**.

53. Mersmann, A., CALCULATION OF INTERFACIAL-TENSIONS. *Journal of Crystal Growth* **1990**, *102* (4), 841-847.

54. Kumar, V. W., L.; Riebe, M.; Prud'homme, R.; Tung, H, Formulation and Stability of Itraconazole and Odanacatib, Nanoparticles: Governing Physical Parameters *Molecular Pharmaceutics In review*.

55. Deen, W. M., Analysis of Transport Phenomena. Page 518.

56. Malvern, I., Zetasizer Nano series User manual. **2005**.
57. P. Hiemenz, R. R., Principles of Colloid and Surface Chemistry. *CRC Press* **1997**, *Third edition*.
58. Malvern, I., Zetasizer Nano QuickStart & Training Manual. **January 2006**.
59. Johnson, B. K.; Prud'homme, R. K., Flash NanoPrecipitation of organic actives and block copolymers using a confined impinging jets mixer. *Australian Journal of Chemistry* **2003**, *56* (10), 1021-1024.
60. Sun, S. H.; Zeng, H.; Robinson, D. B.; Raoux, S.; Rice, P. M.; Wang, S. X.; Li, G. X., Monodisperse MFe₂O₄ (M = Fe, Co, Mn) nanoparticles. *J. Am. Chem. Soc.* **2004**, *126* (1), 273-279.
61. Alexandridis, P.; Hatton, T. A., POLY(ETHYLENE OXIDE)-POLY(PROPYLENE OXIDE)-POLY(ETHYLENE OXIDE) BLOCK-COPOLYMER SURFACTANTS IN AQUEOUS-SOLUTIONS AND AT INTERFACES - THERMODYNAMICS, STRUCTURE, DYNAMICS, AND MODELING. *Colloids and Surfaces a-Physicochemical and Engineering Aspects* **1995**, *96* (1-2), 1-46.
62. *Zetasizer Nano Series User Manual; Malvern Instruments: Worcestershire, U. K.* **2005**.
63. *NanoSight NS500 User Manual Version 2.6; NanoSight Ltd., Amesbury, Wilshire, U. K.* **2010**.
64. Miles, W. C.; Goff, J. D.; Huffstetler, P. P.; Reinholz, C. M.; Pothayee, N.; Caba, B. L.; Boyd, J. S.; Davis, R. A.; Riffle, J. S., Synthesis and Colloidal Properties of Polyether-Magnetite Complexes in Water and Phosphate-Buffered Saline. *Langmuir* **2009**, *25* (2), 803-813.
65. Xu, X. Q.; Shen, H.; Xu, J. R.; Xie, M. Q.; Li, X. J., The colloidal stability and core-shell structure of magnetite nanoparticles coated with alginate. *Applied Surface Science* **2006**, *253* (4), 2158-2164.
66. Mefford, O. T.; Woodward, R. C.; Goff, J. D.; Vadala, T. P.; St Pierre, T. G.; Dailey, J. P.; Riffle, J. S., Field-induced motion of ferrofluids through immiscible viscous media: Testbed for restorative treatment of retinal detachment. *Journal of Magnetism and Magnetic Materials* **2007**, *311* (1), 347-353.
67. Wilson, K. S.; Goff, J. D.; Riffle, J. S.; Harris, L. A.; St Pierre, T. G., Polydimethylsiloxane-magnetite nanoparticle complexes and dispersions in polysiloxane carrier fluids. *Polymers for Advanced Technologies* **2005**, *16* (2-3), 200-211.
68. Purushotham, S.; Ramanujan, R. V., Modeling the performance of magnetic nanoparticles in multimodal cancer therapy. *Journal of Applied Physics* **107** (11).
69. Regmi, R.; Bhattarai, S. R.; Sudakar, C.; Wani, A. S.; Cunningham, R.; Vaishnava, P. P.; Naik, R.; Oupicky, D.; Lawes, G., Hyperthermia controlled rapid drug release from thermosensitive magnetic microgels. *Journal of Materials Chemistry* **2010**, *20* (29), 6158-6163.
70. Veiseh, O.; Gunn, J. W.; Zhang, M. Q., Design and fabrication of magnetic nanoparticles for targeted drug delivery and imaging. *Advanced Drug Delivery Reviews* **62** (3), 284-304.
71. Jain, T. K.; Morales, M. A.; Sahoo, S. K.; Leslie-Pelecky, D. L.; Labhasetwar, V., Iron oxide nanoparticles for sustained delivery of anticancer agents. *Molecular Pharmaceutics* **2005**, *2* (3), 194-205.
72. Kirsch, J. E., Basic Principles of Magnetic Resonance Imaging Contrast Agents. *Topics in Magnetic Resonance Imaging* **1991**, *3* (2), 1-18.
73. Weissleder, R.; Bogdanov, A.; Neuwelt, E. A.; Papisov, M., LONG-CIRCULATING IRON-OXIDES FOR MR-IMAGING. *Advanced Drug Delivery Reviews* **1995**, *16* (2-3), 321-334.

74. Sun, S. H.; Zeng, H., Size-controlled synthesis of magnetite nanoparticles. *Journal of the American Chemical Society* **2002**, *124* (28), 8204-8205.
75. Pinna, N.; Grancharov, S.; Beato, P.; Bonville, P.; Antonietti, M.; Niederberger, M., Magnetite Nanocrystals: Aqueous Synthesis, Characterization, and Solubility. *Chemistry of Materials* **2005**, *17* (11), 3044-3049.
76. Park, J.; An, K. J.; Hwang, Y. S.; Park, J. G.; Noh, H. J.; Kim, J. Y.; Park, J. H.; Hwang, N. M.; Hyeon, T., Ultra-large-scale syntheses of monodisperse nanocrystals. *Nature Materials* **2004**, *3* (12), 891-895.
77. Harris, L. A.; Goff, J. D.; Carmichael, A. Y.; Riffle, J. S.; Harburn, J. J.; St Pierre, T. G.; Saunders, M., Magnetite nanoparticle dispersions stabilized with triblock copolymers. *Chemistry of Materials* **2003**, *15* (6), 1367-1377.
78. Kim, D. K.; Mikhaylova, M.; Zhang, Y.; Muhammed, M., Protective coating of superparamagnetic iron oxide nanoparticles. *Chemistry of Materials* **2003**, *15* (8), 1617-1627.
79. Ge, J. P.; Hu, Y. X.; Biasini, M.; Dong, C. L.; Guo, J. H.; Beyermann, W. P.; Yin, Y. D., One-step synthesis of highly water-soluble magnetite colloidal nanocrystals. *Chemistry-a European Journal* **2007**, *13* (25), 7153-7161.
80. Xie, J.; Xu, C.; Kohler, N.; Hou, Y.; Sun, S., Controlled PEGylation of monodisperse Fe₃O₄ nanoparticles for reduced non-specific uptake by macrophage cells. *Advanced Materials* **2007**, *19*, 3163-+.
81. Jain, N.; Wang, Y. J.; Jones, S. K.; Hawke, B. S.; Warr, G. G., Optimized Steric Stabilization of Aqueous Ferrofluids and Magnetic Nanoparticles. *Langmuir* **2006**, *22* (6), 4465-4472.
82. Daou, T. J.; Pourroy, G.; Greneche, J. M.; Bertin, A.; Felder-Flesch, D.; Begin-Colin, S., Water soluble dendronized iron oxide nanoparticles. *Dalton Transactions* **2009**, (23), 4442-4449.
83. Perez, J. M.; Josephson, L.; O'Loughlin, T.; Hogemann, D.; Weissleder, R., Magnetic relaxation switches capable of sensing molecular interactions. *Nature Biotechnology* **2002**, *20* (8), 816-820.
84. Ge, J. P.; Hu, Y. X.; Yin, Y. D., Highly tunable superparamagnetic colloidal photonic crystals. *Angewandte Chemie-International Edition* **2007**, *46*, 7428-7431.
85. Yang, J.; Lee, C. H.; Ko, H. J.; Suh, J. S.; Yoon, H. G.; Lee, K.; Huh, Y. M.; Haam, S., Multifunctional magneto-polymeric nanohybrids for targeted detection and synergistic therapeutic effects on breast cancer. *Angewandte Chemie-International Edition* **2007**, *46* (46), 8836-8839.
86. Nasongkla, N.; Bey, E.; Ren, J. M.; Ai, H.; Khemtong, C.; Guthi, J. S.; Chin, S. F.; Sherry, A. D.; Boothman, D. A.; Gao, J. M., Multifunctional polymeric micelles as cancer-targeted, MRI-ultrasensitive drug delivery systems. *Nano Letters* **2006**, *6* (11), 2427-2430.
87. Hamoudeh, M.; Al Faraj, A.; Canet-Soulas, E.; Bessueille, F.; Leonard, D.; Fessi, H., Elaboration of PLLA-based superparamagnetic nanoparticles: Characterization, magnetic behaviour study and in vitro relaxivity evaluation. *Int. J. Pharm.* **2007**, *338* (1-2), 248-257.
88. Berret, J. F.; Schonbeck, N.; Gazeau, F.; El Kharrat, D.; Sandre, O.; Vacher, A.; Airiau, M., Controlled clustering of superparamagnetic nanoparticles using block copolymers: Design of new contrast agents for magnetic resonance imaging. *Journal of the American Chemical Society* **2006**, *128* (5), 1755-1761.
89. Akbulut, M.; Ginart, P.; Gindy, M. E.; Theriault, C.; Chin, K. H.; Soboyejo, W.; Prud'homme, R. K., Generic Method of Preparing Multifunctional Fluorescent Nanoparticles Using Flash NanoPrecipitation. *Advanced Functional Materials* **2009**, *19* (5), 718-725.

90. Liu, Y.; Tong, Z.; Prud'homme, R. K., Stabilized polymeric nanoparticles for controlled and efficient release of bifenthrin. *Pest Management Science* **2008**, *64* (8), 808-812.
91. Chen, T.; D'Addio, S. M.; Kennedy, M. T.; Swietlow, A.; Kevrekidis, I. G.; Panagiotopoulos, A. Z.; Prud'homme, R. K., Protected Peptide Nanoparticles: Experiments and Brownian Dynamics Simulations of the Energetics of Assembly. *Nano Letters* **2009**, *9* (6), 2218-2222.
92. Ungun, B.; Prud'homme, R. K.; Budijono, S. J.; Shan, J. N.; Lim, S. F.; Ju, Y. G.; Austin, R., Nanofabricated upconversion nanoparticles for photodynamic therapy. *Optics Express* **2009**, *17* (1), 80-86.
93. Kumar, V.; Wang, L.; Riebe, M.; Tung, H. H.; Prud'homme, R. K., Formulation and Stability of Itraconazole and Odanacatib Nanoparticles: Governing Physical Parameters. *Molecular Pharmaceutics* **2009**, *6* (4), 1118-1124.
94. Hiemenz, P.; Rajagopalan, R., Principles of Colloid and Surface Chemistry. **1997**, *3rd ed.*; Marcel Dekker: New York, 1997.
95. Johnson, B. K.; Saad, W.; Prud'homme, R. K., Nanoprecipitation of pharmaceuticals using mixing and block copolymer stabilization. *Polymeric Drug Delivery II: Polymeric Matrices and Drug Particle Engineering* **2006**, *924*, 278-291.
96. http://www.texloc.com/closet/cl_refractiveindex.html.
97. Filipe, V.; Hawe, A.; Jiskoot, W., Critical Evaluation of Nanoparticle Tracking Analysis (NTA) by NanoSight for the Measurement of Nanoparticles and Protein Aggregates. *Pharmaceutical Research* *27* (5), 796-810.
98. Mefford, O. T.; Vadala, M. L.; Goff, J. D.; Carroll, M. R. J.; Mejia-Ariza, R.; Caba, B. L.; St Pierre, T. G.; Woodward, R. C.; Davis, R. M.; Riffle, J. S., Stability of polydimethylsiloxane-magnetite nanoparticle dispersions against flocculation: Interparticle interactions of polydisperse materials. *Langmuir* **2008**, *24* (9), 5060-5069.
99. Mefford, O. T.; Carroll, M. R. J.; Vadala, M. L.; Goff, J. D.; Mejia-Ariza, R.; Saunders, M.; Woodward, R. C.; St Pierre, T. G.; Davis, R. M.; Riffle, J. S., Size analysis of PDMS-magnetite nanoparticle complexes: Experiment and theory. *Chemistry of Materials* **2008**, *20* (6), 2184-2191.
100. Vagberg, L. J. M.; Cogan, K. A.; Gast, A. P., Light-Scattering Study Of Starlike Polymeric Micelles. *Macromolecules* **1991**, *24* (7), 1670-1677.